Tesis Doctoral

Impresión óptica de nanopartículas metálicas

Gargiulo, Julián

2017-03-23

Universidad de Buenos Aires
Facultad de Ciencias Exactas y Naturales
Departamento de Física

Impresión óptica de nanopartículas metálicas

Tesis presentada para optar por el título de
Doctor de la Universidad de Buenos Aires en el área Ciencias Físicas
por Julian Gargiulo

Director de Tesis: Dr. Fernando D. Stefani
Consejera de Estudios: Dra. Andrea Bragas
Lugar de trabajo: Centro de Investigaciones en Bionanociencias,
Consejo Nacional de Investigaciones Científicas y Técnicas

Fecha de defensa: 23 de Marzo de 2017

A mi mamá y mi papá, de quienes surgió el placer por razonar el mundo,
la filosofía y la ciencia.
Por el infinito apoyo.

*Vi el Aleph, desde todos los puntos, vi en el Aleph la tierra, y en la tierra otra vez el Aleph y en el Aleph la tierra.**

J.L.Borges

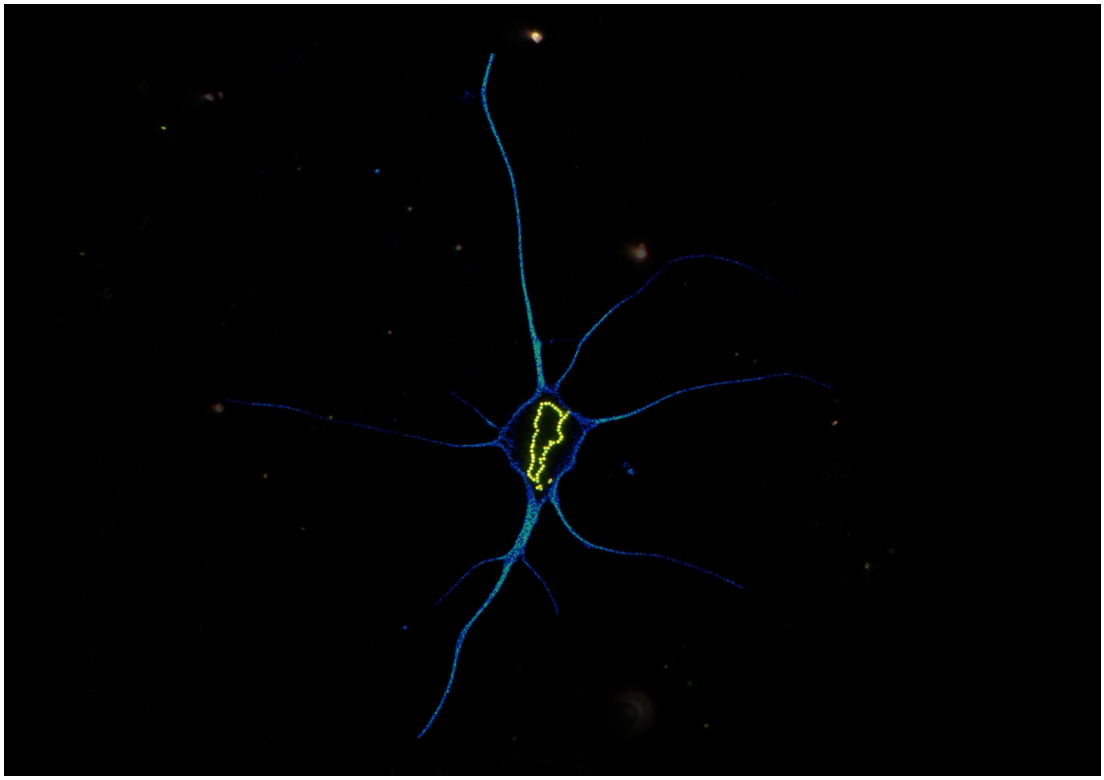

**I saw the Aleph from every point and angle, and in the Aleph I saw the earth and in the earth the Aleph and in the Aleph the earth.*

Resumen

Las nanopartículas metálicas (MNPs) presentan propiedades optoelectrónicas únicas que dependen de su forma y su tamaño y que no están presente en partículas de tamaños macroscópicos. Estas propiedades surgen a partir de sus resonancias plasmónicas superficiales localizadas (LSPRs), que producen intensificaciones enormes del campo electromagnético cerca de la superficie de las MNPs y aumentan sus secciones eficaces de dispersión y absorción. Estos efectos han motivado el uso de las MNPs en muchas aplicaciones del campo de la nanotecnología, incluyendo el sensado ultra-sensible, celdas solares, fotónica, microscopía, catálisis, medicina y farmacéutica.

La fabricación de MNPs puede conseguirse mediante métodos *top-down*(de arriba hacia abajo) o *bottom-up*(de abajo hacia arriba). En los primeros, un proceso litográfico o de ataque químico le agrega morfología a una película metálica previamente depositada sobre un sustrato. De esta manera pueden fabricarse estructuras en dos dimensiones con alta precisión y resolución. Sin embargo, la calidad del material es en general pobre y se obtienen partículas policristalinas con bordes rugosos. Además, la combinación de dos o más materiales mediante estas técnicas es complicada. Por otro lado, MNPs de una gran variedad de formas y composiciones pueden ser producidas en procesos bottom-up mediante sintésis química. Estas MNPs son monocristalinas y se les puede dar funciones químicas o biológicas específicas en su superficie. Sin embargo, las MNPs coloidales se obtienen en suspensiones líquidas y no es fácil controlar su ensamblado en posiciones precisas de un sustrato. Uno de los desafíos actuales de la nanotecnología es el desarrollo de un método para controlar su ensamblado con precisión nanométrica, lo que permitiría la aplicación de la enorme librería de partículas coloidales en nano y micro-dispositivos.

La impresión óptica de MNPs es un método puramente óptico que puede cumplir este objetivo. El mismo emplea láseres fuertemente enfocados para atra-

par MNPs desde una suspensión coloidal y llevarlas individualmente hasta posiciones específicas de un sustrato con gran precisión y versatilidad de diseño. Debido a que esta basada en fuerzas ópticas y que la interacción de la luz depende fuertemente de la forma y el material de la MNP, la técnica tiene un gran potencial para la deposición selectiva de diferentes tipos de MNPs y su combinación en patrones organizados.

Esta tesis presenta un estudio sistemático de la precisión y la resolución de la técnica de impresión óptica de nanoparticulas metálicas. Su potencial, sus limitaciones y perspectivas son analizadas en base a experimentos y consideraciones teóricas.

En primer lugar, la precisión para inmovilizar MNPs únicas fue estudiada en función de la potencia del láser de impresión, para MNPs esféricas de oro y plata. Se identificaron dos regímenes diferentes, dependiendo de si el láser utilizado estaba o no sintonizado con la LSPR de la partícula. Sorprendentemente y a pesar de ser una técnica óptica de campo lejano, es posible imprimir MNPs con una precisión cercana a los 50nm, muy por debajo del límite de difracción.

Luego se estudió la resolución de la impresión óptica, entendida como la capacidad de imprimir dos o más partículas a distancia controlada. Antes de este trabajo hubo varios reportes en donde se mostró que era imposible imprimir dos partículas a distancias menores que 200 - 300 nm, debido a una repulsión de naturaleza incierta. Este hecho constituyó una importante limitación en la técnica, que impidió su implementación para fabricar circuitos de MNPs conectadas o estructuras con partículas acopladas plasmonicamente. En esta tesis se estudiaron los orígenes de esa repulsión y se encontró que estaba relacionada al calentamiento óptico de las partículas ya impresas sobre el sustrato. Se propusieron y pusieron a prueba experimentalmente varias estrategias para lograr la impresión de partículas conectadas, lográndose por primera vez la impresión óptica de partículas conectadas y con orientación bien definida.

Finalmente, la impresión óptica fue utilizada como una herramienta para el estudio sistemático de reacciones químicas el nivel de partícula única. NPs de oro impresas ópticamente fueron usadas como semillas a partir de las cuales se obtuvieron NPs más grandes mediante la reducción asistida por plasmónica de $HAuCl_4$acuoso. De esta manera la geometría final de cada partícula se controló independientemente.

Palabras clave: *fabricación de patrones de partículas coloidales, nanopartículas metálicas, manipulación óptica, termoforesis, química asistida por plasmónica*

Optical printing of metallic nanoparticles

Metal nanoparticles (MNPs) present unique size and shape dependent optoelectronic properties that are not present in larger particles or the bulk material, which arise from their localized surface plasmon resonances (LSPRs). LSPRs produce dramatic enhancements of the electromagnetic field close to the surface of the particle as well as large scattering and absorption cross-sections. These particular properties have motivated the use of MNPs in many applications in the field of nanotechnology, including ultra-sensitive sensing, light harvesting, imaging, photonics, catalysis, and medical and pharmaceutical therapies.

The fabrication of MNPs can be achieved by top-down or bottom-up approaches. In the first, lithographic or etching processes add morphology to a thin metallic film previously deposited on a substrate. In this way, two-dimensional nanostructures can be fabricated with high precision and resolution, but the material quality is usually poor leading to polycrystalline nanoparticles with rough surfaces. Also, combining two or more materials is challenging.

On the other hand, bottom-up produced colloidal MNPs can be obtained by chemical synthesis with a vast variety of shapes and compositions not available by top-down approaches. These nanoparticles are usually monocrystalline and can hold specific biological or chemical functions at their surfaces. However, colloidal nanoparticles are obtained in liquid suspensions and controlling their assembly onto precise positions of a substrate is not straightforward. Developing a method to control their assembly onto substrates with nanometric precision is one of the open challenges of nanotechnology. Such a method would enable the application of the enormous library of colloidal nanoparticles on nano- and micro-devices.

Optical printing is a powerful all-optical method that can accomplish this goal. It employs highly focused laser beams to trap colloidal nanoparticles from

suspension and deliver them individually into specific locations on a surface with high accuracy and flexibility of pattern design. Since it is based on optical forces and the interaction of light with MNPs is size and composition dependent, the technique has a strong potential for selective deposition of different kinds of MNPs and their combination in organized patterns.

This thesis presents a systematic study of the precision and resolution of optical printing applied to MNPs. Its potential, limitations and perspectives are analysed based on measurements and theoretical considerations.

First, the precision of optical printing to immobilize single MNPs was studied as a function of the laser power, for MNPs made of gold and silver. Two different regimes were identified depending on whether the laser used is tuned to the LSPR or not. Remarkably, in spite of being a far-field optical technique, MNPs can be printed with a precision of about 50 nm, well beyond the diffraction limit.

Next, the resolution of optical printing, i.e. the capacity to print two or more MNP at controlled distances, was addressed. Before this work, several reports had shown that it was impossible to print two MNPs closer together than 200 – 300 nm, due to a repulsion of unclear nature. This constituted an important limitation that has obstructed the use of optical printing for the fabrication of plasmonically coupled structures and circuits of connected NP. In this thesis, the origin of this repulsion was investigated and found to be related to optical heating of the already printed MNP. Furthermore, several strategies to effectively print connected MNPs were proposed and tested, accomplishing for the first time optical printing of connected nanoparticles with well-defined orientation.

Finally, optical printing was applied as a tool for studying systematically chemical reactions at the single MNP level. As an example, optically printed gold NPs were used as seeds to obtain larger NPs by plasmon-assisted reduction of aqueous $HAuCl_4$. In this way, supported MNPs were reshaped in situ to controlled final morphologies.

Keywords: *Colloidal nanopatterning, Metal nanoparticles, Optical manipulation, Thermophoresis, Plasmon-assisted chemistry.*

Contents

Motivation and Outlook

There is an enormous and continuously growing list of colloidal nanoparticles (NPs) that can be prepared through chemical synthesis. Metals[1], semiconductors, oxides or magnetic materials can be synthesized as NPs of many different sizes, shapes and compositions[2, 3]. Besides the most common nearly spherical NPs , many other shapes are attainable such as rods, cubes, polygonal ,prisms, stars, wires, and more.[4, 5, 6] Additionaly, two materials can be combined to obtain composites of different geometries, like core-shell NPs .[7]. In addition to the material composition, changing the geometry of the particle allows the tuning of physical properties such as optical, catalytic, electronic, and magnetic properties, which are size and shape dependent in the nanoscale.[8].

Also, the capping molecules of the NPs can be exchanged or modified with a variety of functional molecular moieties, allowing the tailored design of the NPs surface chemical properties[9]. This molecular conjugation can include biomolecules like DNA, enzymes or antibodies, providing the particles with a biological function.

In summary, chemical synthesis permits the large-scale and low-cost production of colloidal NPs with a vast diversity of tailored physical, chemical and biological properties. In addition, assemblies of NPs can lead to novel properties not present in the isolated particles. For example, in the case of plasmonic, semiconducting or magnetic particles in close proximity, electric or magnetic moments of each particle can couple with the others, giving rise to collective effects. However, colloidal NPs are obtained in liquid suspensions and their assembly onto precise positions of a substrate is not straightforward. Developing methodologies to control their assembly onto substrates with nanometric precision is one of the open challenges of nanotechnology. Such a method would enable the application of the enormous library of colloidal nanoparticles on nano- and micro-devices.

In this thesis the advantages and limitations of employing optical printing to

accomplish that goal is studied. Although the technique is in principle applicable to many colloidal particles, this thesis is focuses on metallic NPs . In particular, Au and Ag nearly spherical NPs were employed. These NPs are among the most widely used and investigated, due to their unique size and shape dependent optoelectronic properties that arise from localized surface plasmon resonances (LSPRs). LSPRs produce dramatic enhancements of the electromagnetic field close to the NP surface as well as large scattering and absorption cross-sections. These particular properties have motivated the use of Au and Ag NPs in many applications in the field of nanotechnology, including ultra-sensitive sensing, light harvesting, imaging, photonics, catalysis, and medical and pharmaceutical therapies.

In the first chapter 1, the optical properties of metallic NPs are presented. The theoretical background of LSPRs is introduced, as well as methods for the analytical calculation of polarizabilities, absorption and scattering cross sections, electromagnetic fields and optical forces.

In chapter 2 a review of the most extended methods for 2D patterning of surfaces with colloidal NPs is provided. It includes a description of the state-of-the-art of self-assembly methods, template assisted self-assembly methods, and template-free methods guided by light. The aim of that chapter is to provide a proper context for the introduction of optical printing, which is described in chapter 3, along with a review of the relevant progress during the last years in the field and a discussion about its open questions and current challenges.

In chapter 4, the experimental set-up and the custom software that was specifically designed and developed for the experiments in this thesis is presented.

Then, in chapter 5, the precision of optical printing to immobilize isolated metallic NPs is studied. Methods to quantify the precision are introduced and accuracy limits are tested for Ag and Au particles at different powers and wavelengths. Finally, theoretical framework and simulations are used to rationalize the experimental results and provide a complete picture of the physical mechanism of optical printing.

The capability of optical printing to place NPs close to each other, and even connect them in a controlled fashion, is investigated in Chapter 6, including several combinations of particles and substrates. It is found that connecting metallic NPs by optical printing may be limited by photothermal effects. The different phenomena that may be involved are experimentally tested and evaluated with

the help of computer simulations.

Finally, in chapter 7, in-situ growing and reshaping of optically printed Au NPs is studied, demonstrating the advantages of optical printing for carrying out systematic investigations of photo-chemical reactions on colloidal NPs , including the role of light polarization.

1

Optical properties of metallic nanoparticles

In this chapter we briefly present the optical properties of metallic nanoparticles (NPs). First, theoretical background of plasmon resonances is introduced in section 1.1. Then, analytical and numerical methods are presented to calculate polarizabilities (section 1.1), absorption and scattering cross sections (1.2), electromagnetic fields (1.2), temperature fields due to plasmonic heating (1.3) and optical forces (1.4).

1.1 Localized surface plasmon resonances

Optical properties of metallic NPs arise from their localized surface plasmon resonances (LSPRs). Lets describe what they are.

A plasma is a medium with equal concentration of positive and negative charges, of which at least one charge type is mobile[10]. A metallic crystal can be described as a plasma, were the negative charges of the delocalized conduction electrons are balanced by an equal concentration of positive charge of the ion cores. An electromagnetic wave can cause the collective motion of the electrons, which in turn radiate and contribute to the field. This coupled mechanical-electromagnetic wave is known as a *surface plasmon* and is confined to the surface of the metals, due to the typically short penetration lenght of conductors. Surface plasmons propagates in a bulk material, but if the metal dimensions are smaller than the propagation lenght, a localized non-propagating plasmon is obtained. For the right frecuency of the field, the response of the electrons will be reso-

nanant. Then, localized surface plasmon esonances are non-propagating resonant oscillations of the conduction electrons of metallic nanostructures, coupled to the electromagnetic field.[11]

In small particles, curved surfaces and positive nuclei exerts restoring forces to the movement of the electrons. Therefore, the resonance condition of the systems depend on the exact size and shape of the particle, as well as the dielectric constant of the metal and its surrounding. For noble metals like gold and silver and particles with nanometric dimensions, LSPR can be excited in the optical range, i.e. these metallic NPs interact strongly with light: absorption, scattering and the electric field close the surface are enhanced.

In order to further describe the interesting properties of LSPR, we address the simple but illustrative case of a metal sphere with a radius a and relative dielectric constant ϵ, sorrounded by an isotropic medium with a relative dielectric constant ϵ_m, illuminated by a linear polarized plane wave of wavelenght λ with an amplitude E_0. If the radius is considerably smaller than the wavelenght ($a << \lambda$), the Rayleigh or *quasi-static* approximation can be applied, which consists in neglecting the phase propagation of the electromagnetic field inside the particle. Doing that, the time and spacial parts of the electromagnetic field can be separated. It is no longer necessary to solve the full Maxwell equations. Instead, the problem is described by the Laplace equation for the electrostatic spatial field and the harmonic time dependence can be incorporated afterwards. Analytical solutions for this system are available, (for example in the book of Maier[11] section 5.1). The electrostatic potential inside the sphere ϕ_{in} and outside of the sphere ϕ_{out} are found to be

$$\phi_{in} = -\frac{3\epsilon_m}{\epsilon + 2\epsilon_m} E_0 r cos\theta \tag{1.1}$$

$$\phi_{out} = -E_0 r cos(\theta) + \frac{\epsilon - \epsilon_m}{\epsilon + 2\epsilon_m} E_0 a^3 \frac{cos\theta}{r^2} \tag{1.2}$$

Equation 1.2 can be physically interpreted as the superposition of the applied field (first term) and that of a dipole located at the particle centre (second term). This solution is similar to the well-known electrostatic potential of a dipole[12]

$$\phi_{dipolar} = -E_0 r cos(\theta) + \frac{\mathbf{p} \cdot \mathbf{r}}{4\pi\epsilon_0\epsilon_m r^3} \tag{1.3}$$

after the assignment of the induced dipole moment $\mathbf{p}$ to the expression

$$\mathbf{p} = 4\pi\epsilon_0\epsilon_m a^3 \frac{\epsilon - \epsilon_m}{\epsilon + 2\epsilon_m}\mathbf{E_0} \tag{1.4}$$

Therefore, the electric field outside the particle can be described in terms of an induced dipole situated at the nanoparticle center. The strength of the interaction between the field and the induced dipole moment is given by the polarizability α defined via $\mathbf{p} = \epsilon_0\epsilon_m\alpha\mathbf{E_0}$. Introducing this definition into Equation 1.4 leads to

$$\alpha(\omega) = 4\pi a^3 \frac{\epsilon(\omega) - \epsilon_m}{\epsilon(\omega) + 2\epsilon_m} \tag{1.5}$$

which is known as the Clausius-Mosotti equation for the polarizability. We have made explicit that the frecuency dependence of the polarizability is mainly from the dielectric function of the particle. There are two major contibutions to $\epsilon(\omega)$: (i) the quasi-free movement of the conduction band electrons and (ii) the bound-electron term, corresponding to interband transitions that take place when the energy of the incoming photons exceeds the energy between different bands. Even though there are theoretical models to predict the value for $\epsilon(\omega)$, the approach in this thesis will be to use available experimental data for bulk material, but including the correction for small spheres proposed by Coronado et. al.[13]

$$\epsilon(\omega, a) = \epsilon_{bulk}(\omega) + \frac{\omega_p^2}{\omega^2 + i\omega\gamma_0} - \frac{\omega_p^2}{\omega^2 + i\omega(\gamma_0 + B\frac{v_f}{a})} \tag{1.6}$$

where $\omega_p = \frac{ne^2}{\epsilon_0 m_{eff}}$ is the plasmon frecuency, $\gamma_0 = \frac{v_f}{l_\infty}$ is the intrinsic width of the dipole plasmon polariton, l_∞ is the mean free path of the conduction electrons in the bulk, B is a dimensionless parameter, usually assumed to be close to unity[13] and v_f is the fermi velocity. Further discussion on the correction for small spheres can be found in the book by Bohren and Huffman[14] (chapter 12.1.6).

Fig 1.1 shows, as a function of wavelength, the modulus, real and imaginary parts of the polarizability calculated using 1.5 for Ag and Au NPs with a diameter of 60nm. Indeed, the first noticeable feature is the arise of a resonance, achieved when the denominator is a minimum. For small or slowly-varying $Im(\epsilon)$ the resonant condition is

$$Re(\epsilon(\omega)) = -2\epsilon_m \tag{1.7}$$

which is known as the Fröhlich condition. This resonance correspond to a LSPR

and has implications in the absorption, scattering and near field of the particle, as discussed in section 1.2. It is important to note that equation 1.5 is strictly valid for vanishing radius particles. For larger particles the *quasi-static* approximations is no longer accurate. Therephore, Kuwata et. al.[15] proposed an extended expression for the polarizability, that includes higher orders of the size parameter $x = \frac{\pi a}{\lambda}$.

$$\alpha_K = V \frac{1 - \frac{1}{10}(\epsilon + \epsilon_m)x^2}{(\frac{1}{3} + \frac{\epsilon_m}{\epsilon - \epsilon_m}) - \frac{1}{30}(\epsilon + 10\epsilon_m)x^2 - i\frac{4\pi^2\epsilon_m^{3/2}}{3}\frac{V}{\lambda^3}} \tag{1.8}$$

with $V = \frac{4\pi a^3}{3}$ the volume of the shpere. Note the plasmon resonance now depends explicitly on the particle size. Compared with the Claussius-Mossoti equation, Kuwata polarizability includes a (typically red) shift of the LSPR with the particle size, as can be seen in figure 1.1. The extended Kuwata polarizability α_K is the one used in this thesis for calculations of the electric fields and optical forces.

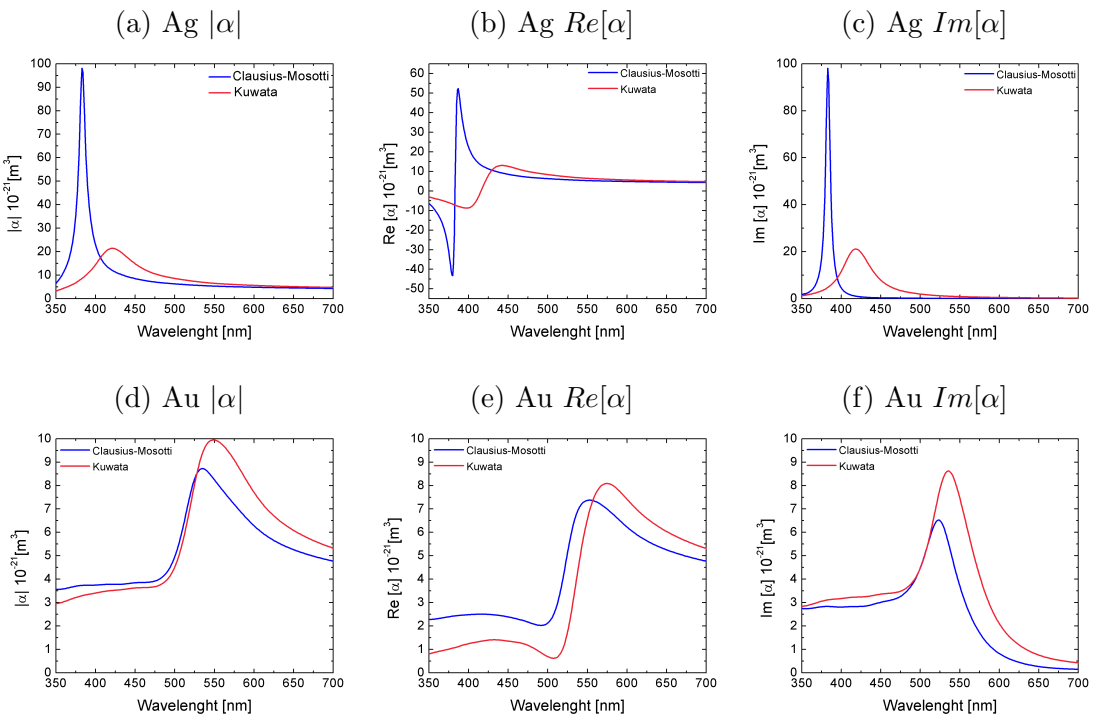

Figure 1.1: Polarizability of Ag and Au spheres of 60nm, calculated using Clausius-Mosotti and Kuwata expression.

1.2 Enhanced absorption, scattering, and near-field intensity

In the previous section we have shown that under ilumination of the right frecuency, the polarizability of a metal particle has a resonant response. In that case, the NP acts as an electrical dipole, resonantly absorbing and radiating light. The extinction σ_{ext} and scattering σ_{sca} cross-sections are defined as the ratio between the total scattered P_{sca} or extinct P_{exc} power by the radiating dipole and the intensity I_{inc} of the incident light. For a small particle, they are related to the polarizability through[11]

$$\sigma_{ext} = \frac{P_{ext}}{I_{inc}} = kIm\left[\alpha\right] \tag{1.9}$$

$$\sigma_{sca} = \frac{P_{sca}}{I_{inc}} = \frac{k^4}{6\pi}|\alpha|^2 \tag{1.10}$$

where $k = \frac{2\pi}{\lambda}$ is the wavenumber of the incident wave. The absorption cross section σ_{abs} is then obtained by $\sigma_{abs} = \sigma_{ext} - \sigma_{sca}$. Figure 1.2 show the σ_{sca} and σ_{abs} for Ag and Au NPs with a diameter of 60 nm, calculated using Kuwata polarizability. For both material an enhancement of absorption and scattering is produced when the LSPR is exited.

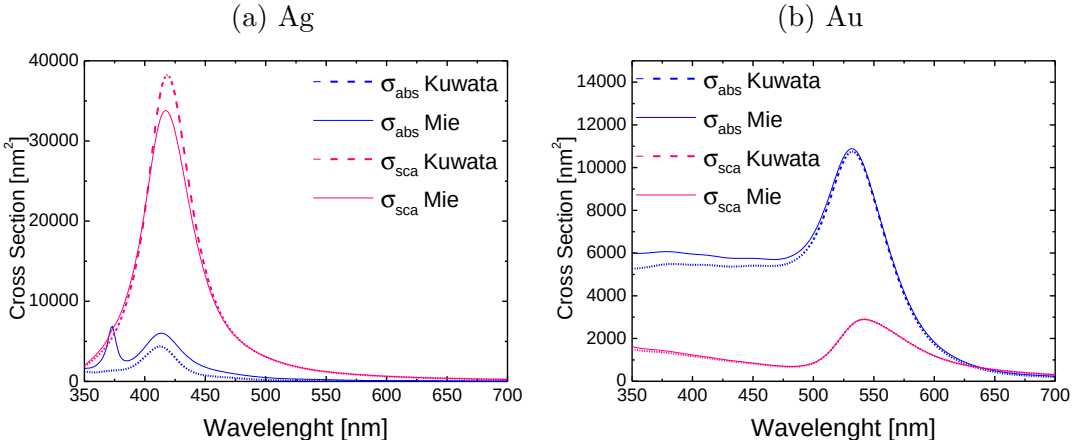

Figure 1.2: Absorption (blue) and Scattering (pink) cross section vs wavelenght for a)Ag and b) Au spheres of 60nm diameter in water. Solid lines correspond to Mie theory and dashed lines were calculated using Kuwata polarizability and equations 1.9 and 1.10.

Equations 1.9 and 1.10 are valid in the dipolar regime, which is correct for small particles. For larger particles the complete electrodynamic problem must be solved. An analytical solution for spheres of arbitrary size was obtained by Mie and consist in a multipole expansion of the field in terms of vector harmonics. This approach is generally known as Mie Theory and provides exact expressions for extinction σ_{ext} and scattering σ_{sca} cross sections.

$$\sigma_{ext} = \frac{2\pi}{|k|^2}\sum_{j=1}^{\infty}(2j+1)Re\left[|a_j| + |b_j|\right] \tag{1.11}$$

$$\sigma_{sca} = \frac{2\pi}{|k|^2}\sum_{j=1}^{\infty}(2j+1)(|a_j|^2 + |b_j|^2) \tag{1.12}$$

with the coefficients a_j and b_j given by

$$a_j = \frac{m\psi_n(mx)\psi_n^{'}(x) - \psi_n(x)\psi_n^{'}(mx)}{m\psi_n(mx)\xi_n^{'}(x) - \xi_n(x)\psi_n^{'}(mx)} \tag{1.13}$$

$$b_j = \frac{\psi_n(mx)\psi_n^{'}(x) - m\psi_n(x)\psi_n^{'}(mx)}{\psi_n(mx)\xi_n^{'}(x) - m\xi_n(x)\psi_n^{'}(mx)} \tag{1.14}$$

where $m = n/n_m$ is the relative refractive index, $x = 2\pi a/\lambda$ is the size parameter, ψ_n and ξ_n are the Riccati-Bessel functions and $\psi_n^{'}$ and $\xi_n^{'}$ their derivatives with respect to the argument. A complete discussion about Mie theory can be found in Bohren et. al.[14], section 4.4. Figure 1.2 show the exact cross sections for Au and Ag 60nm spheres, calculated using Mie theory, compared with those obtained using Kuwata polarizability. As can be seen, Kuwata model predicts reasonably well both the position and the magnitude of the main resonances. On the other hand, Mie theory predicts a second resonance frecuency in the absorption of Ag particles around 375nm. This resonance correspond to a quadropular mode, and therefore can not be predicted by the Kuwata dipolar model. Since this mode does not couple efficiently with the far field, the resonance is not reflected in the scattering cross-section.

Another interesting feature of the LSPRs is the enhancement of the electric field close to the surface of the particle. For spheres, electric field $\mathbf{E} = -\nabla\phi$ can be evaluated from the potencials given by equations 1.1 and 1.2 to obtain

$$\mathbf{E_{in}} = \frac{3\epsilon_m}{\epsilon + 2\epsilon_m}\mathbf{E_0} \tag{1.15}$$

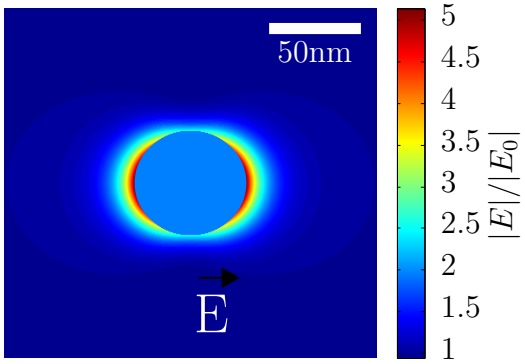

Figure 1.3: Map of the near field enhancement produced by a 60nm Au NP in water illuminated at $\lambda = 532nm$.

$$\mathbf{E_{out}} = \mathbf{E_0} + \frac{3\hat{\mathbf{r}}(\hat{\mathbf{r}} \cdot \mathbf{p}) - \mathbf{p}}{4\pi\epsilon_0\epsilon_m} \frac{1}{r^3} \tag{1.16}$$

where $\hat{\mathbf{r}}$ is the radial unit vector. Equations 1.15 and 1.16 show that a resonance in α implies a resonant enhancement of both internal and external fields. Figure 1.3 show the field enhancement map produced by a 60nm Au NP in water illuminated at $\lambda = 532nm$. The field has an anisotropic distribution, with maximum values being in regions parallel to polarization of the incident field. Interestingly, the field intensity in these regions is several times stronger than the incident field. Also, this strong near field decays proportional to r^{-3}. Therefore, for visible light, high intensities of field can be confined into sub-wavelength volumes, usually known as *hot spots*.

1.3 Light-induced heating

Metallic nanoparticles are efficient converters of light into heat[16]. Upon absorption of photons by the electron plasma, energy is transferred to the crystal lattice via electron-phonon coupling. This heat generation mechanism is extremely fast and thermalization occurs in a time of the order of several picoseconds. After that, the temperature inside the particle is homogeneous and heat is released to the surrounding medium, leading to temperature increases. The temperature field $T(r,t)$ around a NP is given by the heat diffusion equation[17]

$$\rho(r)\, c_p(r) \left[\frac{\partial T(r,t)}{\partial t} + \nabla \left(T(r,t)\, \mathbf{v}(r,t) \right) \right] - \kappa(r)\, \nabla^2 T(r,t) = q(r,t) \tag{1.17}$$

where $\mathbf{v}(r,t)$ is the velocity, ρ the density, κ the thermal conductivity and c_p the specific heat capacity at constant pressure of the fluid. $q(r,t)$ is the heat density generated by the NP. The heat transfer from the particle to the medium is mediated by convection and conduction, given by the terms $\rho c \nabla(T\mathbf{v})$ and $\kappa\nabla^2 T$ respectively. The ratio of these two magnitudes a dimensionless number known as the Rayleigh number Ra:

$$Ra = \frac{\rho c_p \tilde{L}\tilde{V}}{\kappa} \tag{1.18}$$

where $\tilde{L}$ and $\tilde{V}$ are the order of magnitude of a characteristic length and velocity of the system. If the Rayleigh number is much lower (higher) than unity, diffusion is dominant (negligible). We will consider the case of NPs embedded in solids or in fluids with low Ra, which is the actual situation in most practical nanoscale problems. In these systems the convection term of equation 1.17 can be dropped. For mediums with negligible absorption, the heat density inside q_{in} and oustide q_{out} the particle is given by

$$\begin{aligned} q_{in}(r,t) &= \frac{\sigma_{abs} I}{V} \\ q_{out}(r,t) &= 0 \end{aligned} \tag{1.19}$$

where I is the light power density. Here we have considered that the light absorbed by the particle is completely transformed into heat, a reasonable assumptions given the typically low fluorescence and photoluminescence quantum yields of metallic NPs. Then, for a spherical NP under continuous illumination in an homogeneous medium of thermal conductivity κ, the steady-state solution for the temperature increase ΔT is

$$\begin{aligned} \Delta T &= \frac{\sigma_{abs} I}{4\pi\kappa a} \qquad r < a \\ \Delta T &= \frac{\sigma_{abs} I}{4\pi\kappa r} \qquad r > a \end{aligned} \tag{1.20}$$

The calculated steady-state temperature field is shown in figure 1.4a for a 60nm Au NP in water, illuminated at the LSPR, with $\lambda = 532$ nm and an intensity of $I = 110\frac{kW}{cm^2}$. It must be noted that the decay length of the temperature field is in the order of magnitude of the particle size, as can be seen in 1.4b, giving raise to large temperature gradients close the surface. It is interesting to estimate the characteristic time $\tilde{\tau}_T$ related to the establishment of the steady-state temperature

profile (i.e. transient period). From dimensional analysis of 1.17 it is[17]

$$\tilde{\tau}_T = \frac{\rho c_p \tilde{L}^2}{\kappa} \tag{1.21}$$

which is in the order of the ns to μs for nanostructures.

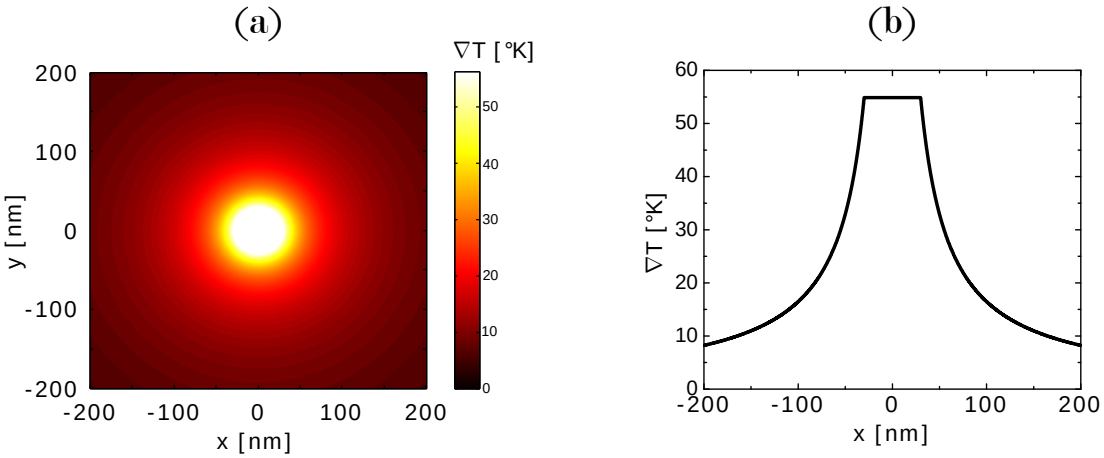

Figure 1.4: (a) Map of the steady-state temperature increase. (b) Steady-state temperature increase versus the distance to the NP center. Calculus correspond to 60 nm Au NP in water illuminated at $\lambda = 532$ nm with an irradiance $I = 110 \frac{kW}{cm^2}$.

1.4 Optical forces

When a light beam is absorbed or scattered by a body, its change in momentum is transferred to the body and an optical force arise. The calculation of the optical force $\mathbf{F}_{optical}$ on a NP can be derived from the rate of change of momentum of the electromagnetic field. For an electromagnetic wave, the momentum density in a medium with relative dielectric constant ϵ_r and magnetic suceptibility μ_r is given by the Maxwell stress tensor[18]

$$\overleftrightarrow{\mathbf{T}}(\mathbf{r},t) = \left[\epsilon_r\epsilon_0 \mathbf{E}\otimes\mathbf{E} + \mu_r\mu_0 \mathbf{H}\otimes\mathbf{H} - \frac{1}{2}(\epsilon_r\epsilon_0|\mathbf{E}|^2 + \mu_r\mu_0|\mathbf{H}|^2)\overleftrightarrow{\mathbf{I}}\right] \tag{1.22}$$

were $\overleftrightarrow{\mathbf{I}}$ is the unit dyadic. The time-average mechanical force acting on an arbitrary body within the close surface S is obtained by integrating the momentum flux over the surface

$$\langle \mathbf{F}_{optical} \rangle = \int_S \left\langle \overleftrightarrow{\mathbf{T}}(\mathbf{r},t) \right\rangle \mathbf{n}\, ds \tag{1.23}$$

where brackets indicate a time average and **n** is the surface normal.It is important to note that the fields used to calculate the Maxwell tensor are the self-consistent fields of the problem, i.e. the superposition of the incident and induced field.

The stress tensor formalism is suitable for various computational approaches, however, physical insight of optical forces can be gained from analytical approximate models. If the particles are small compared to the wavelength of light, the Rayleigh approximation discussed in section 1.1 can be applied. Then, the particle is modelled as a point-like electric dipole **p** of polarizability α given by equation 1.8. The Lorentz force on such dipole is

$$\mathbf{F}_{dipole} = (\mathbf{p} \cdot \nabla)\,\mathbf{E} + \mu \frac{d\mathbf{p}}{dt} \times \mathbf{H} \tag{1.24}$$

Using complex notation and taking the time average over the optical period $T = 2\pi/\omega$ leads to[19]

$$\langle \mathbf{F} \rangle = \frac{\epsilon_0 \epsilon_m}{2} Re\left(\sum_j \alpha E_j \nabla E_j^* \right) \tag{1.25}$$

where E_j are the electric field components and $*$ indicates the complex conjugation. Equation 1.25 is handy for calculus, because it only depends on the external electric fields. However, it is assumed that the small dipole does not modify the fields, which can be inaccurate especially for resonant particles. Further physical insight on optical forces is achieved by recasting 1.25 into the sum of three terms[20]

$$\langle \mathbf{F} \rangle = \underbrace{\alpha^{'} \frac{\epsilon_0 \epsilon_m}{4} \nabla |\mathbf{E}|^2}_{\text{Gradient force}} + \underbrace{\alpha^{''} \frac{k \epsilon_m}{c} \langle \mathbf{S} \rangle}_{\text{Radiation pressure}} + \underbrace{\alpha^{''} \frac{\epsilon_0 \epsilon_m}{4i} \nabla \times \mathbf{E} \times \mathbf{E^*}}_{\text{Spin curl force}} \tag{1.26}$$

where $\mathbf{S} = \mathbf{E} \times \mathbf{H^*}$ is the Poynting vector and the notation $\alpha^{'} = Re\,[\alpha]$ and $\alpha^{''} = Im\,[\alpha]$ was adopted. The first term represents the optical gradient force, a conservative force proportional to the gradient of the irradiance and the real part of the polarizability $\alpha^{'}$. If $\alpha^{'}$ is positive, it pushes towards the direction of maximum intensity. The second terms is the non conservative radiation pressure proportional to the imaginary part of the polarizability $\alpha^{''}$. It pushes the particle in the direction of the Poynting vector, which for electromagnetic waves is collinear with the wave vector **k**. For historical reasons it is also known as the *scattering force*, but it can be a rather misleading name. In fact, $\alpha^{''}$ depends on

both the absorption and scattering cross sections, as deduced from equation 1.9. Therefore it is more correct to call it the *absorption plus scattering* force. The last term is an additional non conservative force associated with the non uniform distribution of the spin density of the light. It is zero for plane waves or linearly polarized fields, but can be relevant for highly focused beams carrying angular moment.

Equation 1.26 shows that the polarizability α is the key property of particles that determines the magnitude and direction of the three optical forces. In metals, the resonance in the polarizability can be exploited to obtain enhanced forces at specific wavelengths, compared to dielectric particles of the same size. Also, the relative strength between gradient and radiation pressure is related to the ratio between the real and imaginary part of the polarizability, which is wavelenght dependent. This means that wavelenght must be chosen according to the application. For example, for optical trapping in highly focused beams, gradient forces are employed to confine particles in the region of higher intensity, while radiation pressure acts as a destabilizing force that must be avoided. In that case, a large $\alpha^{'}$ and small $\alpha^{''}$ is required. On the other hand, optical printing takes advantage of both gradient forces and radiation pressure to push particles towards a surface.

The calculation of optical forces exerted on metallic nanoparticles in the focus of a Gaussian beam in the Rayleight approximation isnow presented, following the derivation of Agayan et.al [21]. The electric field in cylindrical coordinates of the Gaussian beam propagating along the z axis is described in the paraxial approximation by

$$\mathbf{E}(r,z) = \mathbf{E_0}\frac{2}{\pi}\frac{w_0}{w}e^{\frac{-r^2}{w^2}}e^{i\left(k\left(\frac{r^2}{2R}+z\right)+\phi\right)} \tag{1.27}$$

$$R = z\left(1+\frac{z_0^2}{z^2}\right) \quad \phi = \tan^{-1}\left(\frac{z}{z_0}\right) \quad w(z) = w_0\sqrt{1+\frac{z_0^2}{z^2}} \tag{1.28}$$

whith $z_0 = \pi w_0^2 n/\lambda$ and $\mathbf{E_0}$ the maximum field amplitude at $(0,0)$, related to the total power P of the beam through $|E_0|^2 = 2P\mu_0 c/(nw_0^2)$. The parameter w_0 is the beam waist at the focal plane ($z = 0$), also called the Gaussian beam radius, and represents radius at which the field has decreased to $1/e$, and the intensity has decreased to $1/e^2$. The time-averaged intensity density, also known

as irradiance, is calculated by[12] $I = \frac{Re(\mathbf{E}\times\mathbf{H^*})}{2} = \frac{|\mathbf{E}|^2 n}{2\mu_0 c}$. For a Gaussian beam, the irradiance is

$$I(r,z) = I_0 \left(\frac{w_0}{w(z)}\right)^2 e^{-\frac{2r^2}{w(z)^2}} \tag{1.29}$$

Inserting the expression 1.27 for a Gaussian beam into equation 1.25 gives an analytical expression for the optical forces. The gradient force in the radial F^r_{grad} and axial F^z_{grad} directiond are therefore:

$$F^z_{grad}(r,z) = -\alpha^{'}\frac{\epsilon_0}{\pi}E_0^2\frac{z w_0^4}{z_0^2}\left(\frac{1}{w^4} - \frac{2r^2}{w^6}\right)e^{-\frac{2r^2}{w^2}}$$
$$F^r_{grad}(r,z) = -\alpha^{'}\frac{2\epsilon_0}{\pi}E_0^2\frac{r w_0^2}{w^4}e^{-\frac{2r^2}{w^2}} \tag{1.30}$$

and the scattering plus absorption force in the radial F^r_{sca} and axial F^z_{sca} direction are

$$F^z_{sca}(r,z) = \alpha^{''}\frac{\epsilon_0}{\pi}E_0^2\frac{w_0^2}{w^2}\left(k - \frac{kr^2}{2}\frac{z^2 - z_0^2}{\left(z^2+z_0^2\right)^2} - \frac{w_0^2}{z_0 w^2}\right)e^{-\frac{2r^2}{w^2}}$$
$$F^r_{sca}(r,z) = \alpha^{''}\frac{\epsilon_0}{\pi}E_0^2\frac{rkw_0^2}{Rw^2}e^{-\frac{2r^2}{w^2}} \tag{1.31}$$

Force fields in the Rayleigh regime are shown in figure 1.5. They are based on equations 1.30 and 1.31 for a 60 nm Au sphere. The Gaussian beam has a total power of $P = 1$ mW and a waist of $w_0 = 266$ nm, the polarizability α is given by Kuwata model (equation 1.8) and the particle is illuminated at the frecuency of its LSPR at 532 nm in water. At this wavelength the imaginary part of the polarizability $\alpha^{''}$ dominates over the real part $\alpha^{'}$, and therefore the total optical force is mainly due to the scattring plus absorption contribution.

It is important to recall the two sources of error of equations 1.30 and 1.31. First, only the external fields and not the particle-induced fields are considered. The second one arises from the paraxial description of the Gaussian beam, which can be inaccurate for higly-focused beams. In the work by Dienerowitz et. al.[18], a quantitatively estimation about the error of the Rayleigh approximation in the calculus of forces is provided, showing that errors are mainly in the calculus of radial forces. Nevertheless, these equations are a useful tool to predict with simple expressions the complex interaction of metallic particles with light.

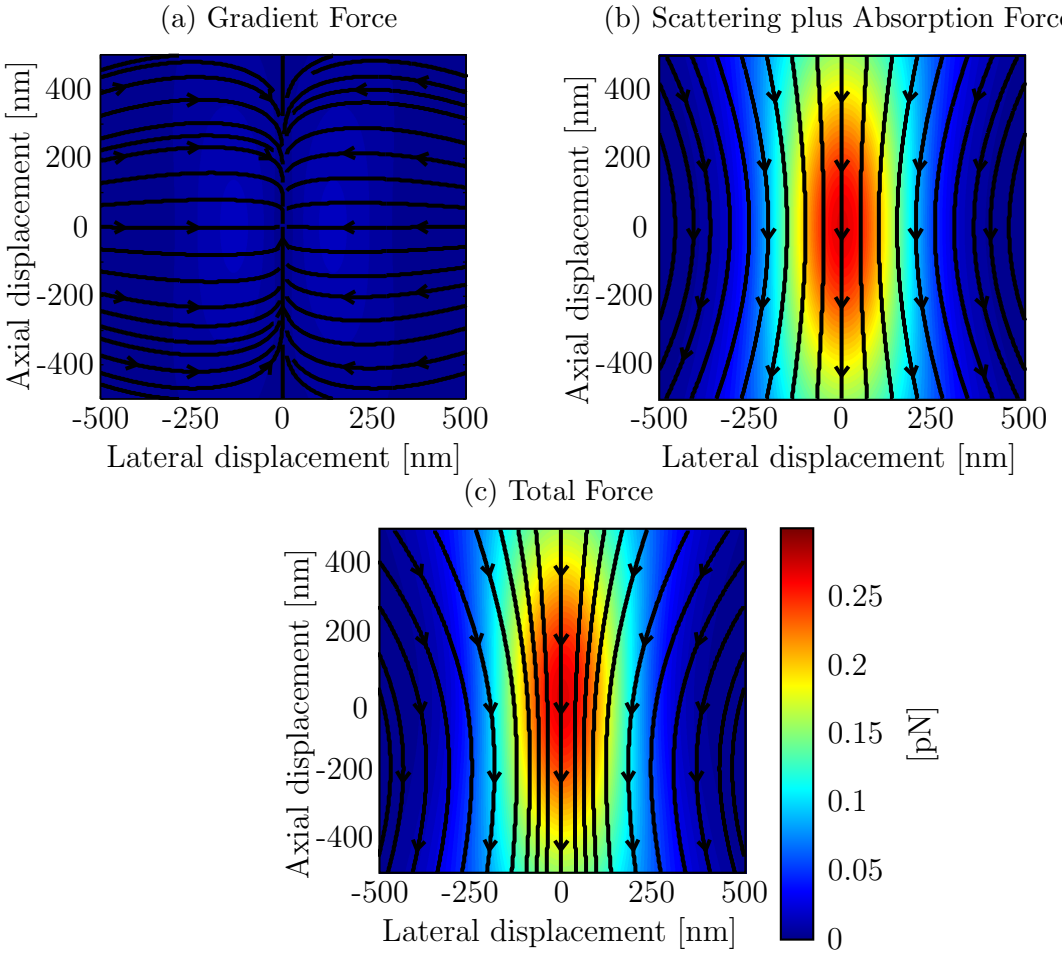

Figure 1.5: Optical force fields in the Rayleight regime, calculated for a $60nm$ Au nanoshpere illuminated at $\lambda = 532nm$. A Gaussian beam with a waist $w_0 = 266nm$ propagates from positive to negative z. The focal plane is at $z = 0$ and the total beam power is $P = 1mW$. Arrows denote direction of the force and its magnitude is colour coded.

2

Assembly of 2D patterns of colloidal nanoparticles onto surfaces

In order to make use in devices of the vast variety of properties of colloidal nanoparticles (NPs), an assembly process is required, capable of incorporating the NPs onto solid surfaces. These processes can have different degrees of complexity depending on the level of organization required for the particles. Developing a simple method to control spacial placement of individual particles with nanometric precision is one of the open challenges of nanotechnology. The scope of this chapter is to review the most extended methods for 2D patterning of surfaces with colloidal NPs, to provide a proper background for the introduction of Optical Printing. Methods are presented, providing an idea of their advantages and limitations and illustrating the different systems that can be fabricated. The review is limited to the fabrication of two-dimensional arrays with only one particle as height (monolayers). Extensive reviews on the subject can be found at references [22, 23, 24].

Self-assembly methods are introduced in section 2.1. Then, the incorporation of physical or chemical features into the substrate is described, that are used to control the assembly of particles into more complex structures (section 2.2). Finally photodynamic assembly is introduced in section 2.3, as an alternative template-free versatile approach for the fabrication of arbitrary patterns with high precision.

2.1 Self-assembled monolayers

The term self-assembly refers to the fact that particles can autonomously organize patterns as a result of the complex interplay of forces that take part in the assembly process. This organization emerges from interactions among the particles themselves and with the substrate, without external direction. To mention some examples, the interactions can include chemical bonds, dipolar and Coulomb forces, steric repulsions, capillary and hydrodynamic drag forces, flotation, van der Waals attractions or brownian motion[25]. The section starts with the description of self-assembly methods for the fabrication of closed-packed (dense arrangement) monolayer of particles in section 2.1.1. Then, methods to modify those monolayers in a former step to produce non-closed packed arrangements are introduced in section2.1.2.

2.1.1 Convective assembly of Closed-Packed monolayers

These methods take advantage of solvent evaporation to control the deposition of particles from colloidal suspension.[26] They are based on the formation of a very thin liquid film in the meniscus region of a receding droplet, close to the point where solvent, surface and air are in contact, as depicted in figure 2.1a. Once the liquid film falls below the colloid diameter, capillarity forces push the particles together. As the solvent evaporates, a convective flow is created, dragging particles from the bulk solution to the forming monolayer.

The success of convective induced methods rely on a proper matching of many experimental parameters, like the particle-surface interaction, the wetting properties, particle concentration or the evaporation rate. Experimentally, the speed of the receding drop can be controlled by vertically withdrawing the substrate out of the solution or by a second parallel confining surface mounted on a mobile stage. The evaporation rate can also be modified, changing the temperature through peltier cells. If all parameters are carefully matched, an homogeneous closed-packed monolayer grows continuously. An illustrating example is shown in Figure 2.1b, extracted from the work of Wolf, et. al.[27] There, 500 nm polystyrene particles are self-assembled on the surface of a flat PDMS substrate. Convective assembly is a simple method to pattern large areas with ordered particles. However, it is limited to very hydrophilic substrates with low water contact angles (i.e., below 20 degrees) and the method is applicable only if sedimentation re-

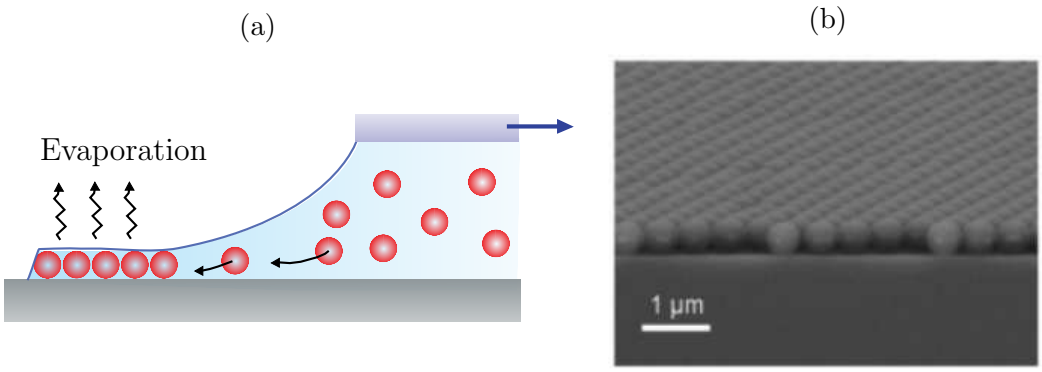

Figure 2.1: (a) Scheme of the convective assembly process. The assembly mechanism is driven by the convective flow of solvent induced by evaporation, leading to the formation of continuous monolayer of packed particles. (b) SEM image of a monolayer of 500 nm PS particles on the surface of a flat PDMS substrate. Figure adapted from Ref. [27]

mains negligible during the assembly. It requires a tight control of parameters. For large enough NPs, the process can be monitored on a microscope, enabling the optimization of parameters during the self-assembly process.[27]

2.1.2 Non Close-Packed Monolayers

Non closed-packed monolayers of particles with controlled separation between individual spheres can be prepared from previously assembled closed-packed monolayers using two different methods: i) Shrinking the particles while keeping their position and ii) Stretching a substrate in order to separate particles.

A popular shrinking method is plasma treatment. Standard plasma cleaning devices are implemented to generate an etching process that reduces the particle size. It was implemented with polystyrene and metal particles[28, 29, 30, 31]. Ordered arrays with adjustable distances and conserving the original hexagonal geometry were fabricated. Figure 2.2 shows an example of an the etching process, where the originally 180 nm particles of a closed-packed monolayer are shrinked in a Ar plasma.

Another shrinking approach to create non close-packed monolayers is to employ core-shell particles with a polymer shell[32, 33]. After immobilization on a substrate, inherent particle shrinking occurs by loss of the swelling solvent during the drying process. A former step with heat treatment to produce the combustion of the organic shell can be used, retaining the non combustible core

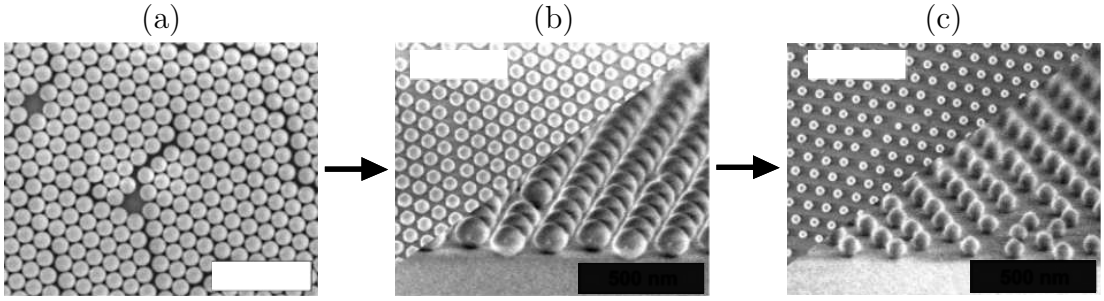

Figure 2.2: SEM images of (a) close-packed monolayer of 180 nm polystyrene particles deposited on a flat glass substrate. (b) after treatment with Ar plasma for 1 min. (c) after and 1,5min. Bottom views in (b) and (c) are titled images. Black scale line: $500nm$. White scale bar: $1\mu m$. Figure adapted from Ref. [29]

positions.[34, 35]. This approach was followed by Férnandez-López et.al.[34] and is shown in Figure 2.3. A non closed-packed monolayer of hybrid Au@PNIPAM core-shell particles is self assembled with a controlled interparticle distance. After that, combustion of the shell is used to produce arrays of Au particles.

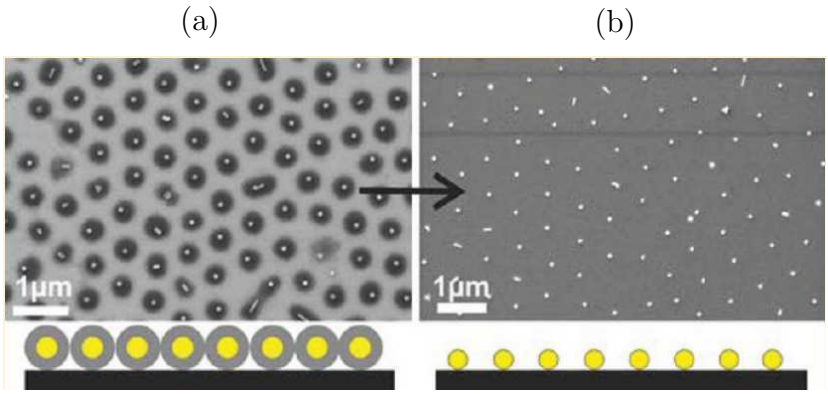

Figure 2.3: SEM images of (a) self-assembled hybrid Au@PNIPAM core-shell particles. (b) Controlled combustion of the organic shell to produce organized arrays of Au particles. Figure adapted from Ref. [34]

The second method to separate particles is to stretch the substrate after their assembly. Flexible substrates such as elastomeric were used for this purpouse[36]. Once the desired separation distance is reached, the colloids can be transferred to a different substrate. More sophisticated elongation protocols can be implemented to create monolayer crystals with nonhexagonal symmetries as for example square lattices.[37]. Figure 2.4 shows an example of a self-assembled closed-packed monolayer of 566 nm silica spheres on a PDMS film that is transformed to a square lattice or to parallel single-sphere wires by different stretching

protocols.[37] Altough these methods show that self-assembled monolayers are

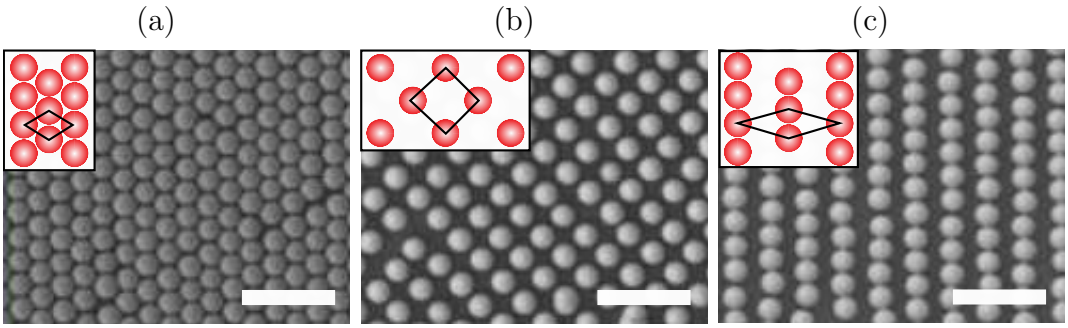

Figure 2.4: (a) SEM image of a closed-packed self-assembled monolayer of 566nm silica shperes on a PDMS film. (b) Square lattice and (c) parallel single sphere wires formed by stretching the PDMS film. Insets show the schematic stretching protocol. Scale bars: 2 μm. Figure adapted from Ref. [37]

not constrained to closed-packed arrays, versatility of design is still limited.

2.2 Template-Assisted Self-Assembly

This section describes the combination of self-assembly methods with the surface modification of the substrate prior to the assembly process. This way, the deposition of particles only takes place in previously selected positions. Two main approaches can be distinguished: physical and chemical modification. Physical patterning modifies the topography of the substrate to provide regions of confinement at which colloids will assemble, as described in section2.2.1. Chemical modification apply surface chemistry in combination with a structuration processes to produce regions with higher and lower affinities for the colloids, as described in section 2.2.2.

2.2.1 Assembly on Topographically Patterned Substrates

Convective assembly can be combined with topographically patterned substrates, extending the range of achievable arrangement of particles to discontinuos 2D structures.[27] The method is depicted in Figure 2.5.a and consist in the incorporation of protrusions that act as obstacles for the motion of particles towards the dryng region. If the solvent film is smaller than the sum of the particle size and the obstacle height, the convective flow is blocked and the assembly is prevented.

On the contrary, the assembly is preserved outside the protrusions. This way a selective deposition is obtained. The topographic patterns can be fabricated by standard lithographic methods. Figure 2.5b shows a 200nm-deep patterned PDMS substrate and Figure 2.5c show the convective self-assembly of 500nm polystyrene particles.

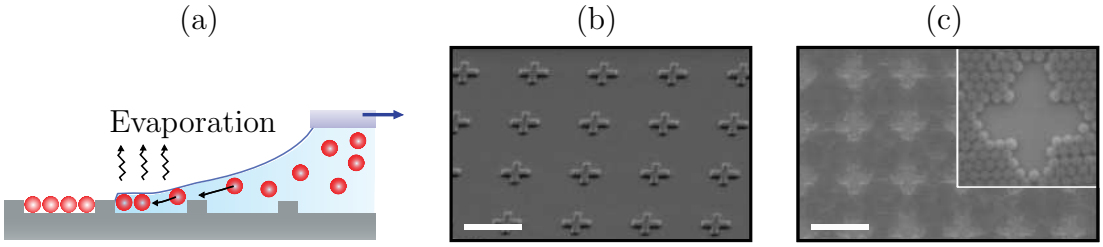

Figure 2.5: Convective assembly. (a) Scheme of convective assembly on patterned substrates. adapted from Ref. [29] (b) SEM image of a 200 nm-deep patterned PDMS subtrate before the assembly of particles. (c) SEM image of a 2D arrangement of 500 nm polystyrene particles. Inset is a 3x magnified image. Scale bars: $5\mu m$. Figure adapted from Ref. [27]

Convective self-assembly is usually limited to continuous structures of particles, such as opal microchannels or stripes of colloidal crystals. Due to its working principle, it is applicable to highly hydrophilic substrates and it is hard to employ it for the fabrication of arbitrary patterns with single particle resolution. On more hydrophobic surfaces, however, the situation is different. The direction of capillary forces changes and the confinement effect decreases when the contact angle of the solvent increases. Above a threshold angle, this force prevents the particle deposition on flat surfaces. In contrast, if a surface is cleverly patterned with holes or depressions, the combined effect of the locally distorted capillary force and the geometrical confinement induced by the hole can be exploited to immobilize single or a small number of particles. This method is known as capillary assembly and is illustrated in Figure 2.6.a. The number of particles that is deposited on each hole and their structural arrangement is controlled by the ratio of sizes between the particle and the hole, as shown in figure 2.6.b. In a work by Flauraud et. al., funneled holes were optimized to trap single Au rods. They report a 100% yield assembly of rods with arbitrary position and orientation with respect to the receding meniscus, as showh in 2.6.c.

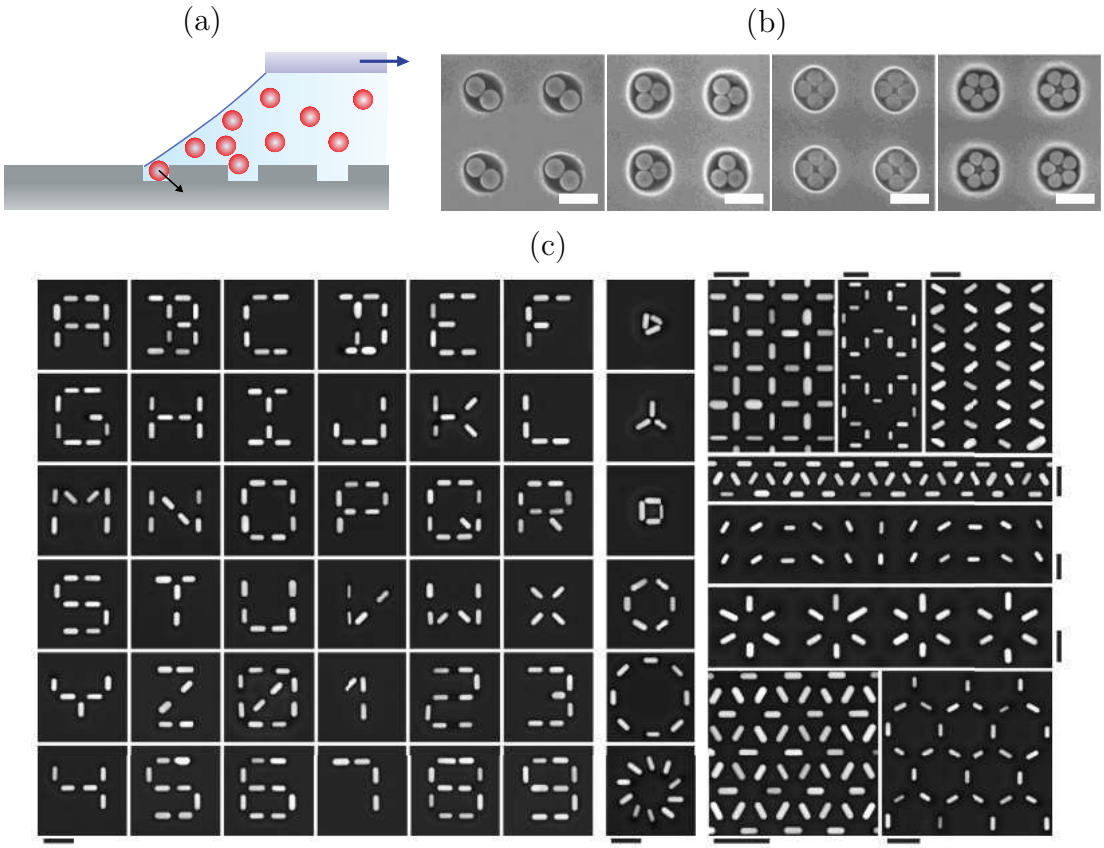

Figure 2.6: Capilarity assembly. (a) Scheme of capillarity assembly on patterned substrates, adapted from Ref. [29] (b) SEM images of polygonal aggregates that were formed by capillary assembly of polystyrene beads on 2D arrays of cylindrical holes. The holes used in all the cases were $2\mu m$ in diameter, and the particle sizes were (from left to right) $1\mu m$, $0.9\mu m$, $0.8\mu m$ and $0.7\mu m$ White scale bars: $2\mu m$. Adapted from Ref [38](c) SEM images of single rod deposition with angular and positional accuracy to form several letters, clusters and geometries. These arrays were obtained using funnelled traps with arbitrary orientations with respect to the receding contact line. All black scale bars: $250nm$. Figure adapted from Ref. [39]

2.2.2 Assembly on Chemically Patterned Surfaces

Combining surface functionalization with lithographic methods, patterns with chemical contrast can be created. In this way, selective deposition is achieved, either by defining regions with lower and higher affinities with the particles or regions with different wetting properties.

Enhanced adhesion to specific areas of a substrate rely on attractive interactions between surface groups on the particles and the substrate, usually elec-

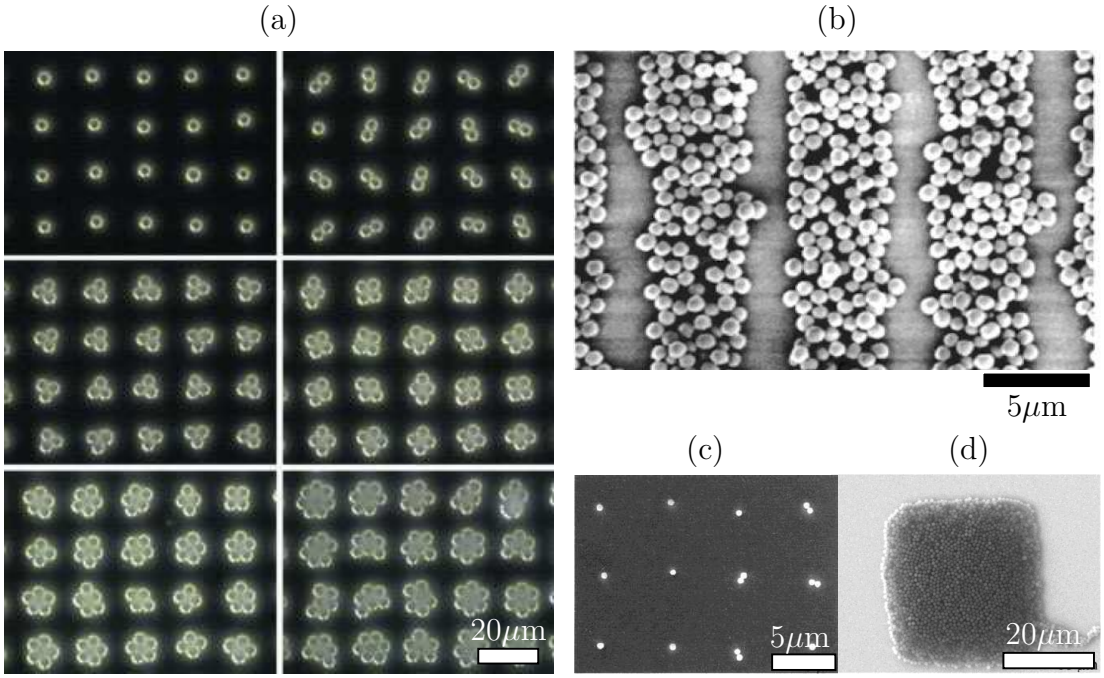

Figure 2.7: Assemblies on chemically patterned surfaces. (a) Optical images of 2D colloidal arrays on circular patterned polyelectrolyte templates. The number of colloids on each clusted is controlled by the diameter of the polyelectrolyte circle. Figure adapted from Ref. [40].(b) SEM image of silica spheres bound by electostatic attraction on stripes of polyelectrolytes. Adapted from Ref. [41] (c) 0.8 μm single polystyrene spheres deposited on small hydrophilic regions (d) Square close-packed array of particles assembled by hydrophobicity contrast. Adapted from Ref. [42]

trostatic, hydrogen bonding or Van der Waals. In the work by Hammond et. al.[40], a periodic array of circular features of a positively charged polyelectrolyte was implemented. Then, a colloidal suspension of negatively charged carboxylated polystyrene particles was put on top of the surface. Changing the size ratio between the polyelectrolyte area and the particle radius, the number of assembled particles is controlled. Figure 2.7.a shows the obtained colloidal arrays. In another work[41], a similar approach was used to create extended patterns with many particles. Figure 2.7.b show large stripes of particles. In general, extended arrays produced by this method are disordered. Strong attachement of particles to the substrate impedes the lateral freedom of movement required for self-organization into ordered structures.

An example of wettability contrast method is the work by Fan et.al[42]. They created patches of hydrophilic domains functionalized with carboxylic acid, sur-

rounded by a methyl terminated hydrophobic surface. A drop of colloidal solution of 800 nm polystyrene spheres is allowed to dry on top of the substrate. As the drop recedes, spontaneous dewetting from hydrophobic domains and flow to hydrophilic regions occurs, carrying the suspended particles, which deposit there as the fluid evaporates. With this method, square regions covered with colloids were obtained, as shown in figure 2.7.d. Also, single particle depositions in small wet regions is possible, although, as shown in figure 2.7.c, the regulation of the number of particles is not fully controlled.

2.3 Photodynamic Assembly

In self-assembly methods, NPs organize according to their thermodynamically most stable configurations and therefore their versatility to form arbitrary arrays is limited. Template-assisted assembly adds flexibility of pattern design, but requires additional steps than lengthen and complicate the fabrication procedure. Combination of multiple types of particles is also difficult.

Photodynamic aseembly methods offers the possibility to overcome all of these drawbacks. [43] With the help of optical forces, NPs can be trapped, delivered and fixed at any desired position on a surface. In this way, arbitrary arrays of particles can be created without the need of any substrate patterning, previous or after the assembly process. One of the first reports of such an approach was published in 2002 by van Blaaderen et.al.[44]. There, they built optical tweezers with a continuous wave infrared beam (λ = 1064 nm) focused to a diffraction-limited spot. The tweezers were used to pick up 700 nm silica particles from a reservoir, drag them in position and then fix them by shifting the focus of the tweezers toward the surface, where opposite surface charges are used to immobilize the particles. In this way patterns like the one shown in figure 2.8a were created. The same year, Ito et.al[45] also employed a (λ = 1064nm) continuous wave beam to trap single 80nm gold NPs and bring them close to a substrate. There, a nanosecond pulse of ultraviolet laser fixes the particle to the surface, by partially funding it and therefore enlarging the contact area with the surface. Figure 2.8.b shows a AFM image of a pattern with eight fixed particles. In 2009, in a work by Lee et.al.[46], controlled deposition of optically trapped high aspect-ratio In_2O_3 nanowires was realized by fast-scanning the trapping beam to rotate the nanowires and connect two branches of a circuit, as shown in 2.8c. A subsequent annealing

step provided electrical contact between the nanowire and the electrodes.

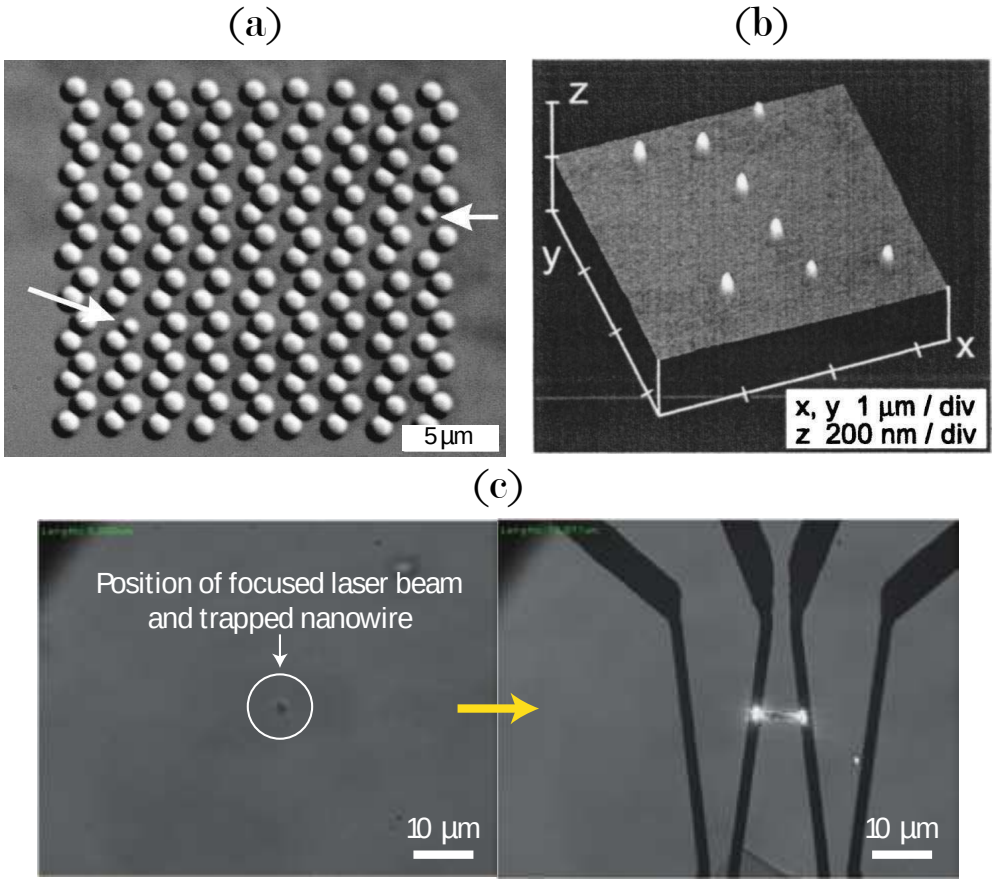

Figure 2.8: (a) Optical image of a pattern of 700nm radius silica particles arranged on a hcp lattice by optical printing. The arrows indicate two smaller particles that have been deliveratly incorporated as defects in the pattern. Adapted from [44]. (b) AFM image of fixed and patterned gold nanoparticles. Adapted from [45]. (c) Optical manipulation of a In_2O_3 nanowire (left) and placement to connect two branches of a circuit (right).Adapted from [46].

In 2010, Scherer et.al.[47] presented an all-optical method to deposit single Au NPs with a size of 40 nm on glass substrates directly out of solution. The substrates were functionalized with a positive polyelectrolyte, which provided a repulsive interaction with the positively charged NPs, preventing their spontaneous deposition. The patterning method consisted on trapping a particle with a $\lambda = 817$ nm wavelength optical tweezers, at some distance away (typically 10 μm) of the substrate, as depicted in figure 2.9a. Then, by manually changing the fine focus on the microscope, the trapped particle could be brought in contact and fixed to the surface due to strong van der Waals forces, as depicted in figure (2.9b). After that, a piezoelectric stage was used to move the sample to a given

position in the lateral (XY) plane, where the next particle would be fixed. In this way, patterns were created, as shown in figures 2.9c and 2.9d.

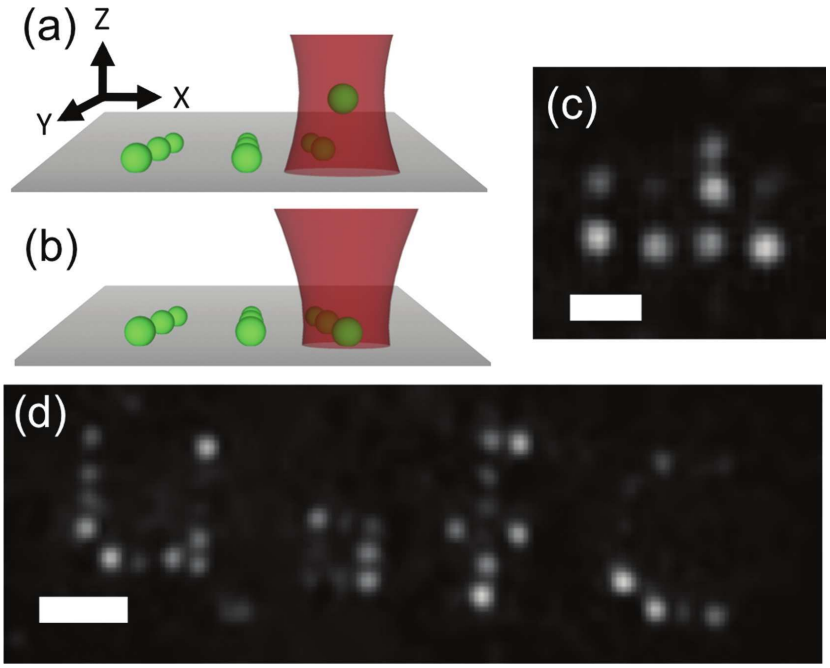

Figure 2.9: Schematic of single nanoparticle trapping (a) and deposition (b). (c) Dark-field image of typical pattern used for the determination of the precision of deposition (scale bar 2 μm). (d) "U of C" pattern created from 37 single nanoparticles (scale bar 5 μm). Figure reproduced from[47].

Simultaneously to Scherer's paper, Urban et.al.[48] demonstrated the patterning of surfaces with 80 nm Au NPs. The method is similar, but they employed a laser beam tuned to the particle localized surface plasmon resonance (LSPR). In this way, particles where fixed directly out of the solution using the radiation pressure of light, without any previous stable trapping step. This technique is called optical printing and is extensively reviewed in chapter 3.

Employing optical forces is not the only way that far-field radiation can allow patterning of surfaces with colloidal NPs and flexibility of design. For example, in 2015, Lin et.al.[49] employed a laser beam to generate microbubbles at the interface of a colloidal suspension and a plasmonic substrate, in a technique called Bubble-pen lithography. The bubble captures and immobilizes the particles on the surface through coordinated actions of Marangoni convection, surface tension, gas pressure, and substrate adhesion. Moving the beam, they created particle assemblies and single-particle patterns, as shown in figures 2.10a and 2.10b. Another family of techniques are known as Optoelectronic Tweezers[50]

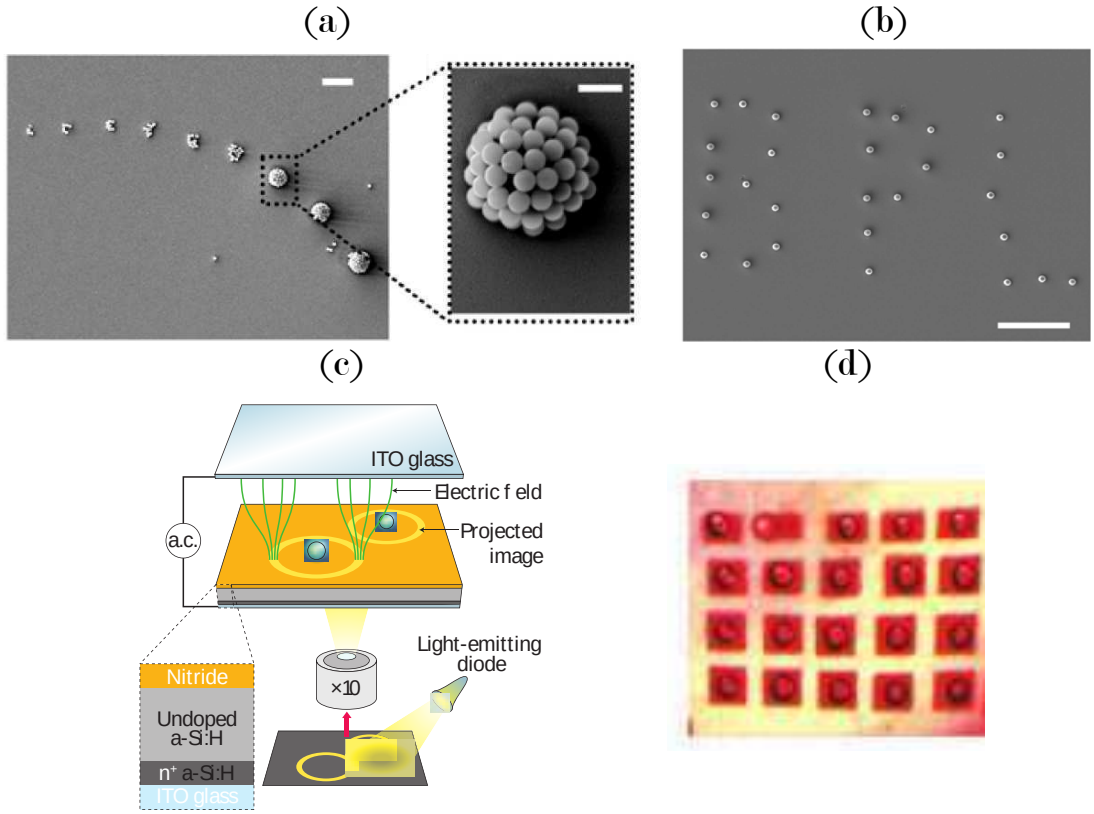

Figure 2.10: (a) SEM image of patterned 540 nm PS beads at different laser powers using Bubble-pen lithography Inset: Magnification of one of the fabricated arrays. (b) Patterning of 940 nm PS beads with single-particle resolution using bubble-pen lithography. Adapted from[49]. (c) Outilne of optoelectronic tweezers. A liquid containing particles is sandwiched between a transparent electrode and a photoconductive electrode. Light patterns from a digital projector are imaged by an objetive onto the devide. The image, together with an a.c. electrical bias, generates dielectrophoretic traps in the illuminated areas. (d) A 4x5 array of dielectrophoretic traps, each one containing a 20 μm polystyrene particle.

and are outlined in figure 2.10c. These techniques make use of both light and an electric bias to sculpt a potenial landscape on a photosensitive substrate. Light then creates virtual electrodes. The resulting non-uniform electric field exerts dielectrophoretic forces on particles, that are used to create potential wells. In this way, particles are trapped on the illuminated areas. Figure 2.10d shows an array of 20 μmpolystyrene beads fabricated through this method.

3

Optical Printing

The aim of this chapter is to present the state of the art of optical printing. In section 3.1 the first paper on optical printing is described, and therefore the working principles of the technique are introduced. Then, a summary of relevant progress during the last years is presented in section 3.2. Finally the open questions and current challenges of optical printing are discussed in section 3.3.

3.1 Fundamentals of Optical Printing

Optical printing is a simple and versatile method to fix colloidal NPs from suspension into specific locations of a substrate using optical forces, as outlined in figure 3.1a. It was introduced by a paper by Urban et. al.[48] in 2010. Unlike other approaches, in this work NPs were fixed directly out of a colloidal suspension without previous stable 3D trapping. A colloidal suspension of NPs, stabilized by electrostatic repulsion between NPs, was put in contact with a substrate. Spontaneous adsorption of the NPs onto the substrate was avoided by preparing the substrate to be charged with the same sign as the NPs. The functionalization of the substrate was achieved trough the layer-by-layer assembly of a monolayer of a charged polyelectrolyte[51].

In addition to the electrostatic repulsion $F_{elect}(z)$, an attractive Lifshitz-van der Waals force $F_{LvdW}(z)$ acts at short separation distances between the NP and the substrate. The total interaction $F_{DLVO}(z) = F_{elect}(z) + F_{LvdW}(z)$ is given by the Derjaguin-Landau-Verwey-Overbeek (DLVO)[52] formalism, by differentiation of the interaction energies between a charged sphere and a charged

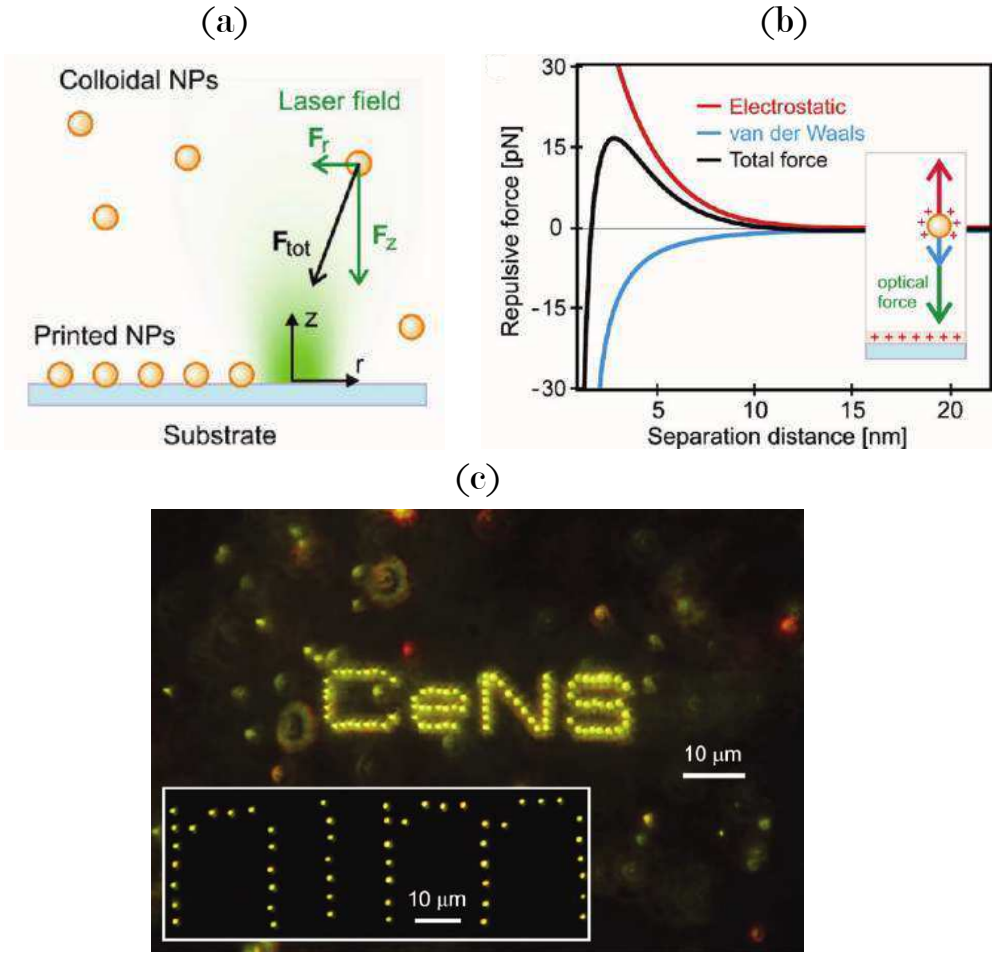

Figure 3.1: (a) Schematic representation of the optical forces acting on a NP during the printing process. (b) Calculated dependence on distance of the electrostatic, van der Waals, and total forces acting on a positively charged Au NP in the vicinity of the positively charged surface (c) Dark-field image of two patterns made by optical printing single 80nm Au nanoparticles (NPs) . Bright spots out of focus around the pattern are individual NPs freely floating in the colloidal suspension. Adapted from [48], where details of the calculations are provided.

surface[53].

$$F_{elect}(z) = \pi\epsilon_m a\kappa \left(\zeta_s^2 + \zeta_p^2 - 2\zeta_p\zeta_s e^{\kappa z}\right)\left(\coth\left(\kappa z\right) - 1\right)$$

$$F_{LvdW}(z) = \frac{2Aa^3}{3z^2\left(z+2a\right)^2} \tag{3.1}$$

where z is the distance of the particle to the surface, a is the particle radius, ζ_s and ζ_p are the zeta potential of the surface and the particle respectively, A is the

Hamaker constant and k^{-1} is the thickness of the electric double layer. Figure 3.1b shows the calculation of both forces and the total force. As can be seen, there is a barrier that prevents deposition of the NPs on the substrate. The basis of optical printing is overcoming this barrier on specific locations of the substrate by applying optical forces on the NPs . For this aim, a laser beam is highly focused onto the sample plane, generating a small region where axial optical forces are stronger than the repulsion. There, the NPs can pass the barrier and be so close to the surface that they get fixed by the attractive van der Waals force. When this happens, it is said that a NPs is printed.

Since optical forces decrease rapidly with the distance to the focal plane, only those particles that are close to the focal volume experience a force strong enough to overcome Brownian motion and be guided to the surface. This means that NPs are free to diffuse in the solution until they reach the focal volume and get printed. Urban et al. monitored this stchocastic process live using dark field microscopy. When a NP was printed, they y moved the substrate to another position, where the following particle should be printed.In this way, surfaces were patterned with arbitrary arrays, as shown in figure 3.1c. Interestingly, none of the reddish and therefore different particles present on the NPs solution is printed on the arrays, showing the selectivity of the optical printing.

3.2 Review of Optical Printing

In sections 2.3 and 3.1, two fundamental papers demonstrating optical patterning of surfaces with Au particles were introduced. Urban et.al paper[48] was from the Photonics and Optoelectronics group, directed by Prof. Jochen Feldmann in Munich. Guffey et.al.[47] paper was from Prof. Norbert Scherer Group in Chicago. They were both published in the same volume of the journal *NanoLetters*. After these fundamental papers from 2010, the same two groups were responsible for almost all the published papers on the subject, which are described in this section.

Although the magnitude of optical forces is usually very small for sub-micron particles, the plasmonic properties of metallic nanoparticles (MNPs) were used to enhance their interaction with light. On the other hand, the strong dependence of optical forces on the particle nature can be exploited for sorting and selective printing of a single type of MNPs out of a mixture.[54]. This was already observed

on Urban et. al. first paper, and then exploited by Huergo et. al. to separate and study the different outputs of a chemical MNPs synthesis. [55] For that, they employed several lasers with wavelengths tuned to localized surface plasmon resonance (LSPR) of each type of nanoparticle.

Simultaneos optical printing of multiple NPs in an ordered fashion is also possible using spatially modulated light fields. In the work by Nedev et.al[56], a laser beam is split into several beams, creating an optical pattern which allowed the parallel printing of up to 64 Au NPS, as shown in Figures 3.2.a and 3.2.b. In another work by Bao et.al.[57] ring-shaped and line optical traps were implemented in order to print Ag NPs, as shown in Figures 3.2.c and 3.2.d. These approaches have the advantage of being faster. Typically the required time for printing the hole pattern is similar to the characteristic time of printing a single particle with a convectional beam. The pattern can be shifted, allowing the fast assembly over larger areas, or it can be modified at high speed enabling the formation of complex patterns.

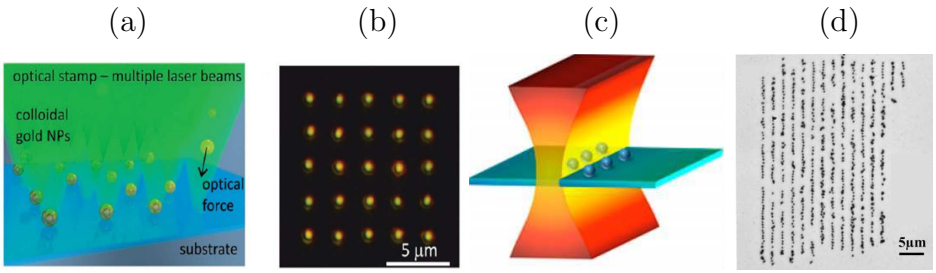

Figure 3.2: Multiplexed optical printing. (a) Scheme of Optical Printing with multiple laser beams. Adapted from [56] (b)) A dark-field image of a square pattern of 80 nm Au NPs printed with multiple beams (c) Scheme of Optical Printing with a line trap. Adapted from [57]. (d) Optical transmission image of printed 200 nm Ag NPs array formed using a line trap.

Angular control in the optical printing of Au nanorods was demonstrated using a two-color approach.[58, 59] A laser beam, not being resonant to the plasmon resonances of the nanorods is used for stable trapping of an individual rod. Optical torque in the trap aligns the rod with the direction of polarization of the beam. After that, a second resonant beam is used to print the rod on the subtrate, maintaining the orientation. Figure 3.3 shows oriented arrays of 41 x 114 nm Au rods. Optical printing is not limited to the fabrication of devices based only on colloidal particles. It can also be used to incorporate a particle into a specific position of a complex surface. In the work by Do et.al.[60], optical

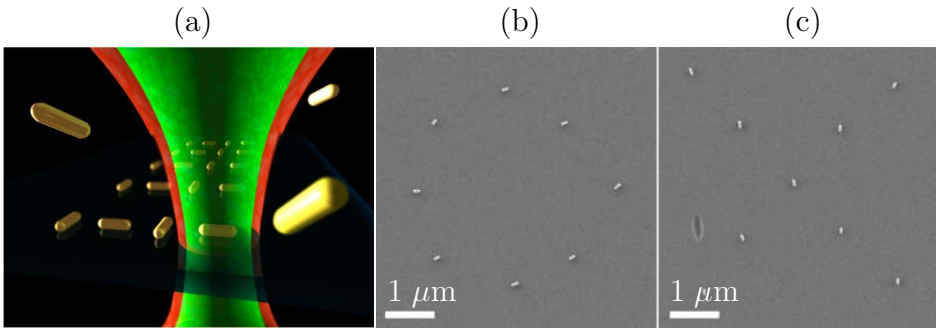

Figure 3.3: (a) Scheme of two focused beams superimposed for the printing of oriented nanorods. (b) and (c) SEM images of an "OX" pattern of printed gold nanorods with angular control. The orientation of the nanorods in the two letters is perpendicular. Figure adapted from [59]

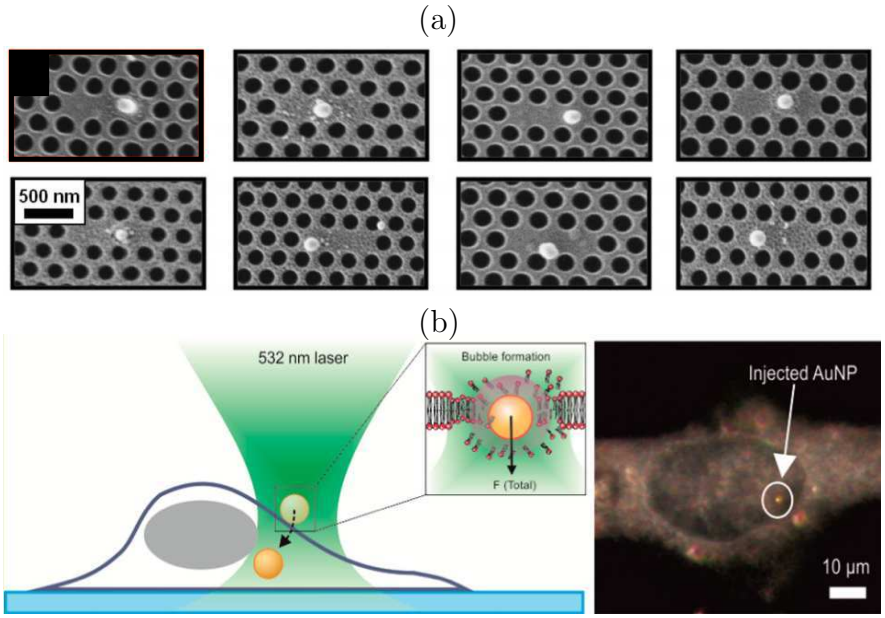

Figure 3.4: Optical printing on complex surfaces. (a) SEM images of a series of photonic crystal nanocavities containing optically-printed 150 nm gold nanoparticles in controlled positions. Figure adapted from [60] (b) Printing and injection of gold nanoparticles into living CHO cells. Adapted from [61]

printing was used to position a 150 nm Au glsNP onto a sub micrometer linear three-hole defect of a photonic crystal, as shown in figure 3.4a. This allowed the fine tuning of the electromagnetic interaction between the glsNP and the cavity mode. In another work by Li et.al.[61], Au particles were patterned on the membrane of living CHO cells and, in a former step, injected into the cell through a combination of plasmonic heating and optical forces (Figure 3.4b). The survival rate of the cells was above 70%.

3.3 Open challenges

One of the open questions of optical printing concerns its positional accuracy. Despite being an optical method, the positional accuracy of optical printing is not limited by diffraction of light, and individual NPs can be positioned with a precision of several tens of nanometers. In the first report by Urban et.al[48], they measured the precision by printing 80nm Au NPs along a line and determining the position through a Gaussian fit of the dark field images, as shown in figures 3.5a and 3.5b. They found the average deviation from the line to be $\sim$ 50nm. They also comment that increasing the laser power lead to larger deviations. On the other hand, in the paper by Guffey et.al.[47] used light out of resonance (λ = 817nm) to first trap and then print 40nm Au particles. The accuracy of the deposition was found to be around $\sim$ 100nm, which is larger than the standard deviation of particle's position fluctuations within the trap $\sim$ 30nm. On the contrary to Urban paper, they comment that the best precision is obtained for high powers. It remains unclear whether these precision values constitute a

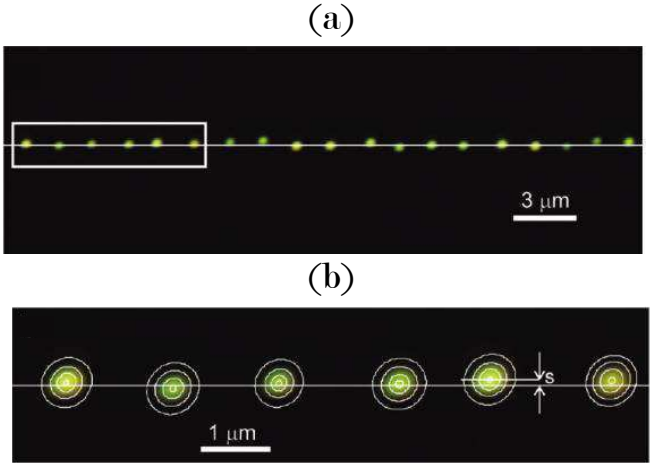

Figure 3.5: (a) Dark field image of a line of printed Au NPs used to estimate printing accuracy. White line is the target line. (b) Detail of the area marked by the rectangle in (a) including the results of the 2D Gaussian fit of each particles used to determine NPs position. Figure adapted from[48]

fundamental limit, or they respond to a particular set of experimental parameters. The interaction of NPs with light depends not only on the beam wavelenght, power and shape but also on the particle composition, size and shape. Also, Brownian fluctuations, enhanced by (wavelenght dependent) plasmonic heating were proposed as a source of error[47, 56]. Understanding the printing mechanism

by unravelling the role of each parameter in the final precision is the key to achieve super precise optical printing. In chapter 5 this subject is address.

The other main challenge of Optical Printing concerns its lateral resolution, understood as the minimum distance at which two particles can be printed in a controlled manner. In different experiments the minimum interparticle distance for controllably printing has been found to be restricted to about 300 nm.[62, 63] This has obstructed the use of optical printing to the fabrication of plasmonically coupled structures and circuits of connected NPs. About this subject, in a paper from 2014, Scherer et. al.[57] stated: *most reports so far are limited to relatively large interparticle separation, typically* > 1 μm. The same year, in another work, Feldmann et. al.[62] wrote: *One of the problems existing for all of these techniques is an apparently fundamental limitation of the minimal distance between controllably printed nanoparticles, which could not be reduced much below 300 nm.*

In a workaround to this limitation, NPs printed on glass were transferred into a thermoresponsive polymer film. Then, the film was heated above 165° causing its contraction and bringing particles closer together.[63] The process is depicted in Figure 3.6a and examples are shown Figure 3.6b. The distance between printed 80nm Au particles was reduced by a factor of 2.3. Still after this procedure, the interparticle distance was limited to about 120 nm.

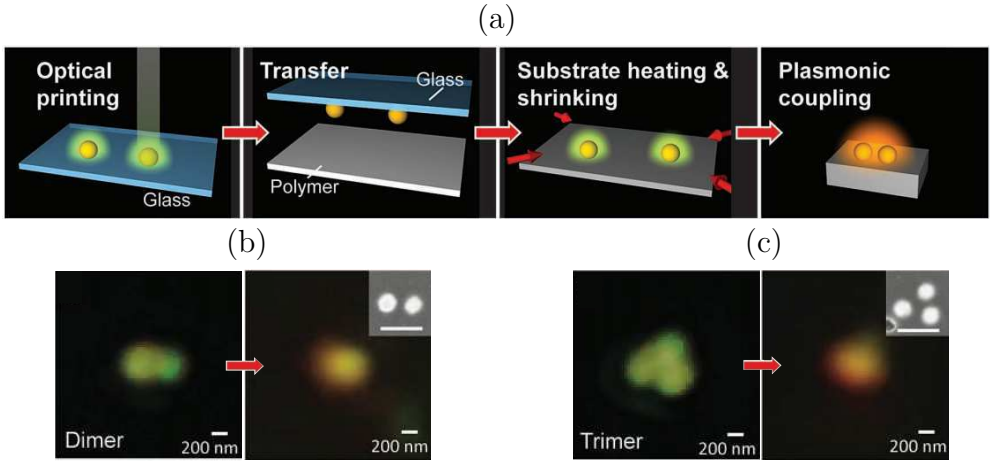

Figure 3.6: Shrink to bring closer. (a) Scheme of the method. First, Au NPs are printed on glass, then transferred to a thermoresponsive polymer film by. After that, the film was heated and shrunk, reducing the distance between particles. Dark field images of a Au dimer (b) and trimer (c) whose separation is reduced from 280 to 120 nm. Insets: SEM images of the shrunk arrays. Figure adapted from [63]

In 2014, Scherer et.al. published the first paper where the lateral resolution was systematically studied.[57] They used the line traps schematized in figure 3.2c to print the chain patterns of 200 nm Ag NPs shown in figure 3.2d, using a wavelenght of 800 nm. They measured the interparticle separation inside the line. The distrubution of separations is shown in 3.7a. The interparticle separation shows a dominant sharp peak at (580 ± 84) nm, which suggest the presence of a strong repulsive interaction. In the same work they studied the influence of a previously deposited nanoparticle chain on the printing of a subsequent parallel chain, as a function of the distance between chains Δx. Three regimes with distinct printing behaviors were observed, as shown in Figure 3.7.b . A noninteracting (green shaded) regime, with $\Delta x > 600$ nm where the printing is independent of the previous chain. An interacting (yellow) regime is characterized by deviations of the particles being printed toward distances larger than expected, for 600 nm $> \Delta x >$ 300 nm. Last, an unstable regime (pink) occurs for $\delta x < 300$ nm, resulting in the loss of control of the printing process. Some of the incoming particles are printed onto the existing chain, forming aggregates.

These results were explained and understood *"in terms of optical binding interactions."* Upon illumination, printed NPs scatter light, which can exert optical forces on the particles being printed. This mutual interaction between particles through light scattering are usually referred to as *Optical Binding.*[65]. An extensive review on optical binding can be found in Zemanek et.al.[66]. Typically, optical binding forces are long ranged and are both attractive and repulsive.

In order to explain their experimental observations, Scherer et.al. calculated the optical binding forces produced by a pair of illuminated 200nm Ag fixed spheres on a third particle, as shown in figure 3.7c. The forces lead to a stable equilibrium position, at a distance of about one wavelength of the fixed particles. In the same line of thought, in a review from 2014 about optical printing by the Feldmann group[62], it is stated that the limitations in the lateral resolution of the technique are *"most likely due to the scattered light from an already printed nanoparticle interfering with the incident light field and creating energetically favourable positions at large distances from the affixed nanoparticle".*

An alternative explanation of the limited lateral resolution was given in 2013 by Urban et.al. Where they wrote that *"because the already printed nanoparticle is still illuminated by the laser, it can heat up and create convective currents, disrupting the path of the second nanoparticle."*[63]

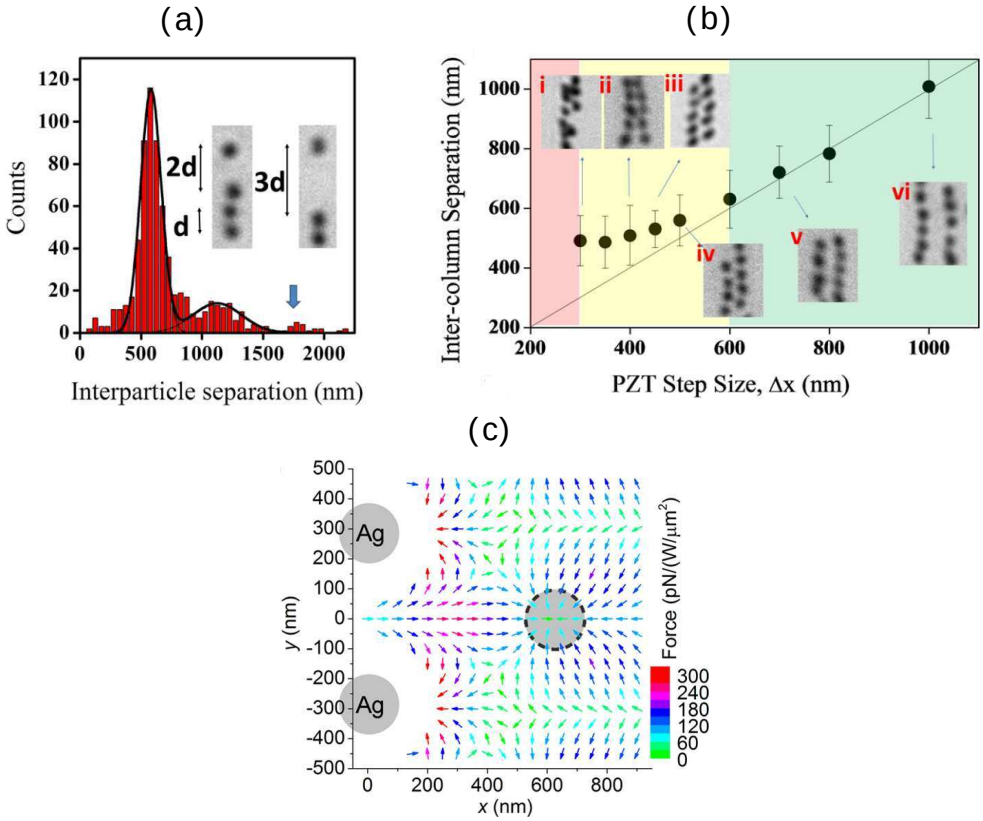

Figure 3.7: (a) Distance distribution of adjacent Ag NPs inside a chain. The black curve is a two-peak Gaussian fit to the distribution with means and standard deviations of (580 ± 84) nm and (1125 ± 91) nm for the two peaks, respectively. (b) Nanoparticle inter chain achieved separation vs set separation Δx. Inset: representative optical images of the deposited arrays. (c) Map of the force exerted by the central pair of 200 nm Ag NPs (the gray spheres) on a new 200 nm Ag glsNP in water illuminated by a plane wave (λ_m = 800nm vacuum wavelength). The polarization is along the x-axis. The direction of each arrow denotes the direction of the optical force when the third nanoparticle is located at the midpoint of the arrow. The colours of the arrows represent the value of electrodynamic forces as shown by the scale bar. The dashed circle represents the equilibrium position of the newly added NP. Figure adapted from [64]

In chapter 6, the different proposed mechanisms are systematically studied and discussed. Understanding the underlying physics is the key to design strategies to overcome this impediment and allow the optical printing of particles at any arbitrary given inter-particle distance. This would dramatically expand the versatility and complexity of devices that can be fabricated with optical printing.

4

Experimental set-up for automated multi-color optical printing

The scope of this section is to describe the experimental set-up that was specifically designed and developed for the experiments in this thesis. The set-up is detailed in section 4.1. Also, a custom software was develop to control and automate the measurements, as described in section 4.2

4.1 The set-up

The setup is schematically depicted in Figure 4.1. It consists of a home-built upright optical microscope that combines three different techniques: i) Dark-field imaging in wide field. ii) Multicolour sample scanning confocal microscopy. iii) Scattering and micro-Raman spectroscopy.

Sample scanning is performed with an XYZ piezoelectric stage (PI P-545) with nanometer precision and a range of 200 μm in the three axes. Three continuous wave lasers of 405nm (Cobolt), 532nm (Laser Ventus) and 640nm (MPB) are used for both printing and as illumination sources for confocal imaging and microspectroscopy. The polarization of each beam is controlled independently using corresponding $\lambda/2$ and $\lambda/4$ waveplates. Beams are spatially filtered using single-mode optical fibers. They are combined into a common optical path towards the sample using suitable dichroic beam splitters. Each laser path includes a mechanic shutter and a neutral density filter mounted on a motorized flipper,

both controlled from the computer. This way the beam can be blocked, or its intensity switched between two values by including or removing the filter from the path. This is useful when the same laser is used for both printing and scanning but different intensities are needed for each application. Since the filter is placed before the fiber coupling, the beam does not move in the sample plane when the filter is included.

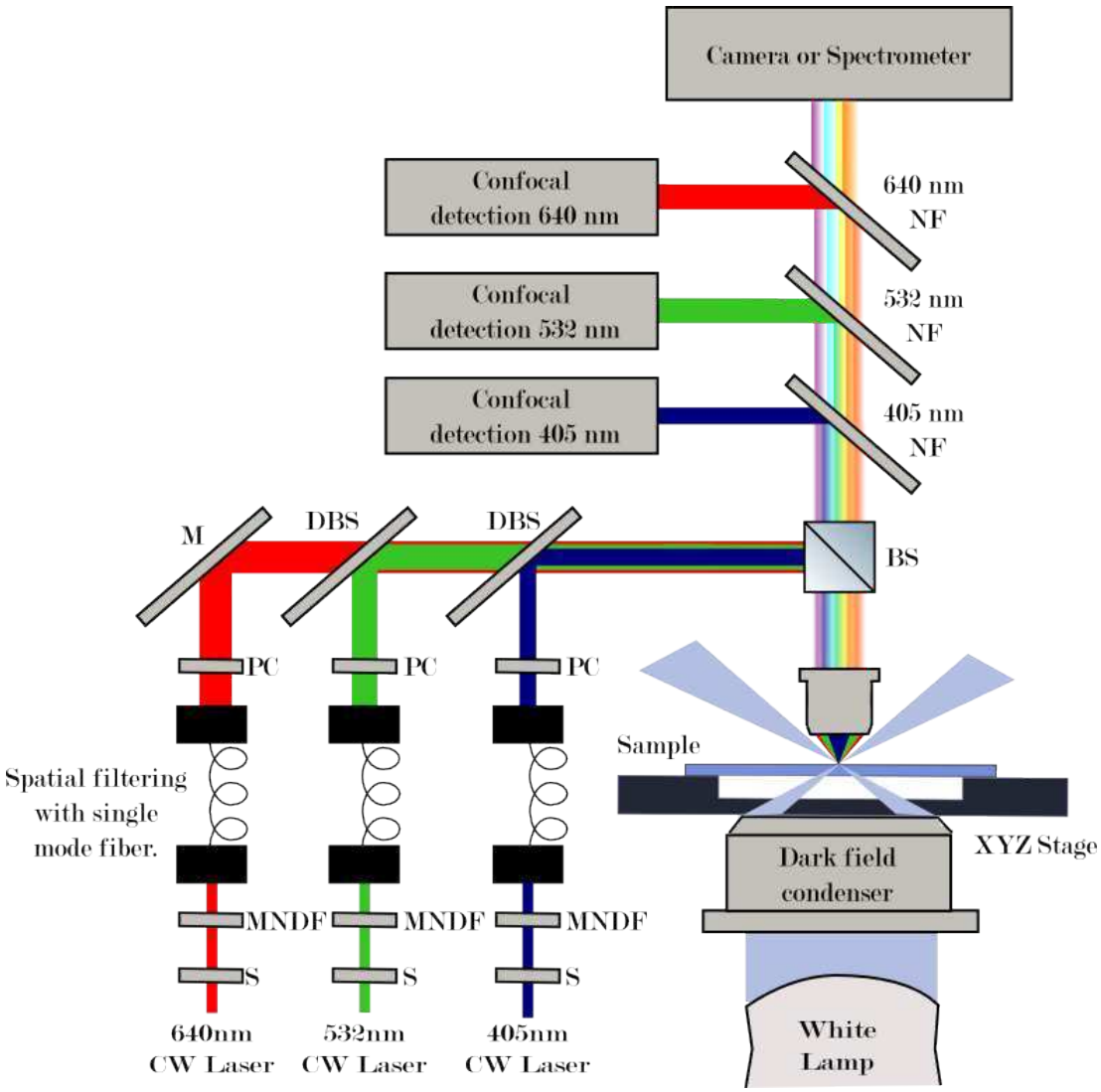

Figure 4.1: Scheme of the experimental set-up. M:Mirror, DBS:Dichroic Beam Splitter, BS:Beam Splitter, NF:Notch Filter, S: Shutter, MNDF: Motorized Neutral Density Filter. PC:Polarization control, consisting in a $\lambda/2$ and a $\lambda/4$ waveplate. Confocal detection boxes are explained in figure4.2a

Dark Field Microscopy

Dark Field microscopy is an imaging technique were the illumination is engineered to enhance image contrast based on scattering. Using an oil-immersion dark-field condenser with a numerical aperture NA=1.2-1.4, light from an halogen white lamp is shaped into a hollow cone and directed towards the sample. Imaging of the sample plane was performed using an water-immersion objective of NA=1, and therefore the oblique rays illuminating the sample are not collected by the objective and do not contribute to the image. Only light scattered by objects in the sample is collected and sent to a camera. This is the reason why images acquired with this technique have usually a dark background with bright objects on it. The microscope has two cameras: A CMOS colour camera (Canon EOS-500D) and a EM-CCD (Andor Ixon3), both connected to a PC. With these cameras it is possible to acquire wide field images and videos, as shown in Figure 4.3b. Notch filters are used to filter light from the laser beams and avoid damaging of the cameras.

Confocal scanning imaging of metallic nanoparticles (MNPs)

The configuration for confocal detection is depicted in Figure 4.2.a. A small circular aperture called pinhole is included in the conjugated plane of the sample plane. Light from the sample plane crosses through the pinhole and is detected by the photodiode. On the other hand, most of the light coming from an object in a different plane does not cross the pin hole and is blocked. For illumination, the beam size of the three lasers is chosen to overfill the pupil of the objetive, and its collimation lens are adjusted to assure that the three beams are focused to its diffraction limit on the sample plane. Using notch filters, elastically scattered light is separated and sent to respective amplified photodiodes through confocal detection. The advantage of using notch filters on this configuration is two-fold i) They filter light from the laser beam, avoiding damage of the cameras and ii) Dark field detection is barely affected and can be perform simultaneously to confocal scanning, because only a small portion of the optical spectrum is filtered

A computer routine was programmed for synchronously scanning the sample and measuring the signal in the photodiode, (see section4.2). This way images can be acquired, using the elastically scattered light of the laser beams by the sample. When scanning a MNPs, it is important to note that the confocal images have two contributions: i) Light scattered by the MNP and ii) Light reflected at

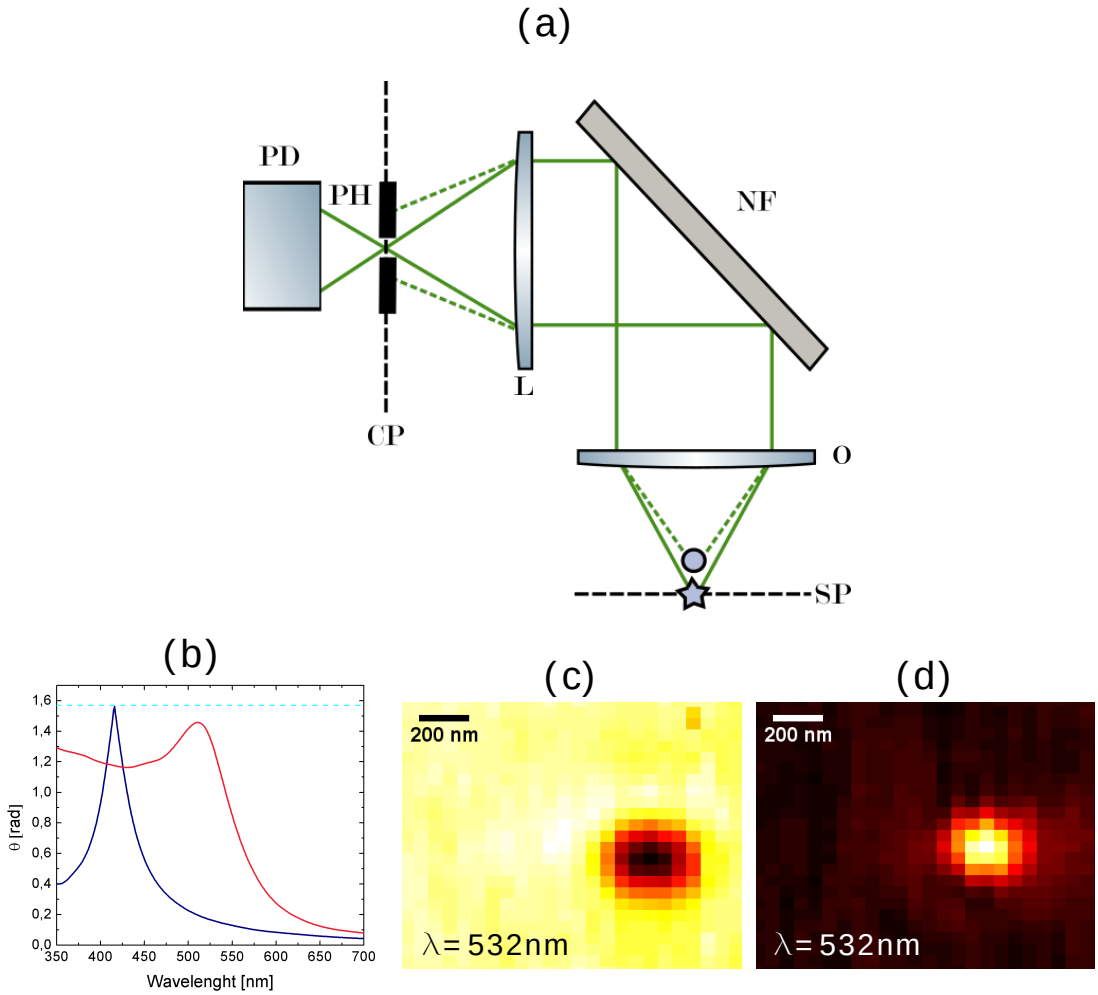

Figure 4.2: Confocal Detection. (a) Scheme of the confocal filtering of the out of plane light. Light from an object (star) in the Sample Plane (SP) is collected by the objective (O) and focused by a convective lens (L) on the conjugated plane (CP), where it crosses a pin hole (PH) and is detected by the photodiode (PD). Light from an object out of plane (circle) is blocked by the PH. (b) Phase θ of the polarizability as a function of wavelenght, for Ag and Au 60 nm shperes, calculated using equation 1.8. Confocal images of (c) Ag and (d) Au 60 nm spherical nanoparticles (NPs) on glass at $\lambda = 532$ nm. Lighter colours indicate higher intensity.

the water/glass interface. Since the illumination laser is a coherent source, these two signals can interfere (constructively or destructively) at the detector. Let E_i denote the electric field of the illumination beam focused onto the sample. Reflected light will contribute to the field in the detector with an amplitude of $E_r = rE_i e^{-i\left(\frac{\pi}{2}+\phi_0\right)}$ with r the effective reflection coefficient,$-i\frac{\pi}{2}$ the phase shift in the reflection and ϕ_0 a phase associated with optical path from the sample to the

detector. Scattered light can be thought as the far field radiation of the induced dipole at the MNP, therefore proportional to its polarizability $\alpha = |\alpha|e^{i\theta}$. The scattered field at the detector can be written as $E_{sca} = sE_i = |s|e^{i\phi}E_i$, with the modulus $|s| \propto |\alpha|$ and the phase $\phi = \theta + \phi_0$. The intensity measured at the detector is then given by

$$I_{det} = |E_r + E_{sca}|^2 = E_i^2 \left(r^2 + s^2 + 2r|s|cos\phi_{rs}\right) \tag{4.1}$$

With $\phi_{rs} = \theta - \frac{\pi}{2}$ the relative phase between reflected and scattered field. It is interesting to note that while the first (reflection) and second (pure scattering) terms are always positive, the third term (interfence) can be negative. In certain conditions, the interference term dominates and MNPs appear dark in confocal images, with a minimum of intensity in its centre. Recalling equation 1.5, $|s| \propto |\alpha| \propto a^3$ and $s^2 \propto a^6$. This means that for large MNPs the pure scattering dominates and particles appear bright in the images, while for smaller particles the interference term dominates and particles appear dark. The transition size between bright to dark depends on the value of the reflection coefficient r and the phase of polarizability θ.

These properties of MNPs can be exploited to detect and localize particles with a weak pure scattering signal: even if $|s|$ is too small, the interference term is still proportional to $|r|$ and thus comparable to the background.[67] For a given MNP size, transition from bright to dark can also occurs if the wavelength is changed. Figure 4.2.b shows the phase θ of the polarizability as a function of wavelenght, for Ag and Au 60 nm shperes, calculated using Kuwata model (equation 1.8). Figure 4.2c shows a confocal image of a Ag 60 nm sphere on glass at $\lambda = 532$nm. At this wavelength the phase of the MNP polarizability is close to zero and therefore destructive interference produces a minimum of intensity in the detector and the sphere is visualized as a dark spot on the image. On the other hand, if a Au shpere is scanned at the same wavelength, the phase of the polarizability is close to $\frac{\pi}{2}$, causing constructive interference in the detector and the particle is seen as a bright spotin the image, as shown in figure 4.2d.

Polarization-resolved scattering spectroscopy

A scheme of the optical set-up for spectrally resolved measurements is shown in Figure 4.3a. Light from a white light lamp that is scattered by the sample is col-

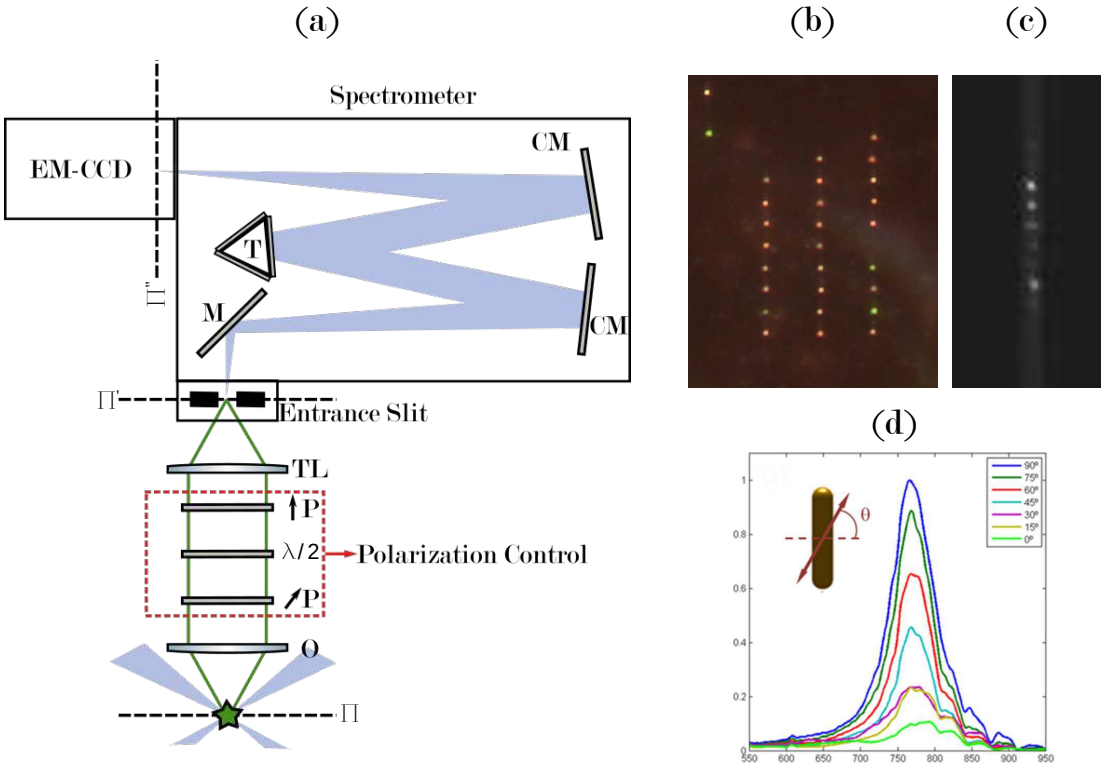

Figure 4.3: Spectroscopic measurements. (a) Scheme of the experimental set-up O: objective lens. TL:Tube lens. M:Mirror. CM: Convex mirror. T:Torrete that allows choosing between two different diffraction gratings or a mirror. Π, Π′ and Π″ are conjugated planes. (b) Dark field image of an array of single Au nanorods on glass, taken with the colour camera. (c) If the mirror is chosen in the torrete, dark field imaging with the black and white camera is possible. The entrance slit is closed to select a row of particles to be measured. (d) Scattering spectra of a single nanorod for different polarization angles.

lected with the objective and sent to an spectrometer (Shamrock 500i-Andor) in the Czerny-Turner configuration. The spectrometer has a very sensitive EMCCD-camera (Ixon3-Andor) and a motorized torrete that allows choosing between two different diffraction gratings (150 and 1200 lines/mm) and a mirror. If the mirror is chosen, the system is used for imaging. The sample, the entrance slit and the sensor of the camera are in conjugated planes of the optical system. The entrance slit is motorized and can be closed to select a region of the sample for the spectroscopic measurement. This is illustrated in figure 4.3c. A polarization control module can be included in the optical path, when polarization-resolved measurements are intended. It consists on three optical elements: an uncoated Glan-Thompson polarizer in a rotating mount, a $\frac{\lambda}{2}$ achromatic waveplate and a

fixed polarizer. The first polarizer is employed to select the polarization component of the light be measured and filter out the other component. The purpose of the waveplate and the fixed polarizer is to eliminate artefacts in the measurement. Diffraction gratings usually have polarization-dependant reflection spectra. The waveplate is used to rotate the polarization of light in such a way that the incident polarization on the grating is always parallel to its grooves. This condition is guaranteed by the last polarizer. It is important to note that notch filters (see figure 4.1) are removed from the optical path before measuring spectra. Figure 4.3.c shows an example of polarization-resolved scattering spectra of a single Au nanorod, with a nominal size of 70x20nm.

Alternatively, the spectrometer can be used to measure inelastic scattering spectra, such as Raman or fluorescence. To that end, narrow band lasers are used for illumination instead of the white light lamp and suitable notch filters are used to avoid reflections of the excitation laser from reaching the detectors.

4.2 Computer Automation

A custom software was developed in Labview for integrating the control of instruments of the microscope through a common graphical user interface. A multifunction data acquisition device DAQ (National Instrument PCIe-6353) is used for acquiring, sending and synchronizing the signals of different instruments. It is connected to the computer through a PCI-express port and controlled by the Labview software. The control of the colour Canon camera and the Shamrock spectrometer was performed independently using software provided by their manufacturers, called EOS Digital SDK and Andor Solis, respectively.

The main window of the graphical interface is shown in figure 4.4. In the following, its different functionalities are described.

Nanopositioning

The front-screen of the nanopositioning module is shown in figure 4.4b. It has buttons that allow setting and reading the position of the piozelectric stage. The stage has a control driver (PI E-517) that communicates digitally with the computer through an USB cable. Motion control is achieved with nanometric resolution and the range of 200 μmon each (X, Y, and Z) axis. Also, it is possible to read the current position of the stage though capacitive sensors. The

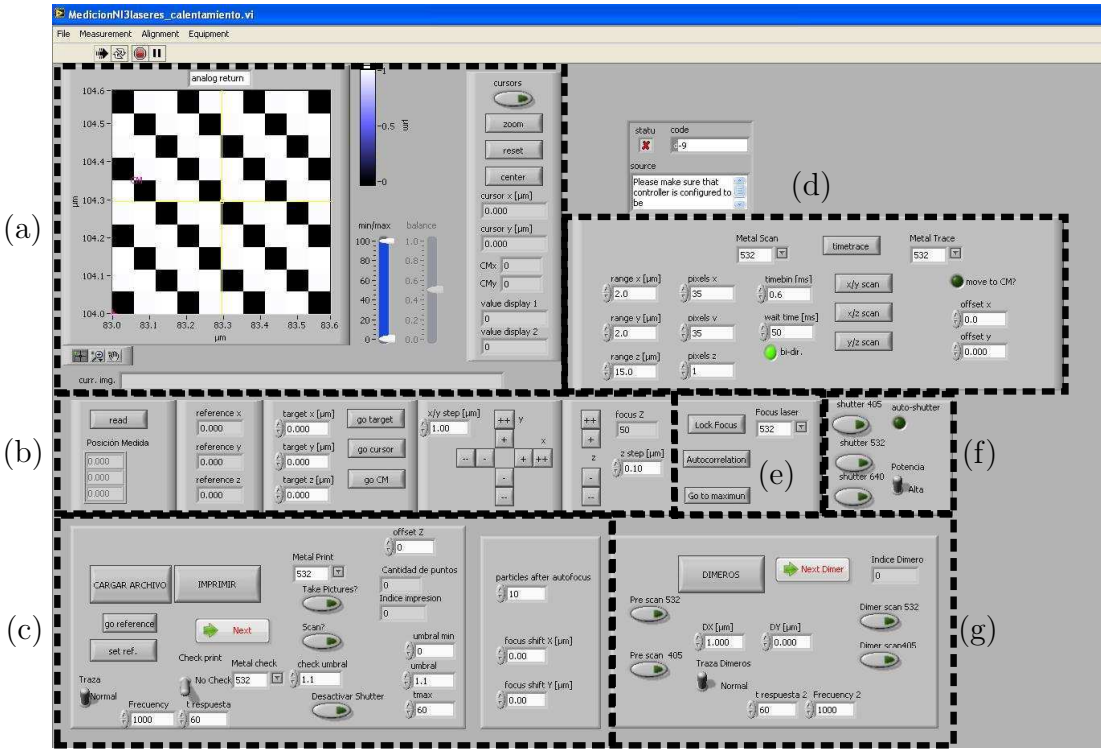

Figure 4.4: Graphical interface of the control program. (a) Image Navigation (b) Nanopositioning (c) Printing Routine (d) 2D scanning and Timetrace (e) Focus Lock (f) Laser Shutters and filters (g) Dimers Routine

manufacturer provides a library of Labview programs to control the stage.

Laser Shutters and Filters

The front-screen of the illumination control is shown in Figure 4.4f. It has buttons to control the shutters and motorized flippers. Each laser has a shutter, that is driven through TTL signals sent by the DAQ and controlled by the program. Also, neutral density filters mounted on a motorized flipper are included in the path of the beam. This enables switching the intensity of the laser beams between two levels, which is useful to rapidly change between printing and scanning applications.

Timetrace

Timetrace routine is called by the buttons from the main graphical interface shown in figure 4.4d. In order to initialize it, a laser has to be chosen. After that, an independent control graphical interface is opened, as shown in figure

4.5. The program opens the shutter of the chosen laser and measures the signal on the corresponding photodiode as a function of time (see figures4.1 and 4.2a). The detected signal is proportional to the light reflected and scattered by the sample, as described by equation 4.1, and is shown online. The program has three stopping options: It can be set to run for a pre-determined period of time, it can be set to run continuously until manually stopped by pressing a button, or it can be programmed to stop according to a given condition obtained from the live analysis of the signal (i.e. change in slope, incrementation above certain threshold, etc.). These routines works smoothly for acquisition rates up to 1 kHz. Faster acquisitions are possible without live visualization on screen or the possibility of automated stopping. Due to the slow communication speed between the computer and the DAQ, the response time for automated stopping is about 10ms.

After the acquisition stops, a file with the measured data is created. Relevant additional information such as the acquisition frequency or the date are also included in the file.

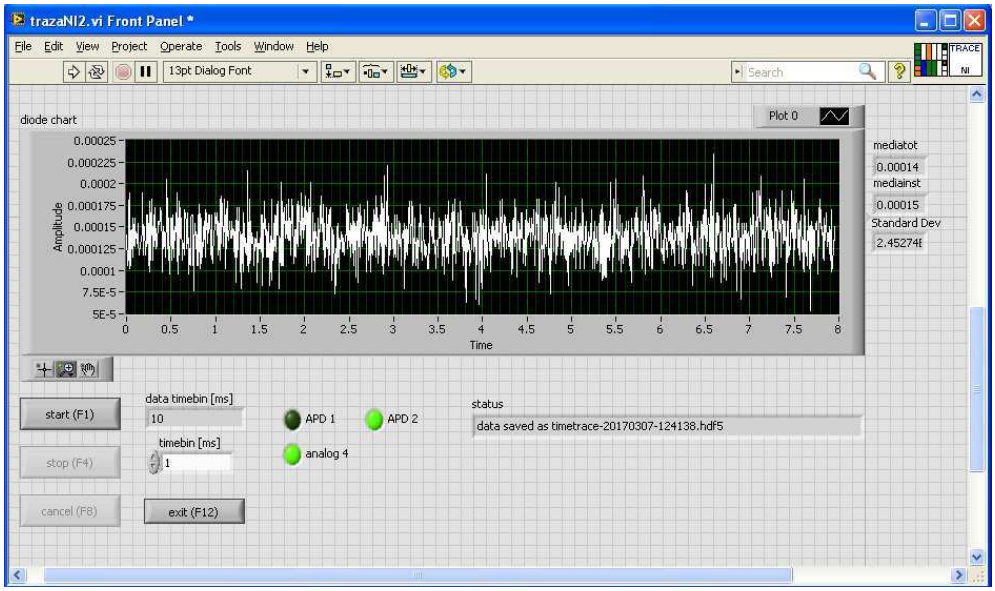

Figure 4.5: Graphical interface of the Timetrace program.

1D Scanning

This program measures the signal in the photodiode as a function of the position, while the stage performs a one dimensional back and forth movement in one of

its three axes (x,y or z). A laser beam, an axis, the number of pixels, the range of motion and a timebin has to be specified. According to these parameters, a file with the coordinates of the movement is created and loaded in the driver of the PI. To ensure linear motion between two positions x_{start} and x_{end}, the range of movement is extended (x_{min} and x_{max}) and acceleration ramps with no acquisition are included in the extended region. The stage has capacitive sensors that measure its current position. Using that information the stage driver has the capability to send trigger signals when the stage crosses a chosen position. Those signals are received by the DAQ, that only acquires data from the photodiode if the stage is inside the range between x_{start} and x_{end}.

2D and 3D Scanning

The scanning program user interface is shown in 4.6. It can be used independently or called from a panel on the main interface as shown in Figure 4.4d. It is based on the 1D scanning program. One dimensional back and forth acquisition is repeated in one axis, while shifting the position of a second axis between consecutive lines. Two-dimensional images can be acquired, in any combination of axis (xy, xz or yz), It also allows the acquisition of a stack of 2D images, for example several xy scans at different z positions. Figure 4.6 shows the confocal measurement of a single MNP. Left image correspond to data acquired when the stage is moving forward, ant right image correspond to the return.

This program also allows the on-line computing of the centre of mass of the image (as shown in the left-bottom panel). After the acquisition stops, a file with the measured data and additional relevant information is created.

Image Navigation

In the viewer of Figure 4.4a, the last performed 2D scan is shown. The centre of the image marks the centre of the objective. It has cursors to choose a position on the image. A routine permits to move the stage in order to centre the beam at the selected position. In addition, another routine allows the computation of the centre of mass of the image, and subsequent centring of the beam with that point. This can be used, per example, to centre a NP with a laser beam.

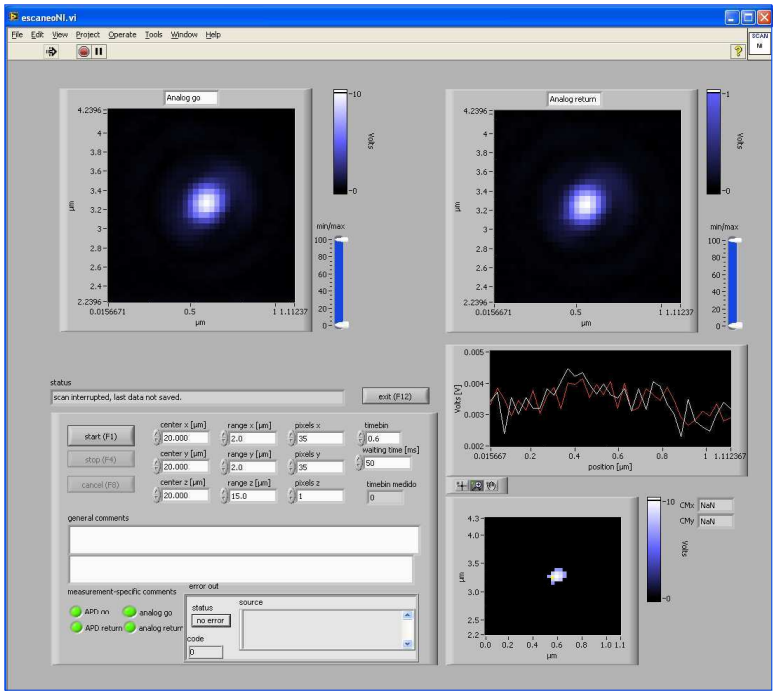

Figure 4.6: Graphical interface of the 2D scanning program.

Focus Lock

This program uses the 1D scan in the z axis. It can be called to save a z position or to return to a previously saved position, using the buttons shown in Figure 4.4e. In order to save a certain position, a one dimensional z-scan centred is performed, with 8 μm range. The resulting intensity profile is saved in a file. To return to the saved position in a later moment, another z-scan is measured and the result is compared with the saved profile through an autocorrelation algorithm. That algorithm provides the z displacement that has to be implemented in order to maximize the correlation between both z-scans. Another possibility is to use this program to measure a one dimensional z-scan intensity profile and then move to the position of maximum intensity.

Routines for optical printing individual nanoparticles and dimers

The Printing Routines combines several of the above described programs in order to achieve versatile and automated optical printing and characterization of individual NPs and dimers of two NPs .

Optical printing of individual NPs is controlled by the buttons in Figure 4.4.c. First, a file with a 3xN matrix including the three coordinates (x,y,z) of the N

particles to be printed is loaded. Second, the focus lock program is used to save the z position. Then, the program moves the stage to the target positions, automatically prints particles and includes focus correction or confocal scans when required. During the focusing and the scanning steps, the intensity of the beam is kept low using the computer-controlled neutral density filter, to avoid the printing of particles. All shutters are closed between steps. The wavelength of the beams employed for printing, focusing or scanning can be independently chosen. Using these routines it was possible to fabricate patterns of Ag and Au NPs as shown in figure 4.7.

Dimers routines are intended to be used after a Printing Routine. They are controlled by the buttons in Figure 4.4.g. Each particle on a printed array is located using the same file of coordinates, and a second particle is printed close to it, at a fixed distance (Δx,Δy). This routines includes confocal scans to find the centre of a printed particle, compensation of any focus drift and additional confocal scans to characterize the fabricated dimers.

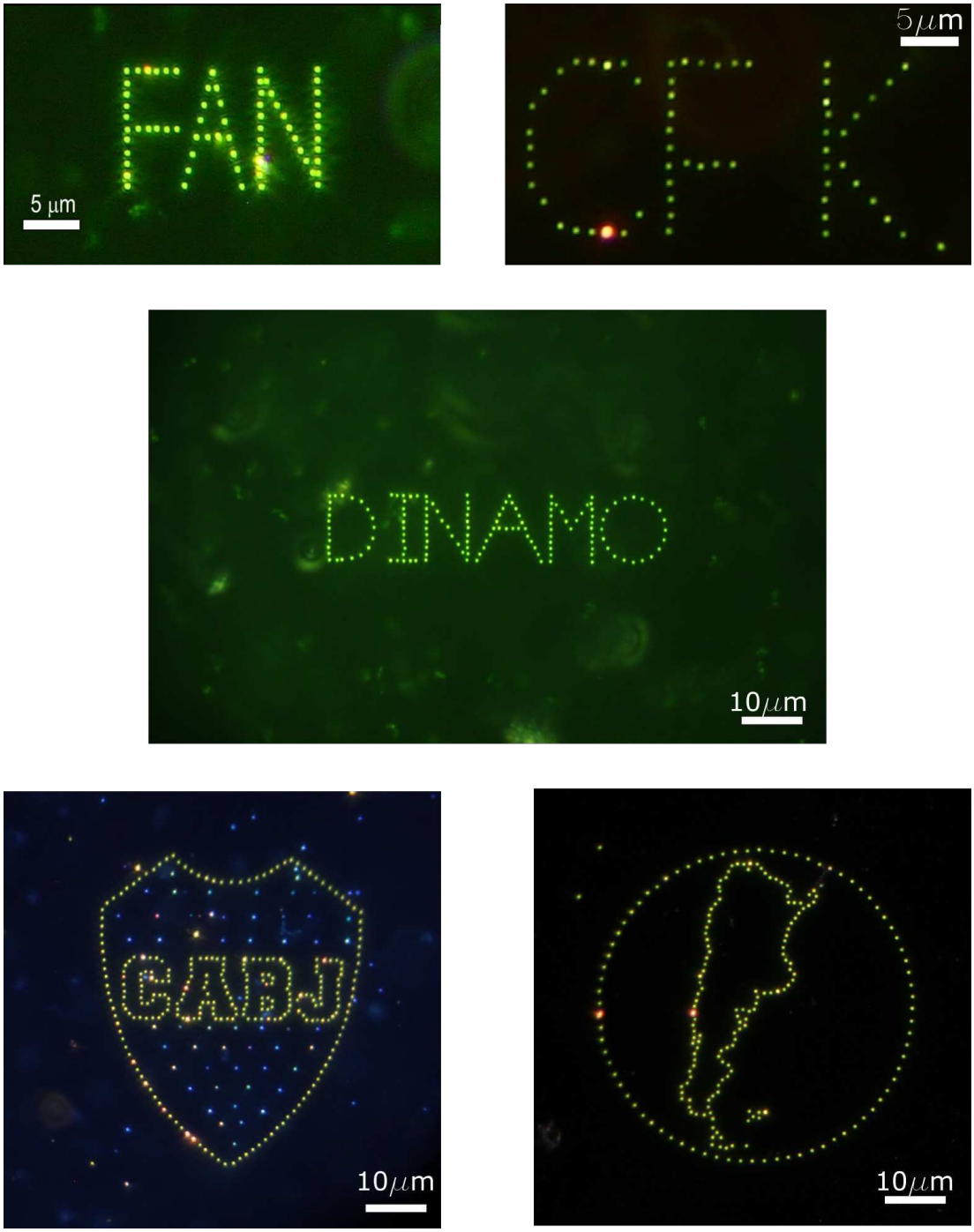

Figure 4.7: Patterns of Au and Ag NPs fabricated by optical printing on glass substrates.

5

Optical printing accuracy of isolated Ag and Au nanoparticles

The strength and direction of the optical forces depend on many parameters: the particle size, shape and material and the shape and wavelength of the optical field. To illustrate this, figure 5.1a shows, as a function of wavelength, the maximal axial and radial forces exerted on Ag and Au nanoparticles (NPs) of the same diameter (60 nm), placed at the centre of a diffraction limited focus (NA = 1.0). As can be seen, the magnitude of optical forces is many times stronger for wavelengths close to the plasmon resonance of the particle. Also, the ratio between radial an axial forces dramatically changes with the wavelength. On resonance, axial forces dominate, being approximately ten-fold stronger than radial forces. On the contrary, out of the plasmon resonance towards the red region, both axial and radial forces have similar magnitudes. Figures 5.1b-e show representative force maps for Ag and Au at laser wavelengths on and off resonance.

Optical printing of gold and silver NPs was proven to be possible using a printing wavelength either at plasmon resonance[56] or off-resonance[60, 64], but no detailed study comparing the precision in each case has been reported. Based on the first measurement by Urban et.al.[48] (described in section 3), it has been accepted as a 'rule of thumb' that the printing accuracy of a single particle was around 50 nm. However, there are still many open questions: Is that accuracy the best achievable? If so, which is the limiting phenomenon? Is there any influence of the wavelength or power of the printing beam? What is the best definition of precision? The aim of this chapter is to provide a deeper understanding of the subject including a detailed physical description of the printing process. The

employed substrates and particles are described in section 5.1. Section 5.2 defines the method to quantify the precision. Then, accuracy limits are tested for Au and Ag NPs on-resonance (section 5.3) and off-resonance (section 5.4). Finally, (in section5.5) a theoretical framework and simulations are used to rationalize the experimental results.

5.1 Sample preparation

In all the experiments presented in this chapter, Au and Ag NPs were printed on glass substrates. Both NPs were citrate coated, and negatively charged at neutral pH. In order to avoid spontaneous binding of the metallic nanoparticles (MNPs), the substrates were surface functionalized with negative charges employing a layer-by-layer deposition of polyelectrolytes[51, 68, 69], with Polydiallyldimethylammonium chloride (PDDA) $M_w = 400000 - 500000$ as polycation and sodium polystyrene sulfonate (PSS) as polyanion $M_w = 70000$ (both from Sigma-Aldrich). First, glass coverslips were cleaned through the folowing steps:

1. Sonication for 10 minutes in Hellmanex (2% v/v)
2. Thorough rinse with MilliQ water.
3. Acetone rinse.
4. Dry in a laboratory oven at $80°C$.
5. Plasma cleaning for 3 minutes.

Then, substrate was surface modified by:

1. Immersion in PDDA solution (1 mg/ml in 0.5M NaCl).
2. Rinsing with MilliQ water.
3. Immersion in PSS solution (1mg/ml in 0.5M NaCl).
4. Rinsing and stored in MilliQ

Citrate-capped gold NPs were purchased from Nanopartz (specified diameter 62 ± 2nm; average diameter determined by FE-SEM 63 nm $\pm$ 3 nm). Citrate-capped silver NPs (specified diameter 60nm $\pm$ 8nm; average diameter determined

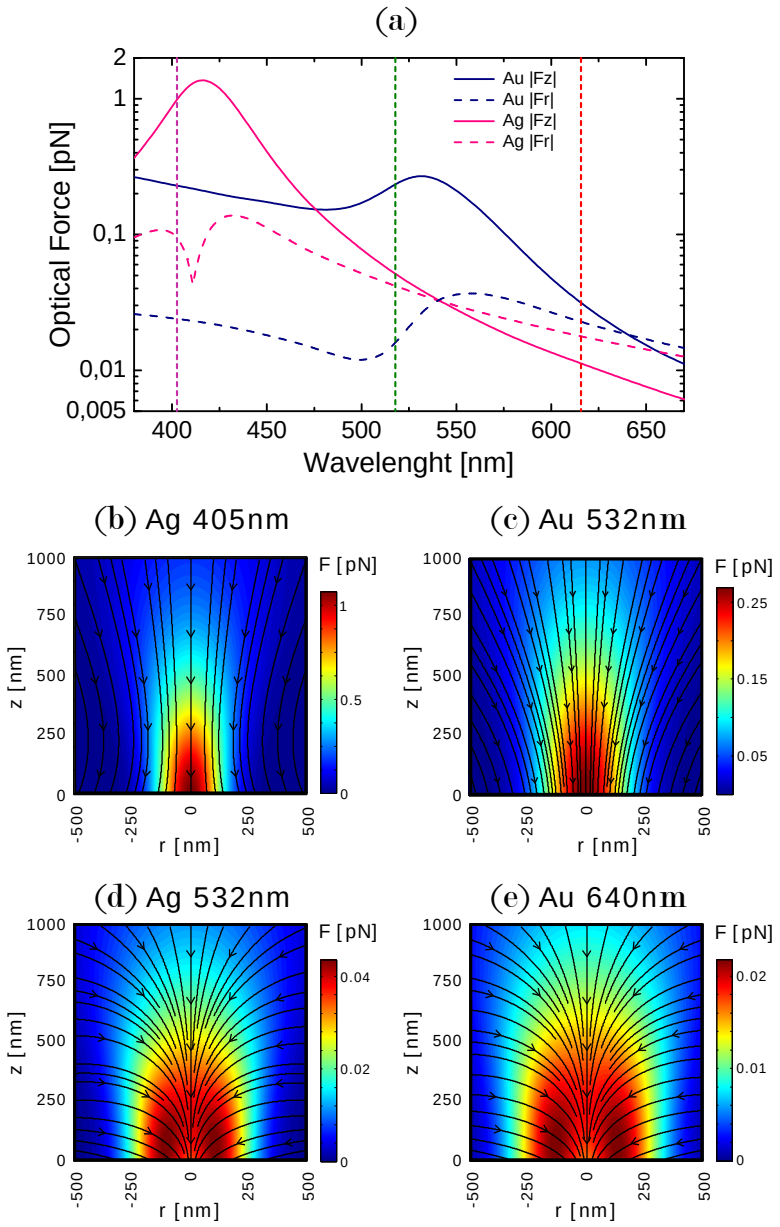

Figure 5.1: (a) Absolute value of the maximum axial and radial force vs wavelength for 60 nm Ag and Au NPs placed at the centre of a diffraction limited Gaussian focus with NA = 1.0, and a of $P = 1$ mW. The three vertical dashed lines correspond to the printing wavelength used in the experiments, 405 nm, 532 nm and 640 nm. (b-e) Force maps at $P = 1$ mW for 60 nm particles. The arrows denote the direction of the force and its magnitude is colour coded. All forces were calculated using equations 1.30 and 1.31.

by FE-SEM 57nm±5nm) were purchased from Sigma-Aldrich. For simplicity, and because the small difference in size is practically irrelevant for these experiments, 60 nm is used along this chapter as nominal size for both NPs. Original colloids

are diluted to a concentration of $C \approx 2.10^9 \frac{particles}{ml}$ using a solution of 1,5 mM NaCl.

5.2 Determination of printing time and printing accuracy

The process of optical printing includes Brownian motion and is therefore stochastic. Consequently, in order to characterize the precision and the average printing time it is necessary to perform the experiment a large number of times with individual NPs to obtain the representative statistics. To that end, the following procedure was performed. First, the stage was moved to the target position (x_0, y_0) for the optical printing of a NP. The laser beam was unblocked and a the time-trace of the confocal scattering signal was monitored and analysed on-line in order to detect the when a NP was printed, as shown in figure 5.2e. Printing events were detected as a step in the scattering signal. The "waiting time" is defined as the time interval between the moment the beam was unblocked and the moment when a printing event was detected. This waiting time for optical printing varies stochastically from one attempt to the other, and a characteristic distribution is shown in 5.2f. As can be seen, is a non-symmetrical fat-tailed distribution, i.e. there are events with much longer times than the average, unlike in a Gaussian distribution. Upon the detection of a printing event, the beam is immediately blocked. Right after that, a confocal scattering image is acquired, using a lower laser intensity in order to prevent further printing events during scanning. The centre of the image is the target position (x_0, y_0). The centre of mass of the image was computed and assigned to the position of the printed particle (x, y). The difference $(\delta x, \delta y) = (x_0, y_0) - (x, y)$ is the printing error. Using this approach, errors due to mechanical drift of the microscope are negligible, because acquiring an image takes less than ten seconds and the microscope drift is about 5nm/min.

As discussed in section 4.1, the detection of MNPs is interferometric. Depending on the scanning wavelength, the particles can appear as bright or dark spots in the images. For localization purposes, the scanning wavelength was always $\lambda = 405$ nm for Ag NPs and $\lambda = 532$ nm for Au NPs, independently from the wavelength used for printing it. In this way, the NPs are detected as bright spots in all cases.

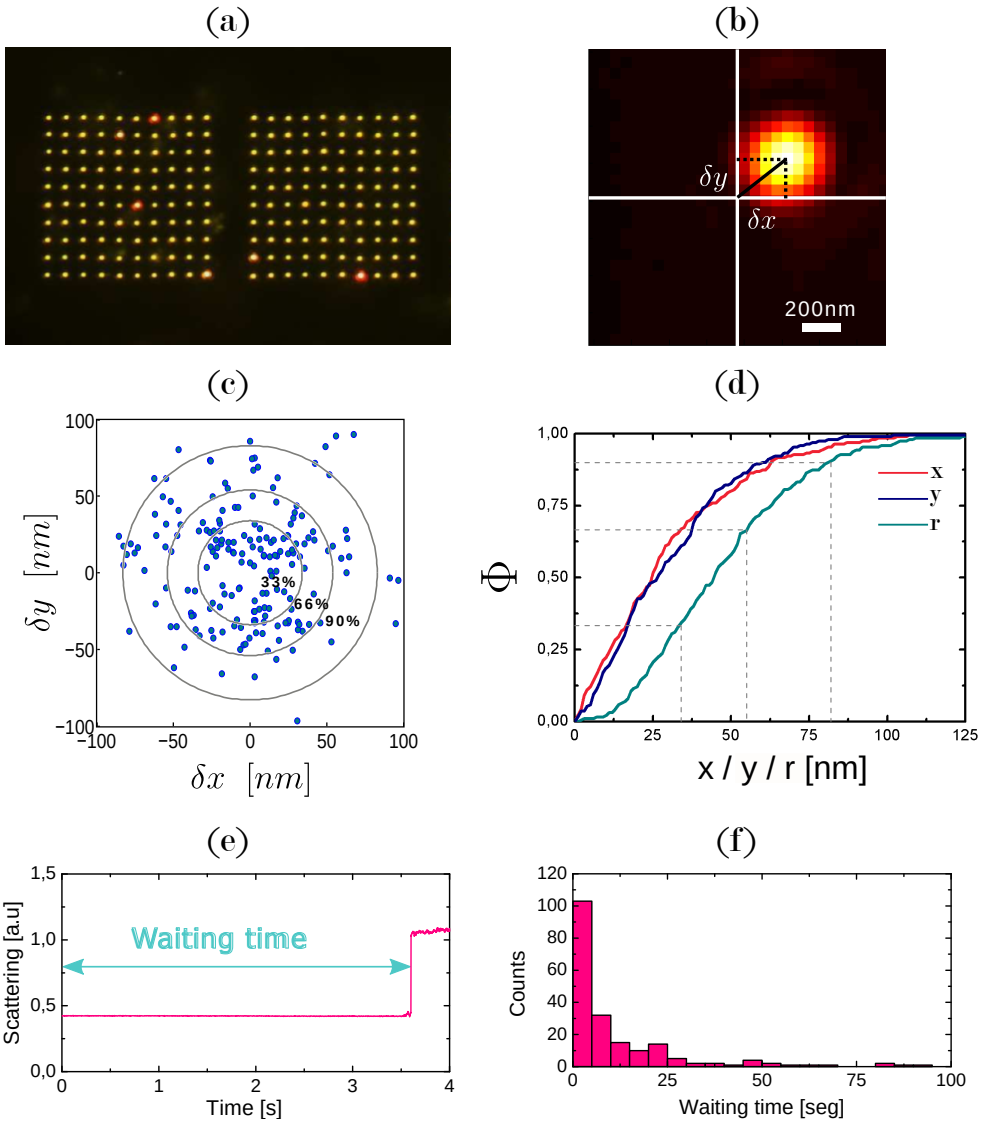

Figure 5.2: (a) Dark field image of two square array of optically printed 60 nm Au NPs (b) Example of a ccattering confocal scan used to determinate the printing error. (c) Scatter 2D plot where the coordinates of each dot is the printing error of a particle. (d) Unidimensional (x and y) and radial (r) cumulative distribution functions Φ (e) Timetrace: Elastic scattering signal during optical printing of a NP. The step in the signal correspond to a printing event. (f) Histogram of waiting times. The median is $t_m = 4.7\ s$

Figure 5.2a show a dark field image of an example with 200 NPs printed in two square grids for accuracy determination. There are some reddish NPs which correspond to non-sphperical or larger particles. After each particle was printed, the error $(\delta x, \delta y)$ was computed, using a confocal scan as shown in figure 5.2b. Particles that were evidently different in the dark field image were removed from

the analysis. An example result of such a measurement is shown in figure 5.2c, where the coordinates of all printing errors are included in a 2D scatter plot. The grey circles represent the areas containing the 33%, 66% and 90% of the particles. The radius containing the 90% is called R_{90}. An alternative way of visualizing the same information is through the cumulative distribution function Φ, as shown in figure 5.2d. This function, represents the probability that a random particle will be printed within a range from the target coordinate. As an example, figure 5.2d shows the unidimensional cumulative distributions functions along the x and y directions ($\phi(x)$ and $\phi(y)$), obtained from the analysis of the optical printing of 200 NPs. Both function are similar indicating that the printing error is fairly isotropic. Furthermore, since NPs were printed with linearly polarized light along the x axis, printing error is independent of the polarization of the beam.

The standard deviations, calculated using $S_x = \sqrt{\frac{1}{N}\sum_{i=1}^{N}(x_i - \overline{x})^2}$ with $\overline{x}$ the mean value and N the number of particles, are $S_x = 38.8$ nm and $S_y = 37.6$ nm.

In the following sections the precision is characterized using the cumulative distribution function (CDF) for the modulus of the error $\delta r = \sqrt{\delta x^2 + \delta y^2}$, as shown in figure 5.2.d in the light blue curve. The Root mean square error (RMSE) is defined as

$$e_{RMS} = \sqrt{\frac{1}{N}\sum_{i=1}^{N}(x_i - \overline{x})^2 + (y_i - \overline{y})^2} \tag{5.1}$$

In the present example, $e_{RMS} = 53.9$nm.

5.3 On-resonance Optical Printing

The influence of laser power on the accuracy of optical printing near plasmon resonance was investigated for Au and Ag 60nm NPs . For this purpose, the procedure described in 5.2 was carried out for a range of laser power levels, using wavelengths of 405 nm for Ag and 532 nm for Au with a beam waist w_0 of (226 ± 7) nm and (265 ± 5) nm respectively. Example grids are shown in figure 5.3a and 5.3b. The results were similar for both materials. At lower powers, printing events become rare; the optical forces are too weak to overcome the electrostatic repulsion. A maximum waiting time of two minutes before moving to the next position was set, and that is the reason why there are holes in the grids at the lowest powers. If the laser power is decreased below a certain threshold, no particle is printed. The threshold power P_{th} was defined as the minimum power

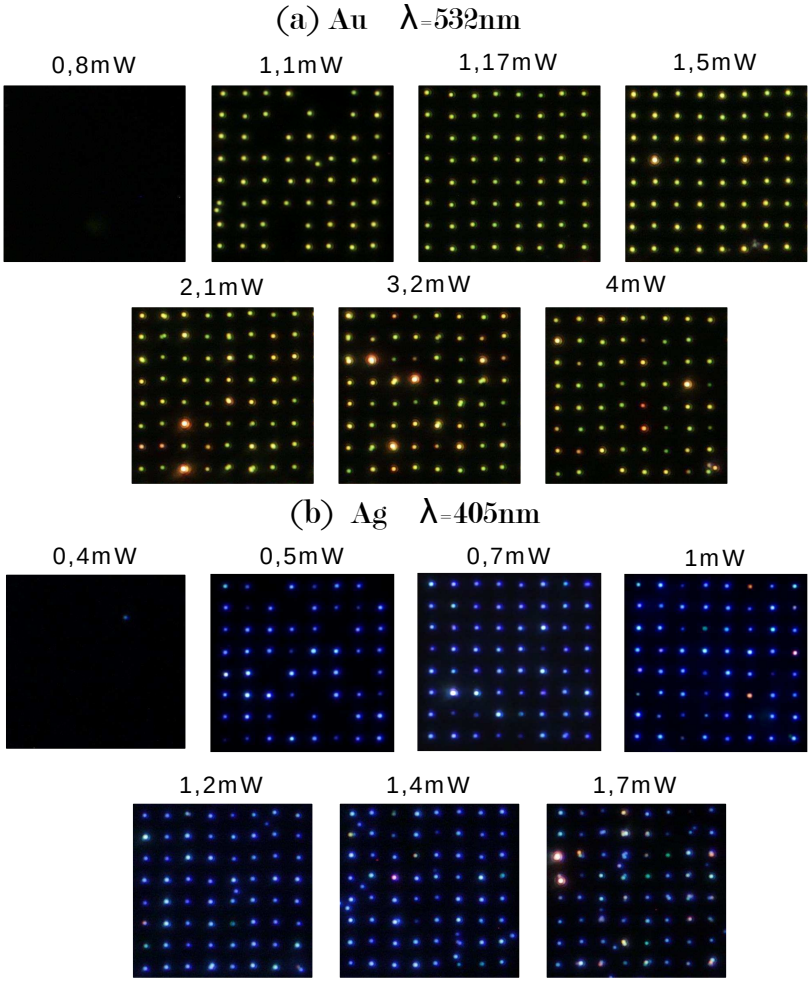

Figure 5.3: On-resonance printing: Example arrays of (a) Au and (b) Ag 60nm NPs fabricated through on-resonance optical printing at different laser powers.

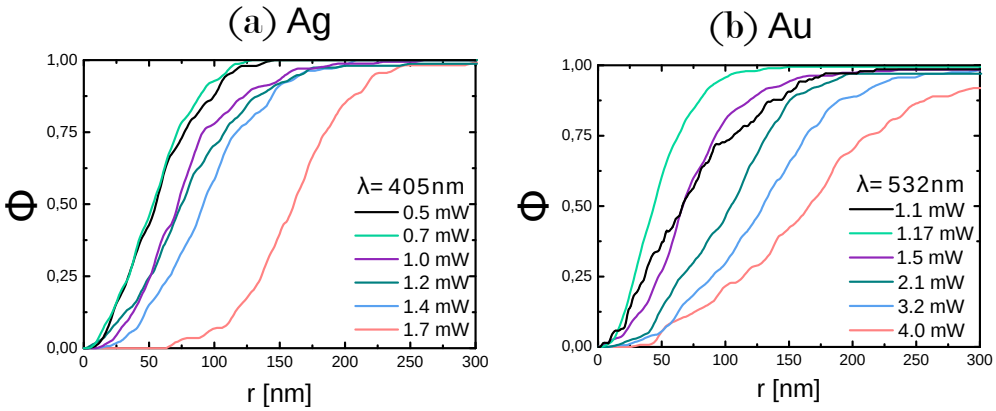

Figure 5.4: On-resonance printing: (a) Radial CDF for Ag NPs at different powers. (b) Radial CDF for Au NPs at different powers.

for which there is at least one printing event in ten minutes. It was found to be $P_{th} = (0.55 \pm 0.05)$ mW for Ag and $P_{th} = (1 \pm 0.05)$ mW for Au.

On the other hand, at high powers the number of *defective* NPs increases. Those are the particles appearing with different colours in the dark-field images of the example grids. This could be caused by the lost of selectivity as the optical forces became strong enough to print other types of NPs from the suspension. Other possibility is that the particles can be reshaped or modified by the high temperatures and electric fields reached[70] (further discussion on controlled reshaping is presented in chapter 7). The power was increased until the defective NPs outnumbered the regular NPs .

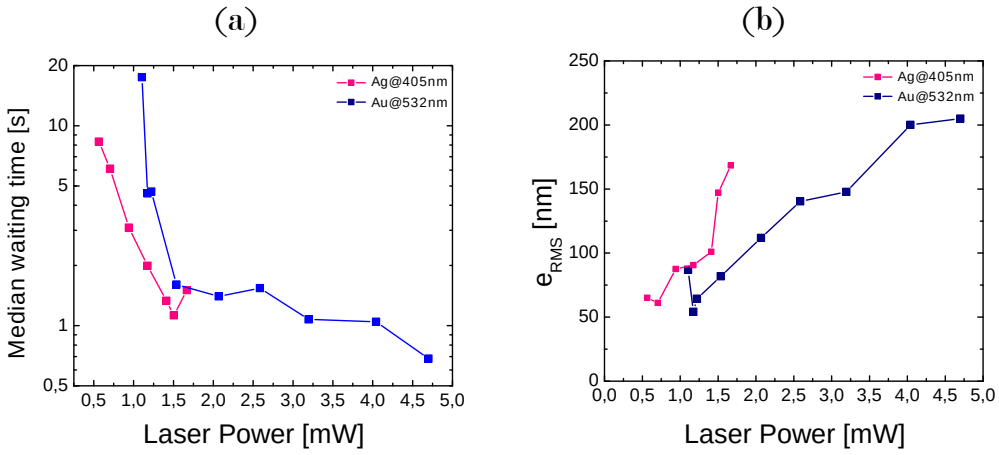

Figure 5.5: (a) On-resonance waiting time (log scale) as function of laser power. (b) e_{RMSE} as a function of laser power for both materials. Pink: Ag at $\lambda = 405$ nm. Blue: Au at $\lambda = 532$ nm.

Figures 5.4a and 5.4b show the Φ for six different laser powers. Clearly, the precision of optical printing gets worse as the laser power increases, for both NPs when the light used is tuned to their respective localized surface plasmon resonance (LSPR). Figure 5.5b summarizes this observation displaying the e_{RMSE} as a function of the power for both materials. The precision improve as the laser powers is decreased, reaching values of around 50 nm, well below the beam waist size. However, a slightly larger error e_{RMSE} is found for the laser power closes to the minimum threshold.

It is also interesting to investigate whether the waiting times for printing depend on laser power. 5.5a shows the median waiting times for the printing of Ag and Au NPs as a function of laser power. In both cases the waiting time increases as the laser power reduces, and they become drastically longer as the

threshold approaches.

5.4 Off-resonance Optical Printing

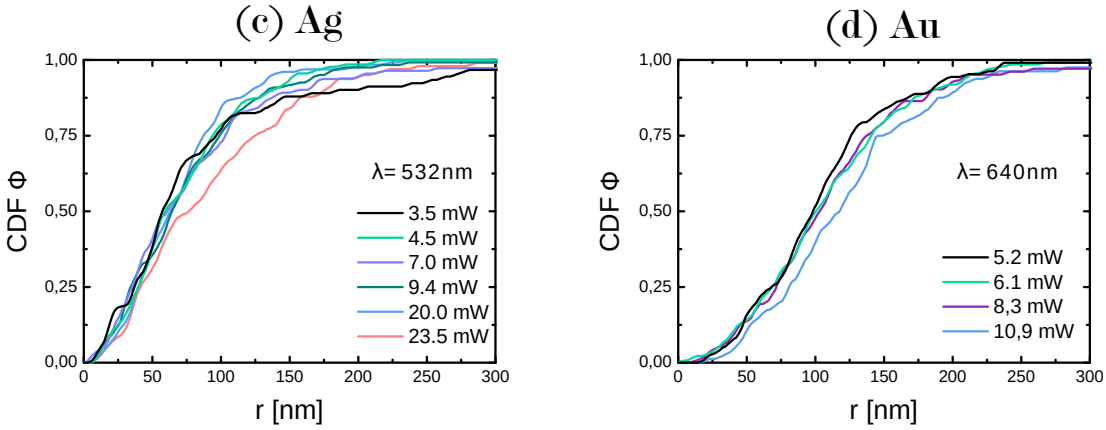

Figure 5.6: Off-resonance printing: (a) Radial CDF for Ag NPs at $\lambda = 532$ nm and different powers. (c) Radial CDF for Au NPs at $\lambda = 640$ nm and different powers.

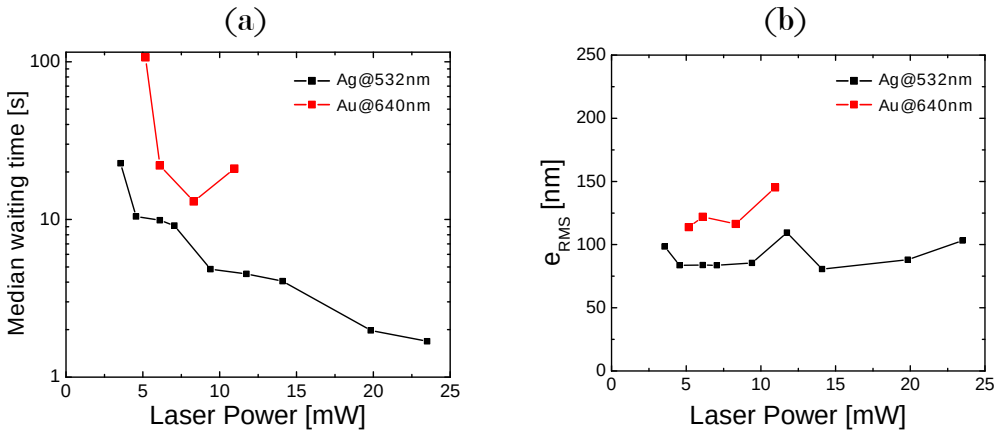

Figure 5.7: (a) Off-resonance waiting time (log scale) as function of laser power. Black:Ag at $\lambda = 405$ nm. Red: Au at $\lambda = 532$ nm.

In order to print NPs out of resonance, lasers of 532 nm for Ag and 640nm for Au were used, with a beam waist w_0 of $(265 \pm 5)nm$ and $(319 \pm 6)nm$ respectively. As expected from the smaller absorption and scattering cross sections involved, higher laser powers are required for optical printing. The threshold powers were $P_{th} = 3.5$ mW for Ag and $P_{th} = (5 \pm 0.5)$ mW for Au.

On resonance, the automatic detection of printing events is done with the printing beam itself. This can be difficult when working off-resonance, due to destructive interference that occurs at the detector (discussed in section4.1). For this reason, a detection laser was superimposed to the printing beam, resonant with plasmon of the particle. The intensity of the detection laser was kept as low as possible, and in all cases the force exerted by this beam was below 10% of the force exerted by the printing beam. An additional difficulty for automated detection is that, due to the high radial to axial force ratio present when using off-resonance light, particles can be trapped in the confocal volume and raise the detection signal, but without being printed on the surface. For this reason an additional confirmation step was included. After a NP was detected, both the printing and the detection beams were blocked for a time interval of one second. Then, the presence of the NP was interrogated with the detection beam alone, in order to check whether the particle was fixed on the surface. If the NP was not fixed, the printing beam was unblocked and the process was repeated until a NP was effectively printed. Once the printing was confirmed, the position of the printed NP and the printing error were determined.

Figure 5.6 shows the $\Phi(r)$ obtained from the off-resonance printing of 200 NPs at different laser powers. Remarkably, the precision of optical printing off-resonance is practically independent of the laser power used. Although the precision in this case is a little worse than the best precision attained in resonance, it remains well below the diffraction limit. The value of e_{rms} in each case is roughly 2.75 times smaller than the beam waist, namely 90 nm for Ag and 115 nm for Au NPs (Figure 5.7).

The waiting times are shown in figure 5.7a. They are in general larger than ones observed on resonance, but follow the same decreasing tendency with increasing power.

5.5 Discussion of the Optical Printing mechanism

In this section a physical description of the process of optical printing of NPs is provided, aiming to explain the experimental observations described in the previous sections. First, the measured waiting times are discussed in subsection 5.5.1. Then, the printing precision is addressed in subsection 5.5.2. Part of

the results presented here emerged from fruitful discussions with Lukáš Chvátal and Pavel Zemánek from the Group of Optical Micro-manipulation Techniques (OMITEC) at the Institute of Scientific Instruments of the Czech Academy of Sciences (Brno, Czech Republic). Subsection 5.5.1 include calculations performed by Lukas Chvatal, as indicated.

5.5.1 Waiting time for optical printing

During the optical printing process, the NPs may experience two kinds of motion: i) Deterministic motion driven by the external optical field or ii) Diffusive or Brownian motion. Below, the two types of motion are described and their contribution to the observed waiting times is discussed.

Deterministic motion: Fluid flows can be classified according to the Reynolds number[71]

$$Re = \frac{\rho \tilde{V} \tilde{L}}{\mu} \tag{5.2}$$

where $\tilde{V}$ is a characteristic velocity, $\tilde{L}$ a characteristic length, μ the dynamic viscosity and ρ the fluid density. The Reynolds number estimates the ratio between inertial and viscous forces. If $Re \ll 1$, viscous forces dominate. In the present system, using $\tilde{L} = 60$nm for the sphere diameter, $\mu = 10^{-3}$Pa s and $\rho = 10^{-3}\frac{kg}{m^3}$ for the water viscosity and density, respectively, one obtains a value of $Re \approx \tilde{V} 6.10^{-2}\frac{\mathrm{s}}{\mathrm{m}}$ which is $\ll 1$ for any physically meaningful velocity of the NPs during the optical printing process. The movement of a particle in a flow with such a small Reynolds number is *overdamped*. This means that the velocity of the particle is proportional to the applied force, according to Stokes equation

$$V(\vec{r}) = F(\vec{r})\,\gamma \tag{5.3}$$

with $\gamma = \frac{1}{6\pi\mu a}$ the Stokes mobility and a the particle radius. For the NPs moving in water driven by an external optical field $F_{op}(r)$ we can assign to each point a characteristic time for deterministic motion given by

$$\tilde{\tau_d}(\vec{r}) = \frac{\tilde{L}}{|V(\vec{r})|} = \frac{\tilde{L}}{\gamma |F_{op}(\vec{r})|} \tag{5.4}$$

Equation 5.3 states the proportionality between the force and the velocity. This means that the force field lines can be interpreted as velocity lines or trajectories. Given an initial position $\vec{r}$, the trajectory toward the surface is determined by the optical forces. This enables the calculation of a "time of flight" $\tau(\vec{r})$, given by the path integral on the trajectory from that position $\vec{r}$ to the substrate

$$\tau(\vec{r}) = \int_{\vec{r}}^{z=0} \frac{\mathrm{d}l}{\gamma |F_{op}(r)|} \tag{5.5}$$

Figure 5.8 shows the time of flight τ for Au particles near the Gaussian focus of a beam of $\lambda = 532$ nm, with a waist of $w_0 = 265$ nm a power of $P = 1$ mW, typical parameters of optical printing on resonance. Since the beam has axial symmetry, it is shown in polar coordinates. The motion of the Au NPs under

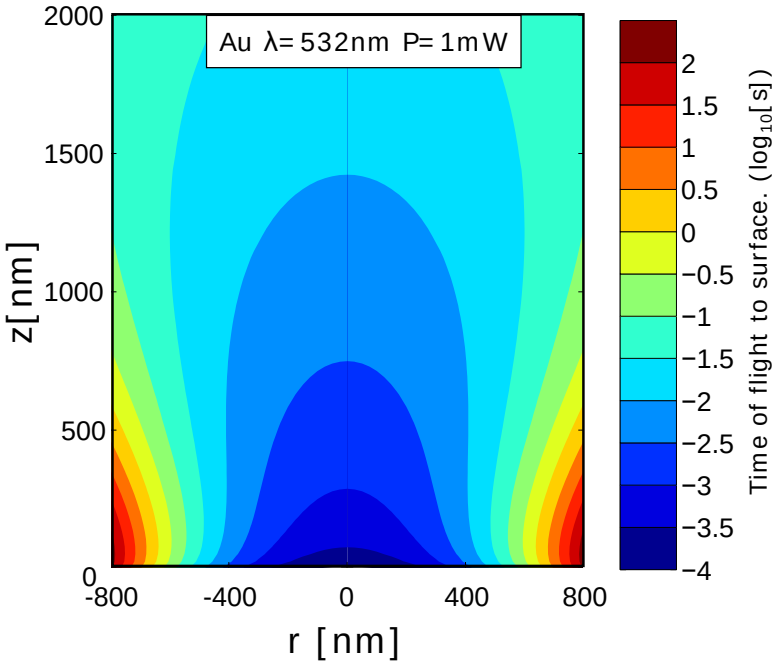

Figure 5.8: Time of flight for deterministic motion calculated using equation 5.5 for Au NPs with a laser beam of $\lambda = 532$ nm, a waist $w_0 = 265$ nm and power of $P = 1$ mW. Values on this figure were calculated by Lukas Chvatal from OMITEC.

these conditions is much faster than the observed waiting times. For example, a particle starting 2 μm away from the surface at the center of the beam has a time of fly of $\approx$ 10ms, while the observed waiting times are typically in the order of the seconds. Therefore, the optical printing process can not be explained only

in terms of deterministic motion and Brownian motion must be involved as well.

Free diffusive Brownian motion: The mean square displacement of a freely diffusing particle three dimensions in a time t is [72]

$$\overline{\Delta r^2} = 6Dt = 6\gamma k_B T t \tag{5.6}$$

With $D = \gamma k_B T$ the diffusion coefficient, $\gamma = \frac{1}{6\pi\mu a}$ the Stokes mobility, k_B the Boltzmann constant and T the temperature. Let denote $\tilde{\tau_f}$ the characteristic time for which a particle diffuses over some characteristic distance $\tilde{L}$.

$$\tilde{\tau_f} = \frac{\tilde{L}^2}{6k_B T\gamma} \tag{5.7}$$

Considering a NP with diameter of 60 nm, in water and at $25°C$, the time needed by the NP to diffuse over a length equal to its own radius is $\tilde{\tau_f} \approx 6.10^{-5}s$. If this time is much shorter than its deterministic counterpart, then the motion of the NP is dominated by free diffusion (pure Brownian motion). One way to analyse these kind of situations is by means of the adimensional Peclet number:

$$Pe\,(\vec{r}) = \frac{\tau_f}{\tau_d\,(\vec{r})} = \frac{\tilde{L}|F_{op}\,(\vec{r})\,|}{2k_B T} \tag{5.8}$$

If the Péclet number is much lower (higher) than unity, diffusion is dominant (negligible). It will be assumned that the characteristic time for Brownian motion $\tilde{\tau_f}$ is uniform in space; i.e. there is no influence of the surface or high temperature increases induced by the laser on the diffusion. The characteristic time for directed motion τ_d depends on position according to the optical force field. Using the Péclet number, a "capture volume" V_c can be defined, understood as the region of space where the optical forces are stronger than Brownian motion. This volume and its boundary surface S_c are defined as

$$\begin{aligned} V_c &= \{\vec{r} : P\,(\vec{r}) > 1\} \\ S_c &= \{\vec{r} : P\,(\vec{r}) = 1\} \end{aligned} \tag{5.9}$$

Figure 5.9 shows the surfaces S_c for Au NPs on-resonance and for Ag NPs off-resonance for different power levels. In both cases a Gaussian beam of $\lambda = 532$ nm with a waist of $w_0 = 265$ nm was used. The capture volume increases

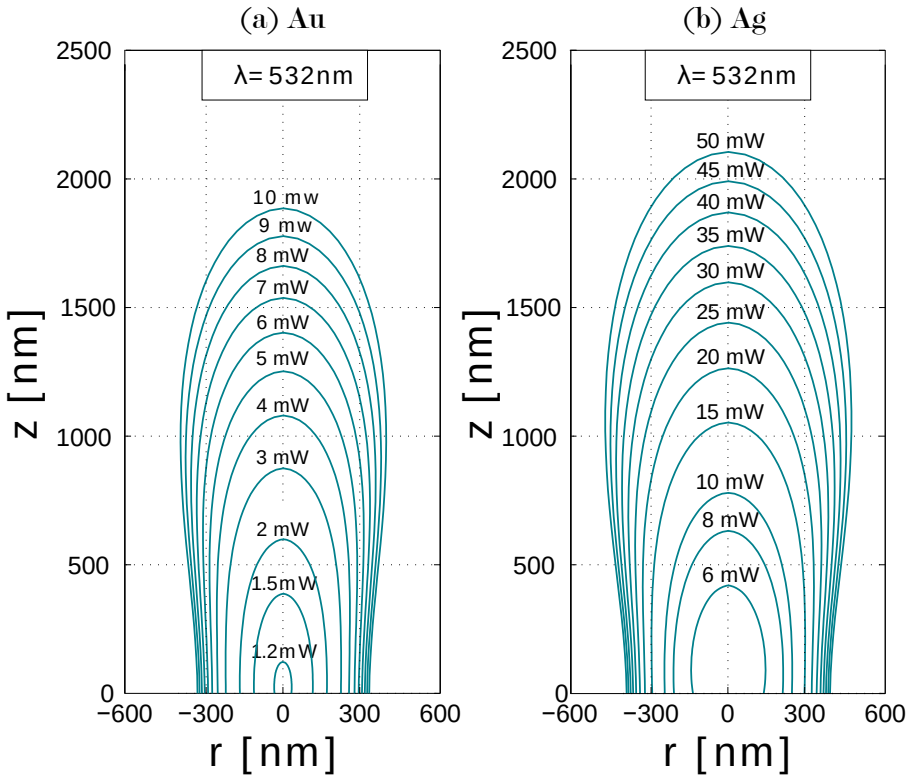

Figure 5.9: Capture surfaces S_c of $Pe = 1$ for different powers levels, calculated at $\lambda = 532$ nm for (a) on-resonance Au and (b) off-resonance Ag 60 nm spheres. This surfaces can be understood as the transition between Brownian and deterministic motion. A beam waist of $w_0 = 265$ nm was used. Values on this figure were calculated by Lukas Chvatal from OMITEC.

for higher powers. If a particle is inside this volume, it is driven towards the substrate by the optical force field. This motion is fast. For example, a Au NP illuminated at $\lambda = 532$ nm and $P = 1,5$ mW that enters the capture volume from the axial axis (r=0), will require $\simeq$ 1ms to reach the surface. This time is negligible compared to observed waiting times, that are typically of a few seconds. Therefore, it can be concluded that the main contribution to the waiting time is given by the Brownian motion of the particles outside the capture volume, i.e. the waiting times shown in figures 5.5a and 5.5b correspond to the time that the closest particle to V_c requires to reach S_c by diffusive motion. Since it depends on the initial position of the particle and its random motion, the waiting time is a stochastic variable with values varying from one event to an other. The fact that the capture volume increases with the power explains why the waiting time decreases. It is important to note that the particle concentration is $C \approx 2.10^9 \frac{NPs}{ml}$, which correspond to approximately 5.10^{-4} particles in the

capture volume $V_c(1.2\ mW)$ for Au in resonance. This means that when the printing beam is turned on, the most likely situation is the capture volume to be empty.

This conclusion is further supported by estimating the order of magnitude of diffusive times. The concentration of particles is $C \simeq 2.10^9 \frac{NPs}{ml}$ which means that, on average, there is a particle every $\simeq 500\ \mu\text{m}^3$. This value is typically much larger than the capture volumes. For example, the capture volume for Au NPs at $P = 1.5$ mW is $V_c(1.5\ mW) \simeq 0.05\ \mu\text{m}^3$. The average distance between a particle and the capture volume is can then be estimated by $\simeq 8\ \mu$m. The required time for a particle of 60 nm to diffuse over that distance is, according to equation 5.7, $\tau \simeq 1,4s$, which is of the same order of magnitude of the observed waiting times.

5.5.2 Printing error

The width of the capture volume is comparable to the beam waist w_0, i.e. a few hundreds of nanometers, as can be seen from figure 5.9. However, the observed printing error or mean square error of the printed NPs are smaller, and particles can be printed with a position accuracy of up to $\simeq$ 50nm. In order to explain this, it is important to recall that there is an electrostatic barrier close to the surface, as introduced in section 3.1. Therefore, the necessary condition for printing a particle in a position r on the surface, is that the axial optical force $F_{op}^z(r,z)$ fulfils the condition

$$|F_{op}^z|\,(r, z=0) > F_{th} \tag{5.10}$$

Where $F_{th} = max\,\{F_{DLVO}\}$ is the threshold force, defined as the maximum of the surface repulsion, given by DLVO theory. According to this theory, the range of action of the repulsion is limited to distances between the surface and the particle of just a few nanometers. Considering that this distances are short compared to the typical variation lengths of the optical fields, F_{op} in 5.10 was evaluated at the surface plane $z = 0$ with negligible error.

The existence of a threshold force is consistent with the experimental observation of a threshold laser power P_{th}, below which it is impossible to print a particle. In fact, the value of the electrostatic threshold force F_{th} can be estimated from

the experimentally observed P_{th} though

$$F_{th} = max\left[F_{op}^{z}\left(P_{th}\right)\right] \tag{5.11}$$

If a the laser power is above the threshold power, it is capable of generating optical forces stronger than the surface repulsion F_{th}. Hovewer, since optical forces decrease rapidly for increasing distance from their maxima, the region where they are stronger than the repulsion is limited. For each laser power, a "printing radius" $R_p\left(P\right)$ is defined, as the radius of the region in the focal plane where the axial optical force is above the threshold, i.e. the radius within the axial optical force fulfils condition 5.10. Figure 5.10 shows the axial optical force $F_{op}^{z}\left(r, z=0\right)$

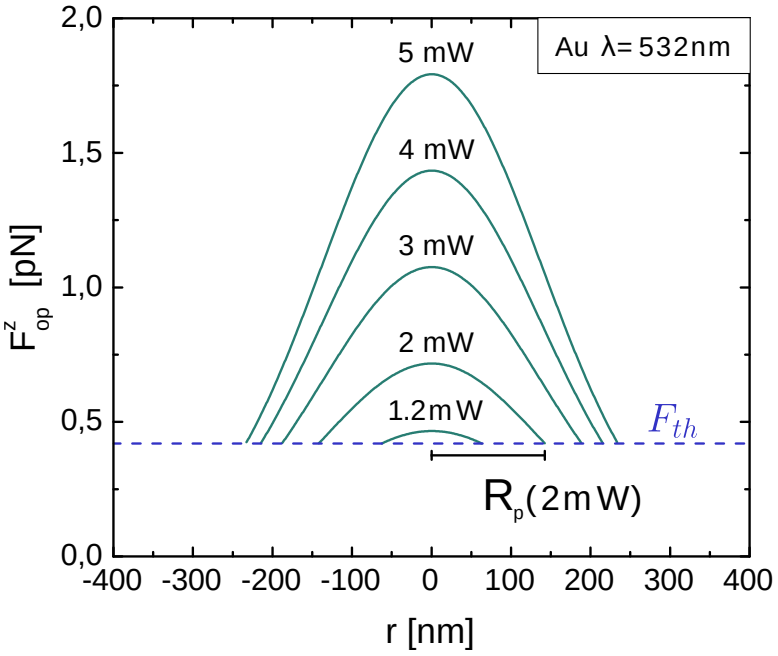

Figure 5.10: Axial optical force F_{op}^{z} at the substrate plane (z=0) as a function of the radial position, for Au NPs at $\lambda = 532$nm and different beam powers. The blue horizontal line indicates the threshold repulsive electostatic barrier F_{th}. The printing radius R_p is depicted at $P = 2mW$. The threshold force F_{th} was calculated using equations 5.11, 1.30 and 1.31 and the experimental value of P_{th}.

for different beam powers, only for the region within the printing radius $R_p\left(P\right)$, calculated for Au NPs at $\lambda = 532$ nm. The value for $R_p\left(P = 2\text{ mW}\right)$ is depicted. Figure 5.11 shows R_p (solid lines) as a function of the laser power, for 60 nm Au and Ag NPs at the wavelengths experimentally tested in previous sections. R_p increases steeply close to the threshold power and diminishes its growth rate as

the laser power increases..

It is interesting to compare the calculated printing radius R_p with the experimental observations of previous sections. For that, we included in figure 5.11 the observed R_{90} for each condition. This is, the radius containing the 90% of the localizations of printed particles, as defined in section 5.2. The general agreement between R_p and R_{90} for the on-resonance case is remarkable, specially considering that the calculations included no free parameter, which is a strong indication that the proposed physical picture is correct in essence. There is a systematic deviation at the highest laser powers, where the observed printing error R_{90} is larger than R_p. This can be due to the considerable temperature increase that the particles experience at those high powers, which can be as large as hundreds of degrees, distorting (reducing) the repulsion.

At this point, it becomes clear why is not possible to increase the optical printing precision simply by reducing the laser power.

In theory, one could set the laser power just above the threshold in order to set a small printing radius R_p and thus highly accurate printing. However, it must be noted that close to the threshold, the dependence of R_p with the printing power is extremely sharp. For example, $\frac{\mathrm{d}R_p}{\mathrm{d}P}(P_{th}) = 2\frac{\mathrm{nm}}{\mu W}$ for Au at $\lambda = 532$ nm, which means that a power sweep with at least 10 μm of resolution is needed to find such a power. Also, fluctuations of the power should be kept smaller than ≈ 10 umW or equivalently $\approx 1\%$. Even though such stability levels are experimentally possible, the value of the threshold P_{th} would also be affected by other factors like: i) Small variations in the particle size can change the exact value of the optical force. ii) Inhomogeneities in the surface charge of the particles and/or the substrate can change the exact value of the electrostatic barrier from one printing event to another.In practice, using laser powers very close to the threshold seems to lead to worse accuracy, as shown in figure 5.11. At this levels of laser power, printing events become rare, and it is possible that the experiment ends up biased by printing events on surface regions where the charge density is slightly smaller.

A more detailed discussion is open by considering the trajectories of the NPs . As discussed is subsection 5.5.1, once a particle enters the capture volume, it is dragged to the substrate by the optical force, following a deterministic trajectory. If the end position of the trajectory is inside the printing radius R_p, the electrostatic barrier can be overcame and the particle is printed. However, there are trajectories for which the end position on the substrate is outside the printing

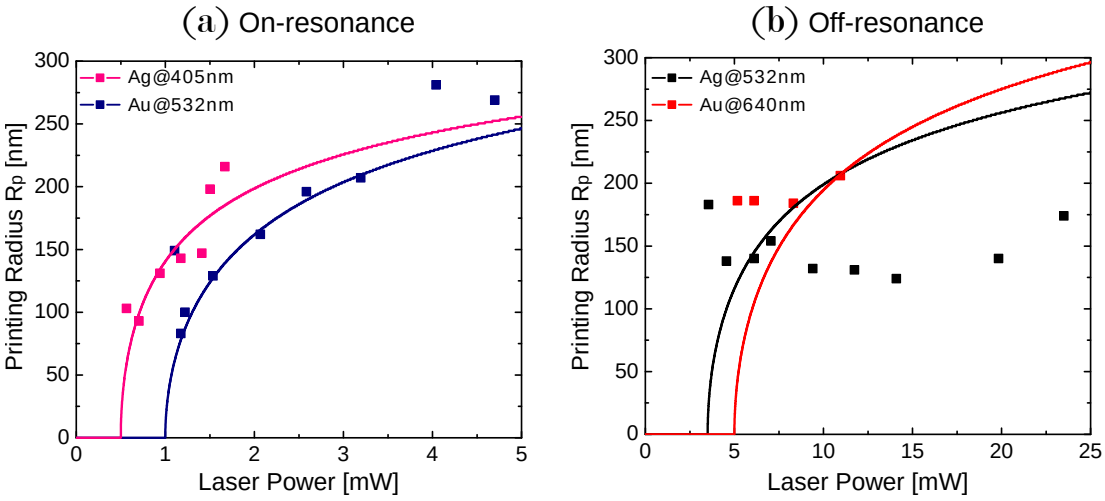

Figure 5.11: Solid lines: Theoretical printing radius l_{max} as a function of printing power for 60 nm Au and Ag NPs on-resonance (a) and off-resonance (b). Squares: Experimental root mean square error e_{RMS}. Pink: Ag at $\lambda = 405$ nm. Blue: Au at $\lambda = 532$ nm. Black: Ag at $\lambda = 532$ nm. Red: Au at $\lambda = 640$ nm.

radius. Those NPs cannot reach the substrate. Their faith may be determined by radial forces that tend to direct them towards the beam center. In this case they may cross R_p and be printed. Alternatively, Brownian motion may lead them outside the capture volume. In all cases, the final position of the printed particle is in the region inside R_p. Figure 5.12 show trajectories calculated for Au 60 nm NPs at different powers and wavelengths, but only those trajectories that end inside the printing radius R_p are plotted.

Figure 5.12a shows the situation for particles on-resonance and a printing power just above the threshold. Since radial forces on-resonance are weak, trajectories are mainly axial. The black box at the substrate level correspond to the printing radius R_p. Since it is small, there are not many trajectories that leads to printing. If the power is increased, the printing radius is larger and more trajectories become available, painted in pink in figure 5.12b. Particles with an initial position inside the black trajectories will continue to be printed inside the black box. On the other hand, a particle with an initial position in the pink region or outside any trajectory will eventually be printed in the pink box. The amount of particles on each box, i.e. the final distribution of printing errors, will depend on the spatial distribution of probability for the initial position of particles. Further increasing the printing power will provide more printing trajectories, as shown in light blue in figure 5.12c.

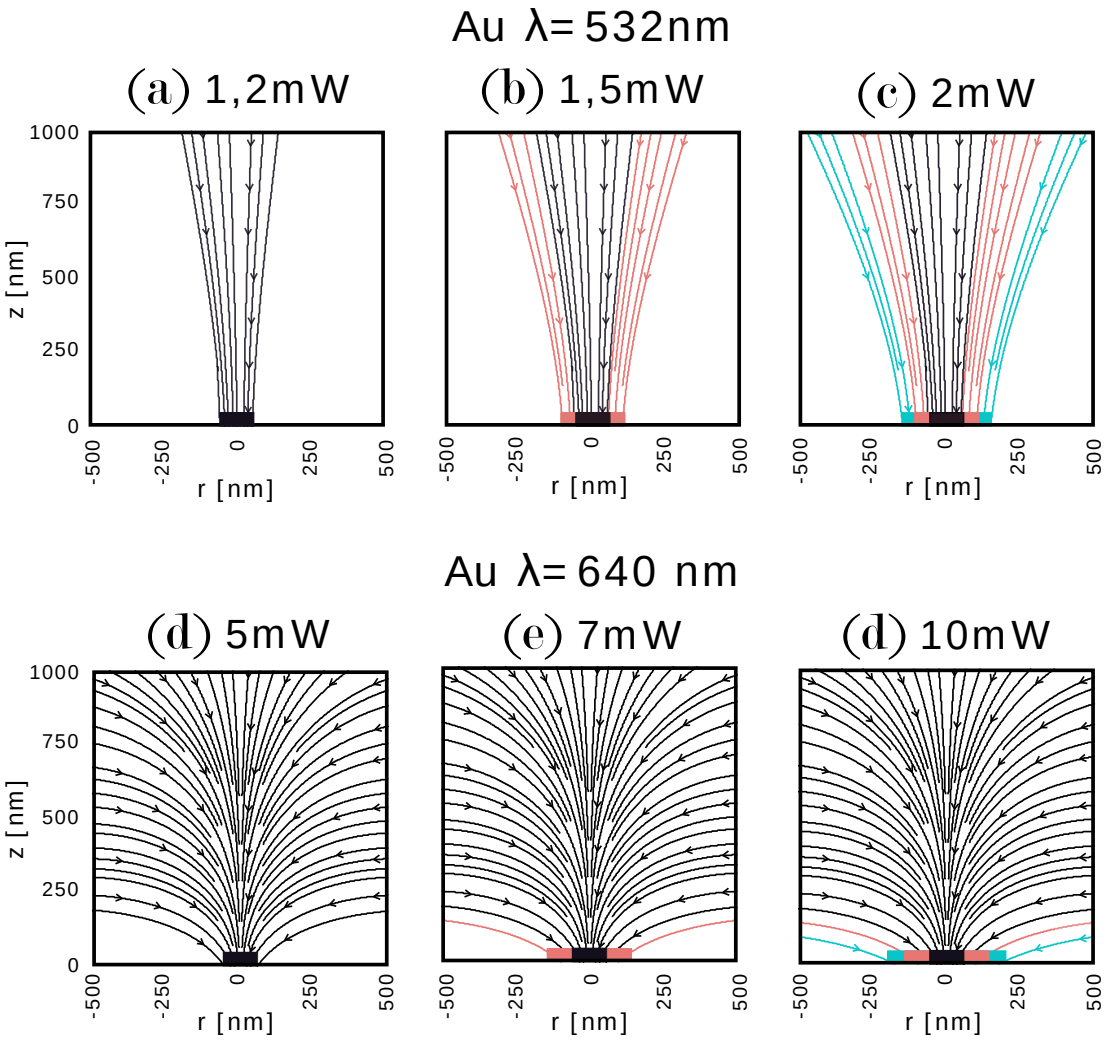

Figure 5.12: Calculated trajectories for 60nm Au NPs at different powers and wavelengths. Only the trajectories that end inside the printing radius R_p are shown. Pink and light blue lines are those trajectories that become available when increasing the power with respect to the lower value. Coloured boxed at $z = 0$ depict the final position of the trajectories. The added size of the boxes correspond to R_p.

A different scenario takes place when optical printing is performed with light off-resonance. First, R_p is no longer a good representation of the printing accuracy, as can be seen in figure 5.11b. Second, completely different NP trajctories are involved because radial and axial forces are comparable in this case. Figure 5.12d shows the printing trajectories for off-resonant printing at a beam power above the threshold. Therefore, when the printing condition is fulfilled (equation 5.10), the radial forces are strong enough to drive NPs towards the substrate

from a large portion of the 2 Π solid angle. The probability that a NP will diffuse into a position from which can be printed is high. The printing radius is again depicted with a black box. If the power is increased, new printing trajectories become available, as shown in pink in 5.12e. However, those trajectories cover a very small region of space and the probability that particle will diffuse into such an initial position is relatively small. Therefore, even though R_p is increased, the final distribution of printed NPs will not be modified, i.e. R_{90} will not increase. This explains the independence of the printing error with laser power observed off resonance.

6

Connecting Metallic Nanoparticles by Optical Printing

"Ya las vamos a hacer brillar pibe"

– Emiliano Cortés, *2014*

One of the most important open questions of Optical Printing concerns its resolution, understood as the minimum distance at which two particles can be printed in a controlled manner. As discussed in section 3.3, it has been shown in different experiments that nanoparticles (NPs) cannot be printed closer to each other than 300 nm. This apparently fundamental limitation has obstructed the use of optical printing for the fabrication of plasmonically coupled structures and circuits of connected NPs. In this chapter, the optical printing of nearby NPs is systematically studied. The aim is to understand the underlying physics in order to find strategies to overcome these impediments and allow the printing of arbitrary particles at any given inter-particle distance.

6.1 Fabrication and characterization of dimers

Optical printing resolution was systematically studied by fabricating dimers of two identical or different NPs and a wide range of target interparticle distances. First, an extended grid of well separated NPs (at least 2 μm from each other) was fabricated by optical printing. Then, each NP on the array is localized and optical

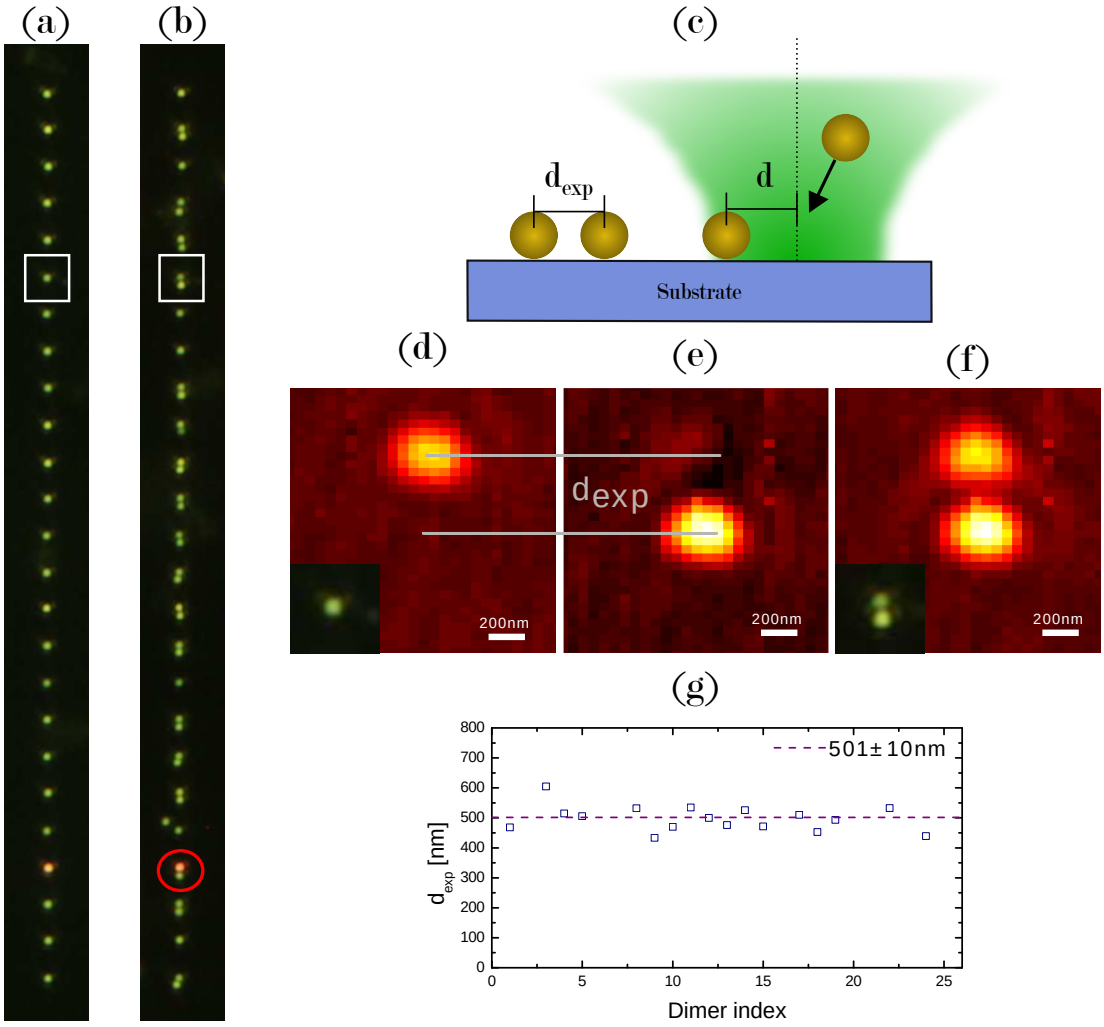

Figure 6.1: (a) Dark field image of an array of Au 60nm NPs printed at $\lambda = 532\ nm$ and $P = 1.2$ mW (b) Dark field image of the same array after a second particle was printed. (c) Definition of the set point d and the achieved d_{exp}. (d) Confocal scan of the particle marked with a white box, acquired at $\lambda = 532$ nm and $P = 0,4$ mW before the printing of the second particle. Inset show the dark field image of the particle. (e) Image of the second particle built from the subtraction of images f and d. (f) Confocal scan of the dimer marked with a white box. Inset shown dark field image of the same dimer. (g) Measured values of d_{exp}. The mean value is $\bar{d}_{exp} = 501$ nm $\pm$ 10 nm.

printing of a second NP was attempted in a position with a given separation distance from the already printed NP. The fabrication process consisted of the following steps:

1. The stage was moved so as to center the laser focus onto one of the NPs of the grid.

2. (Optional) The focus lock routine was performed to compensate any focus drift. This routine consists of moving the stage to an empty region of the substrate, find the set-point of the focus, and returning to the original position.

3. A 2D confocal image of the NP was adquired from which its precise location was obtained by computing the center of mass. The stage is moved to assure that the particle was centred with the printing beam.

4. Additional confocal scans were performed, which were subsequently used to determine the separation distance between the two NPs of the dimer.

5. The stage was then shifted to place the laser focus at the target position for the second NP d. Then the printing beam was unblocked until the second NP was detected, or a previously set maximum time of seconds passed without detection of a second NP.

6. Confocal scans of the fabricated dimer were acquired.

The wavelength of the beams can be chosen independently for each scan or printing procedure. The intensity was kept below the optical printing threshold during scanning and focusing steps. Unless stated otherwise, light polarized perpendicularly to the dimer axis was used, in order to avoid a scattering signal from electromagnetically coupled NPs.

The dimer fabrication process is schematically shown in figure 6.1a. It shows an array of isolated 60 nm Au NPs printed at $\lambda = 532$ nm and a laser power of $P = 1,2$ mW. Figure 6.1b. shows the same array after a second particle was printed, with a set point of $d = 500$ nm. Confocal scans before (e.g. figure 6.1d) and after (e.g. figure 6.1f) printing the second NP were acquired at $\lambda = 532$ nm and $P = 400\ \mu W$.

The production of dimers was characterized through the comparison of two magnitudes: i) The set-point d, defined as the distance from the center of the first NP to the center of the laser focus, i.e., the target position to print the second NP, and ii) The achieved interparticle distance d_{exp}. This two magnitudes are depicted on figure 6.1c.

For large separations, the interparticle distance d_{exp} can be obtained directly from the confocal scan of the fabricated dimer. However, for separations below the diffraction limit, this is no longer possible. In that case, an image of the isolated

second particle is created (see figure 6.1e), by subtracting the contribution of the first particle (acquired in step 4, figure 6.1d) to the image of the dimer (acquired in step 6, figure 6.1f). With this procedure, the position of each individual particle NP can be retrieved and the interparticle distance d_{exp} can be computed.

Figure 6.1g shows the measured values of d_{exp} for each of the dimers shown in figure 6.1b. Events where the second particle was not printed or looked significantly different (e.g. the reddish particle marked with a circle) were excluded from the analysis. In this example, the average achieved interparticle distance was $\bar{d}_{exp} = 501$ nm. The standard deviation was $S_{d_{exp}} = 41$ nm, which is consistent with the precision accuracy as described in chapter 5. The error in the determination of the mean value was $\Delta d_{exp} = \frac{S_d}{\sqrt{N}} = 10$ nm.

In the following sections, this method or variations of this method are applied to test the optical printing resolution for different configurations.

6.2 Limited lateral resolution in Au-Au homodimers

The first step wards identifying the physical mechanism of the repulsion causing the limited resolution is to determine its range of action. For that, dimers of 60 nm Au NPs were fabricated by optical printing at $\lambda = 532$ nm and a printing power of $P = 1,2$ mW, on top of a charged glass substrate prepared as described in section 5.1. The choice of the power was based on results from section 5.3 because is the power for which optical printing provides the highest precision. Various set-points d of interparticle separation distances were used, ranging from 800 to 60 nm. Figure 6.2a show example dark field images of the fabricated dimers. Figure 6.2b shows the average achieved interparticle distance d_{exp} versus the set-point d. For large separation distances (> 300nm) the printing process takes place smoothly, and the dimers can be fabricated according to design. For $d < 300$nm, a deviation from the set-point toward larger separations is observed, concomitantly with a dramatic increase in the average waiting time for printing (6.2c). Clearly, a repulsive interaction is preventing the second NP from being printed correctly. For separations smaller than 250 nm the repulsion is strong enough to completely prevent the printing of the second particle, and dimers cannot be fabricated. At this condition no printing event was observed even for waiting times 20-fold longer than the time needed to print at larger set-points.

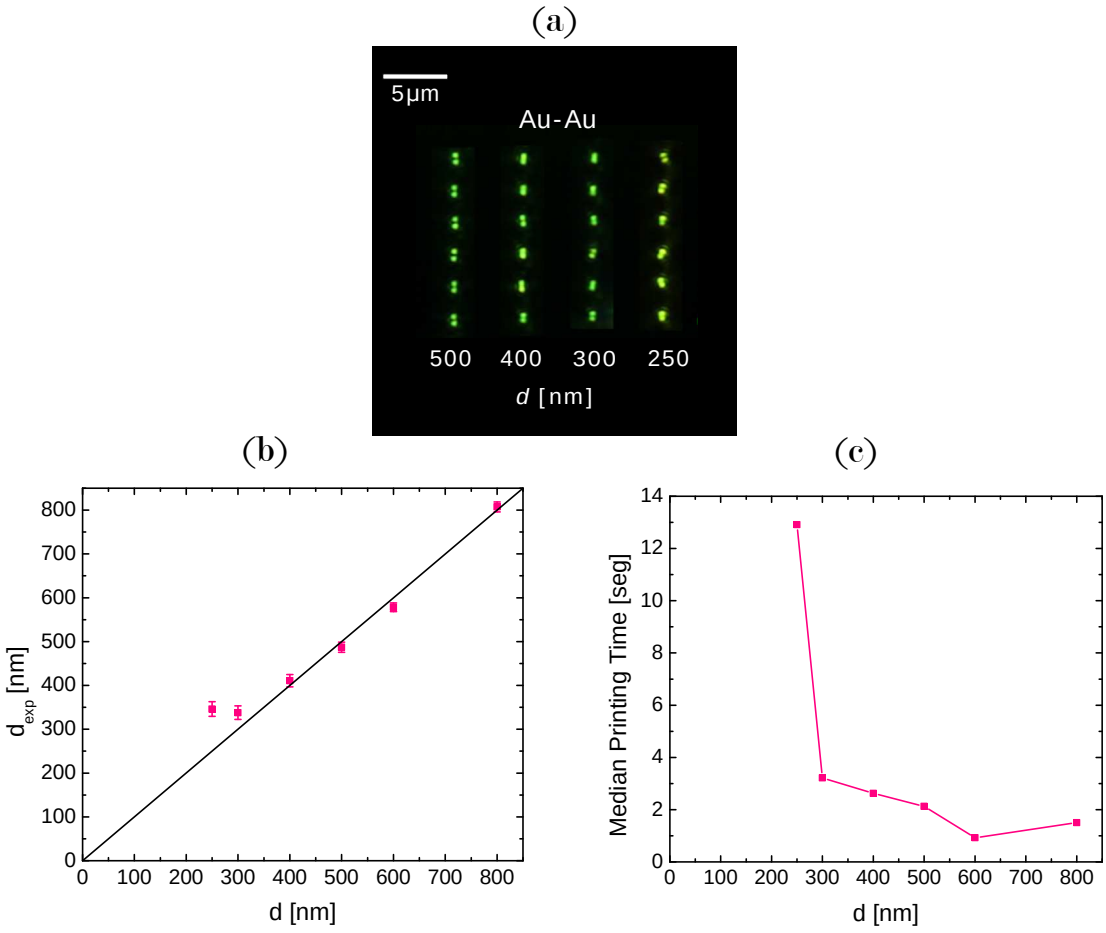

Figure 6.2: (a) Dark field images of Au-Au dimers fabricated at different interparticle distances d. (b) Measured interparticle distances d_{exp} vs set point d for Au-Au dimers. The ideal behavior is shown as a line with slope = 1 (c) Median waiting time for the printing of the second particle in the dimer, as a function of the distance to the first particle d.

The three different behaviors observed: no interaction, interaction with printing, and interaction without printing, are consistent with previous observations with 200 nm Ag NPs by the group of Scherer[57], as discussed in section 3.3. The value of 300 nm as a limit for controllably printing is also consistent with the reported by the group of Feldmann.[63]

It is interesting to note that these limit distance values are comparable to the laser beam waist at the focal plane $w_0 = (266 \pm 3)$ nm. The parameter w_0, also called the Gaussian beam radius, represents the radius at which the field has decreased to $1/e$ of its maximum, and the intensity has decreased to $1/e^2$. This could indicate that the repulsion is light-induced and appears when the already

printed particle is illuminated, as will be further discussed in next section.

6.3 Fabrication of Ag-Au heterodimers

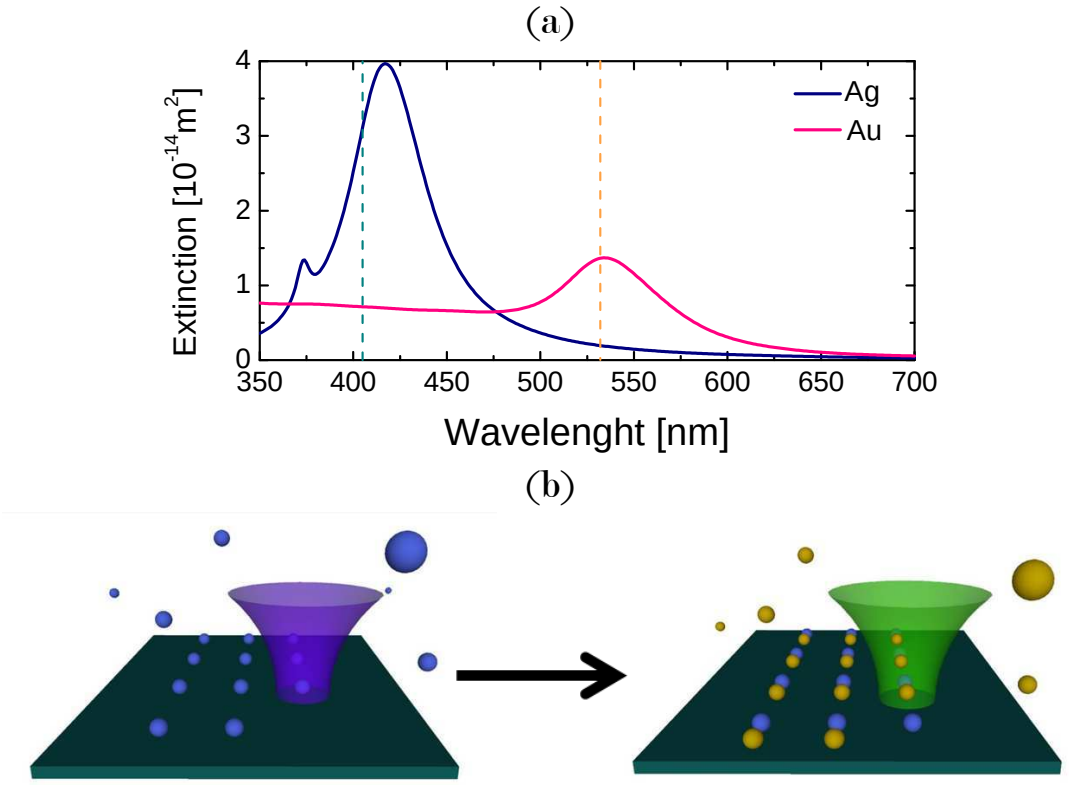

Figure 6.3: (a) Extinction cross sections as a function of wavelength calculated using Mie theory for 60 nm Au (blue) and Ag (pink) NPs in water. Vertical lines show the printing wavelengths, at 405 nm and 532 nm. (b) Schematic of the process for dimers fabrication: first Ag NPs were optically printed with the 405 nm laser. Then the colloidal suspension is replaced by Au NPs, which are subsequently printed using the 532 nm laser.

The results shown in section 6.2 make plausible that the repulsive interaction that prevents the fabrication of dimer at close separation is produced by light interaction with the already printed NP. In this section experiments designed to test this hypothesis are presented, applying a printing strategy that minimizes light interaction with the NPs already present on the substrate. The strategy consist of fabricating heterodimers, printing first a Ag NP, and then a Au NP using light of 532 nm, as depicted in figure 6.3b. Figure 6.3a show the extinction

cross section of 60 nm Au and Ag NPs , calculated using Mie theory. As can be seen, Ag NPs are practically transparent at $\lambda = 532$ nm.

The protocol for fabrication and characterization of Ag-Au dimers was analogous to the one used for Au-Au dimers and described in section 6.1. First a grid of 60 nm Ag NPs was printed using the 405 nm laser. Then the colloidal suspension was exchanged for one of 60 nm Au NPs . Ag NPs were localized by confocal scattering imaging at 405 nm and the Au NPs were printed and detected using the 532 nm laser.

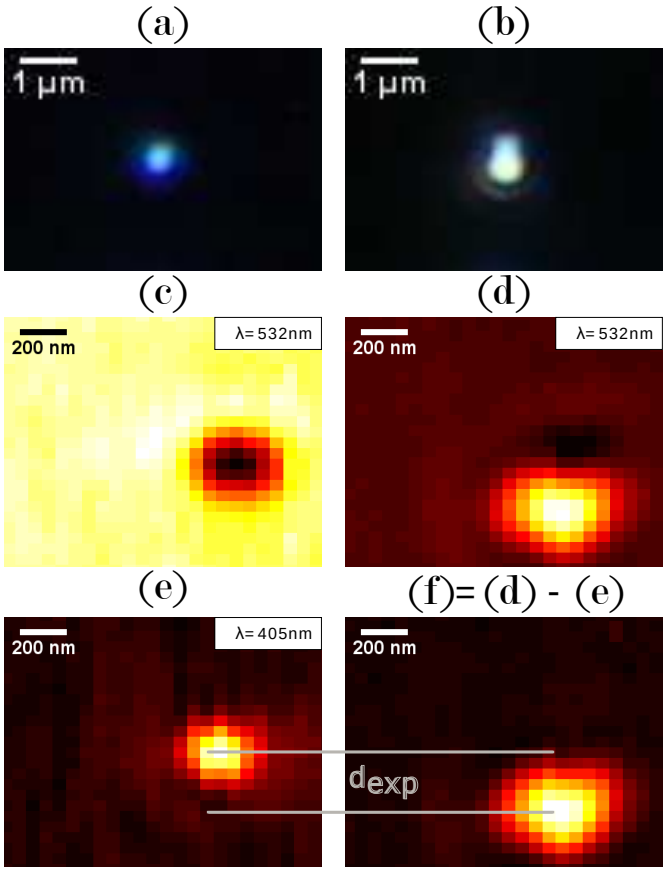

Figure 6.4: Dark field images of (a) Ag 60 nm NP and (b) Ag-Au dimer at $d = 200$ nm with Ag NP on top. Confocal scattering images of (c) Ag NP scanned with 532 nm laser. (d) heterodimer scanned with 532 nm laser (e) Ag NP scanned with 405 nm laser (f) image obtained after subtracting the signal received by a single Ag NP (image (c)) to the dimer confocal scattering at 532 nm (image (d)).

Determination of the achieved interparticle distance d_{exp} is explained in figure 6.4. First, two confocal scattering images of the single Ag NP were acquired, one at 405 nm (figure 6.4e) and the other at 532 nm (figure 6.4c). The image at 405

nm was used to locate the Ag particle. Then, after the Au NP was printed, a confocal scattering image of the Ag-Au dimer was acquired at 532nm (figure 6.4d). Both the Ag and Au NPs contributes to the signal. Subtracting the scattering image of the Ag NP at 532 nm allows to obtain the image of the isolated Au NP (figure 6.4f). Comparison of images 6.4f and 6.4e provides the measured d_{exp}.

To justify this procedure, it must be remembered that, as discussed in section 4.1, elastic scattering from independent sources can interfere at the detector. In this way, intensity of the image 6.4c of the single Ag particle is proportional to

$$I_{Ag} \propto |r + s_{Ag}|^2 = |r|^2 + |s_{Ag}|^2 + 2|r||s_{Ag}|cos\phi_{Ag} \tag{6.1}$$

where ϕ_{Ag} is the phase difference between the reflected $|r|$ and the scattered $|s_{Ag}|$ light.

Then, the intensity of image 6.4d is proportional to

$$\begin{aligned} I_{Ag-Au} \propto |r + s_{Ag} + s_{Au}|^2 =& |r|^2 + |s_{Ag}|^2 + 2|r||s_{Ag}|cos\phi_{Ag} \\ &+ |s_{Au}|^2 + 2|r||s_{Au}|cos\phi_{Au} \\ &+ 2|s_{Au}||s_{Ag}|cos\left(kd + \phi_{Au} - \phi_{Ag}\right) \end{aligned} \tag{6.2}$$

Substracting 6.1 to 6.2

$$I_F \propto |s_{Au}|^2 + 2|r||s_{Au}|cos\phi_{Au} + 2|s_{Au}||s_{Ag}|cos\left(kd + \phi_{Au} - \phi_{Ag}\right) \tag{6.3}$$

which gives the image shown in 6.4f. The first two terms have a maximum at the Au NP position. The last term can be considered as an estimation of the error for the optical caracterization. In this case it can be neglected since $|s_{Ag}(532nm)| \ll |s_{Au}(532nm)|$.

Ag-Au heterodimers were fabricated with various interparticle separation distances, with at least 20 dimers for each distance. Figure 6.5a shows example dark field images of several Ag-Au dimers, when the separation is smaller than the diffraction limit ($<$ 300 nm) the heterodimers appear as a single object in the dark-field images. Nevertheless, the achieved interparticle distance d_{exp} could be determined using the above described method. The average d_{exp} is shown in figure 6.5b, as a function of the target separation d. Remarkably, in this case optical printing is possible for interparticle distances d all the way down to 60 nm for Ag-Au heterodimers, i.e. until the NPs are in contact.

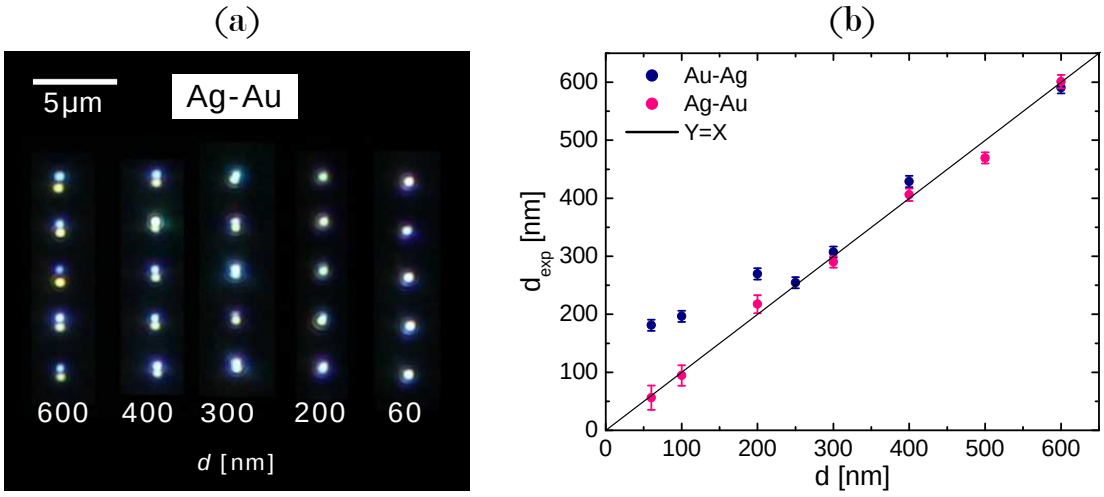

Figure 6.5: (a) Dark field images of Ag-Au dimers fabricated at different interparticle distances d. (b) Measured interparticle distances d_{exp} vs set point d for Ag-Au dimers (pink) and Au-Ag dimers (blue). The ideal behavior is shown as a line with slope = 1

In order to further characterize the fabricated heterodimers and to corroborate the optical measurements of d_{exp}, the dimers were visualized using a field-emission scanning electron microscopy (FE-SEM). The achieved interparticle distance d_{exp}^{SEM} measured with the (FE-SEM) was compared with its optical $d_{exp}^{optical}$ counterpart through the calculus of $S_{d_{exp}}(d) = \sqrt{\langle \left(d_{exp}^{SEM} - d_{exp}^{optical} \right)^2 \rangle}$ where the average is over many dimers at the same set point d. For large set points, the difference between two methods is small ($S_{d_{exp}}(500\text{ nm}) = 20$ nm) and increases for closer set points ($S_{d_{exp}}(60\text{ nm}) = 50$ nm). 15% of the fabricated Ag-Au dimers were compared, and the average over all dimers and set points was $S_{d_{exp}} = 34$ nm, which is comparable to the radius of the particle. This means that the optical measurement of d_{exp} is an accurate method. Also, it indicates that particles are strongly fixed to the surface and do not move during rinsing of the sample with water and drying in vacuum for SEM measurements.

For the fabrication of structures and circuits of NPs, is not only important to control the interparticle distance and to be able to connect NPs, but also to control the relative orientation of the printed NPs with respect to the substrate/device frame of reference. We interrogated the possibilities of optical printing to fabricate Ag-Au dimers with controlled orientation. For this, the angle θ between the vertical axis (x) of the substrate and the vector defined from the centre of Ag NP to the centre of Au NP was analysed, as outlined in the inset

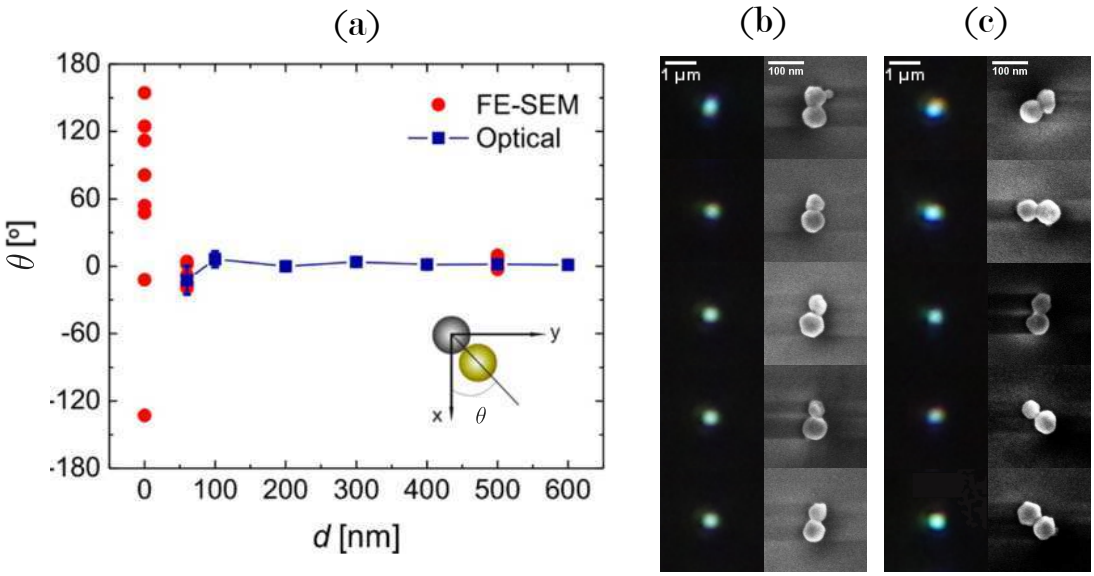

Figure 6.6: (a) Angle θ between the vertical axis (x) of the substrate and the vector defined from the center of Ag NP to the center of Au NP. The optical measurement of θ corresponds to the mean values obtained from analysis of confocal scattering images of at least 20 dimers for each value of d. Several values of θ obtained from the analysis of FE-SEM images are shown for $d = 500$, 100, and 0 nm. (b,c) Dark field (left) and FE-SEM (right) images of Ag-Au heterodimers fabricated at $d = 60$ nm (b) and $d = 0$ nm (c). In (b) the Ag NPs is always the one on the top.

of figure 6.6a. The same figure shows the mean values of θ for dimers fabricated at various interparticle distances d ranging from 600 to 60 nm, obtained from the analysis of confocal scattering images. As can be seen, the optical printing is accurate in terms of directionality within an error smaller than 8° for all values of d from 600 nm down to 100 nm. For the connected NPs ($d = 60$ nm), the variability takes a slightly higher value of 20°. There are two possible reasons for this increment. First, due to the limited printing accuracy, a larger variation in θ is expected as d becomes shorter. Second, a contribution due to contact interactions between the NPs is also likely.

As an example, Figure 6.6b shows dark-field and FE-SEM images of five connected Ag-Au NP dimers fabricated by setting the interparticle distance to 60 nm. On the dark field images the dimers appear as single diffraction limited scatterers. On the FE-SEM images the orientational control is evident. Ag-Au NP dimers can be fabricated as well if the interparticle distance is set to zero, but the orientational control is completely lost (Figure 6.6c).

An additional interesting experiment to test if the repulsions are light-induced is to invert the order of fabrication of heterodimers. We printed first a Au NP at 532 nm and then a Ag NP at 405 nm. Following this order, the already printed Au particle is not longer transparent to the printing wavelength of the second particle, because Au extinction is not negligible at 405 nm (see figure 6.3). At least 20 Au-Ag dimers were fabricated at each interparticle distance d, and the mean achieved distance d_{exp} is shown in figure 6.5b (blue data). It is not possible to connect the NPs with this printnig strategy. The minimum value of d_exp was 250 nm, which is slightly smaller than for the Au-Au case.

Based on these results, and recalling that aside from their optical properties, the Ag and Au NPs have practically identical physicochemical properties, such as size, charge and surface capping molecules, it is reasonable to conclude that the repulsive interaction that prevents the fabrication of Au-Au and Au-Ag NP dimers with separations smaller than 250 nm is light-induced. The experiments also show that optical printing is capable of placing NPs at arbitrary separation distances and also to connect them with controlled orientation, if the interaction of the already printed NPs with the light used for printing is avoided. However, nothing has been said about the causes of the light-induced repulsion yet. In the following sections, several mechanisms are proposed and experimentally tested.

6.4 Evaluation of scattering

Upon illumination, light scattered by the already printed NP may lead to disortions of the optical force field. It may shift the position of maximum axial force from the target position or may induce optical forces on other NPs in solution as it happens in optical binding[73, 74, 65, 75]. During the optical printing process, both the fixed and the approaching particle polarizes, with an induced dipole parallel to the electric field. Considering than not only the far-field but also the near and intermediate fields produced by a radiating dipole depend on the orientation of the dipole, it is reasonable to expect that the interaction between particles varies with the polarization of light.

It is then interesting to calculate the optical force field in the presence of a fixed particle. This was done by a collaborator, Lukáš Chvátal, the Group of Optical Micro-manipulation Techniques (OMITEC) at the Institute of Scientific Instruments of the Czech Academy of Sciences (Brno, Czech Republic), using

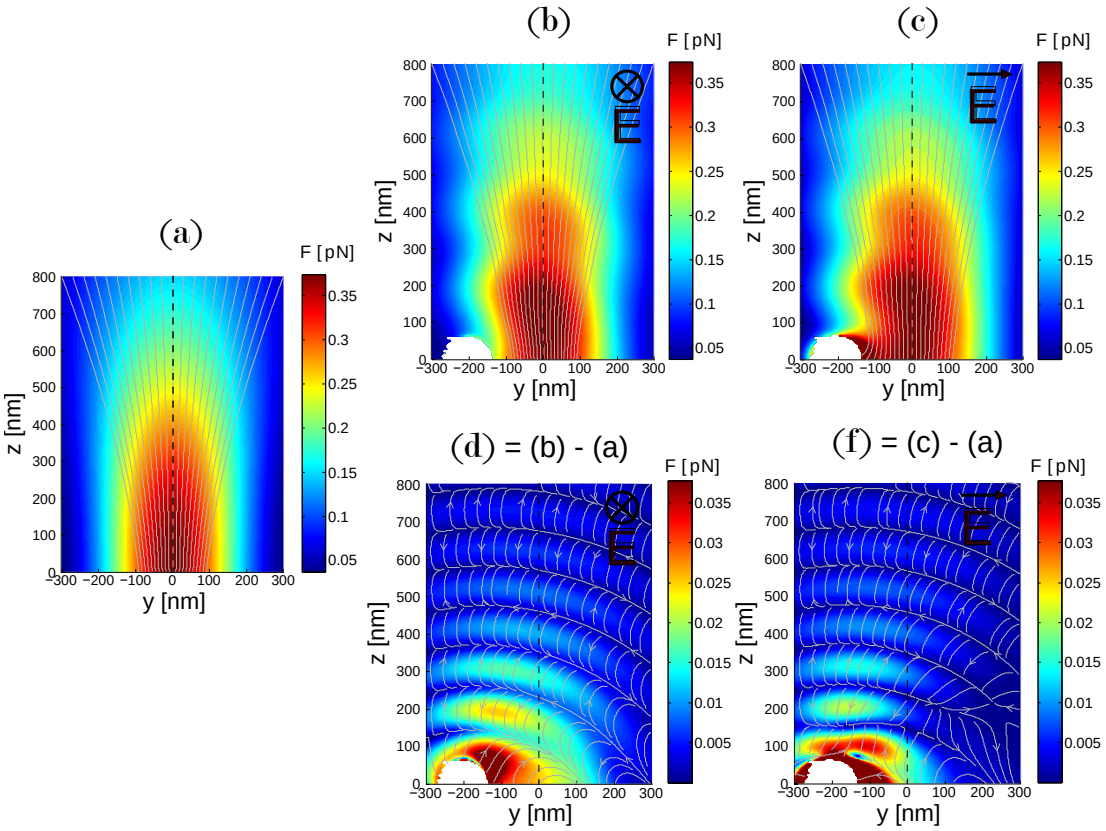

Figure 6.7: Optical force maps. (a) Total Force in the absence of any fixed particle. (b) Total force in the presence of a fixed particle 200 nm away from the beam centre, and a polarization perpendicular and (c) parallel to the y axis. (d) Estimation of the forces caused by the fixed particle in a perpendicular polarized beam, obtained by subtracting (b)-(a). (f) Estimation of the forces caused by the fixed particle in a parallel polarized beam, obtained by subtracting (c)-(a). In all cases, linearly polarized Gaussian beam of $\lambda = 532$ nm, with a waist of $w_0 = 265$ nm and power of $P = 1,2$ mW was used, as in the experiments. White areas correspond to inter-penetrated particles and were excluded from the map. Calculus made by using Generalized Lorenz–Mie theory. Grey lines are field lines. The modulus of the force is colour coded. Data on this figure were computed by Lukáš Chvátal from OMITEC.

their own code based on the Generalized Lorenz–Mie theory with an extension to multiple spherical particles, as explained in reference [76]. First, the force map in the absence of any fixed particle was calculated for Au 60 nm NPs . Figure 6.7a shows the total optical force field for a Gaussian beam of $\lambda = 532$ nm, with a waist of $w_0 = 265$ nm and power of $P = 1,2$ mW exerted on a Au 60 nm NP. Grey lines indicate force field lines, which according to the discussion of section 5.5.1 can be interpreted as trajectories for the particle being printed. The

force map is consistent with the obtained with the Rayleight approximation with Kuwata polarizability (equations 1.30 and 1.31). For example, the maximum calculated forces are $F = 0.36$ pN with Lorenz–Mie theory and $F = 0.31$ pN with Rayleight-Kuwata model. Then, the optical force fields in the presence of a fixed particle 200 nm away from the centre of the beam were calculated for both polarizations, corresponding to an experimental configuration where it was impossible to print a second particle. Figure 6.7b and 6.7c show the calculated force field for perpendicular and parallel polarizations, respectively. In both cases, there are many field lines (trajectories) that end in the substrate. For parallel polarization there are lines that end close to the fixed particle, indicating an attractive interaction between particles. The influence of the fixed particle in the optical field is therefore not strong enough to prevent the second particle from reaching the surface. In order to better visualize it, the difference between the force fields in the presence and in the absence of a fixed sphere is calculated. The resulting subtraction can be interpreted as the distortion of the force field produced by the fixed sphere. This is shown in figure 6.7d for perpendicular and 6.7f for parallel polarization. Oscillations in the sign of the force are typical of optical binding interactions. For both polarizations, the interaction force is at least one order of magnitude weaker than the optical force exerted by the laser beam.

The effect of the polarization of the printing beam in the fabrication of Au homodimers was also experimentally studied. The fabrication procedure of section 6.2 was repeated, for dimers oriented both parallel and perpendicular to the electric field of the printing beam and different interparticle distances d. Example dark field images of the dimers are shown in figure 6.8a. Figure 6.8b shows the average achieved interparticle distance d_{exp} versus the set-point d. Remarkably, the results are independent of the orientation of the dimer. The distance d for which printing becames impossible is the same in both cases, as well as the minimum achieved interparticle distance. Figure 6.8c shows the median waiting time for the printing of the second particle, versus the set-point d. Again, similar behaviours are obtained for both orientations. These results indicate that the polarization of the beam does not have a major role in the light-induced repulsion.

The calculus of optical binding forces, together with the experimental observation that the optical printing process and its limitations are independent of the

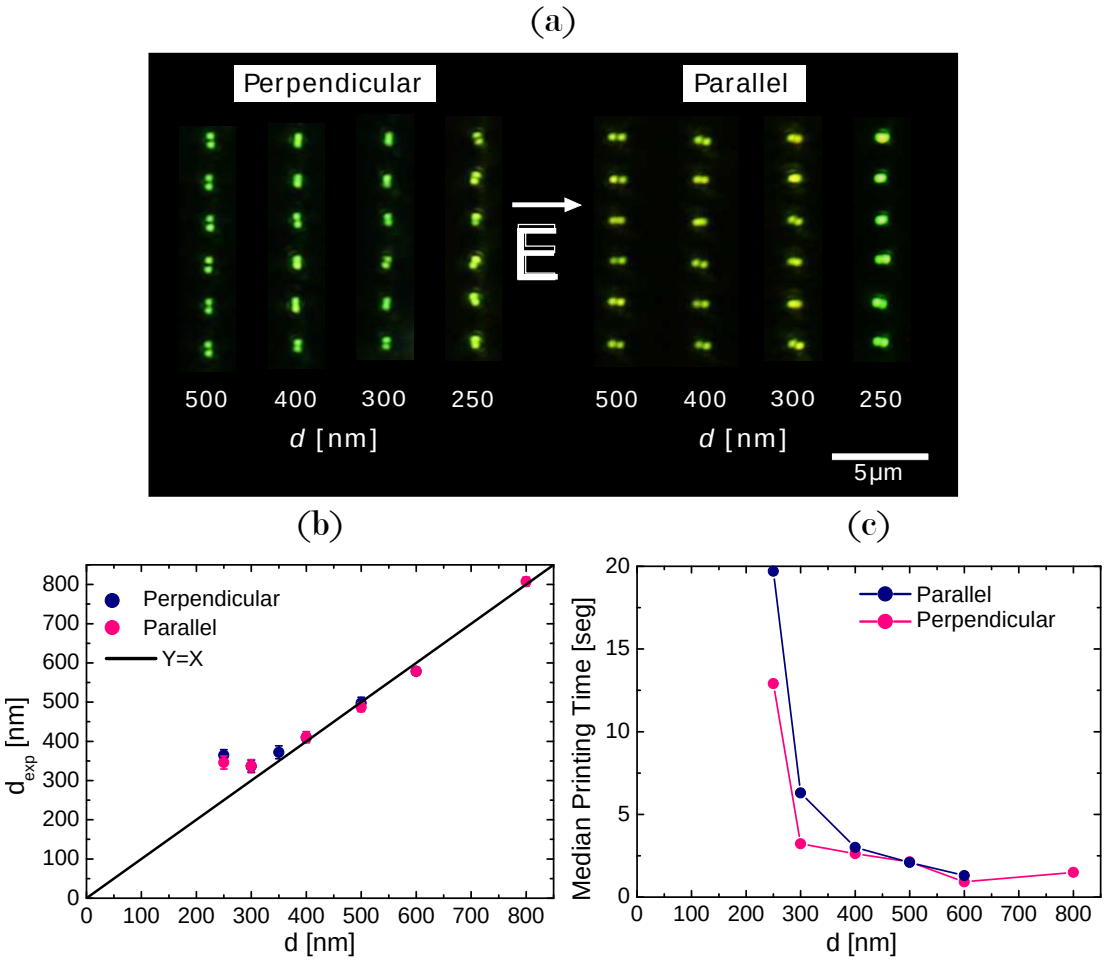

Figure 6.8: (a) Dark field images of Au-Au dimers fabricated at different interparticle distances d and two orientations with respect to the polarization of the printing beam. (b) Measured interparticle distances d_{exp} vs set point d for Au-Au dimers Parallel to the polarization (pink) and Perpendicular (blue). The ideal behavior is shown as a line with slope = 1 (c) Median waiting time for the printing of the second particle in the dimer, as a function of the distance to the first particle d, for both orientations.

polarization of the beam, indicate that the light-induced repulsions are not due to optical binding interactions, or any other mechanism caused by scattering of light by the printed particle. Therefore, other mechanisms based on absorption of light must be studied, as discussed in the following section.

6.5 Evaluation of absorption

6.5.1 Light-induced heating during Optical Printing.

Upon illumination, the printed NPs absorb light and generate heat, which is transferred to the surrounding medium leading to a local temperature increase. The generated heat Q depends on the distance d of the fixed NP to the centre of the printing beam, and can be estimated using equations 1.19 and 1.29 by[77]

$$Q(d) = I(d, z = 0)\sigma_{abs} = \sigma_{abs}\frac{2P}{\pi w_0^2}e^{-\frac{2d^2}{w_0^2}} \tag{6.4}$$

Considering that the thermal conductivity of glass $\kappa_g \simeq 1.3\ \frac{\mathrm{W}}{\mathrm{mK}}$ is similar to that of water $\kappa_w = 0.58\ \frac{\mathrm{W}}{\mathrm{mK}}$, a simple estimation of the temperature map around a fixed particle was obtained considering an homogeneous medium. In that case, insertion 6.4 on 1.20 gives the temperature increase ΔT_0 of the fixed particle, as a function of the separation distance to the centre of the printing beam d

$$\Delta T_0(d) = \frac{\sigma_{abs}}{2\pi^2 a\kappa}\frac{P}{w_0^2}e^{-\frac{2d^2}{w_0^2}} \tag{6.5}$$

Solution of equation 6.5 is shown in figure 6.9a, for Ag and Au NPs with a diameter of 60 nm immersed in water, illuminated by a beam of wavelength $\lambda = 532$ nm with a waist of $w_0 = 265$ nm. Temperature increases above one hundred degrees are expected for Au NPs at distances to the beam shorter than 250 nm, but they rapidly decrease for larger distances. In contrast, the temperature increase for the Ag NP is much smaller, below ten degrees for all distances.

The characteristic time $\tilde{\tau}_T$ for the establishment of the steady-state temperature field around a Au 60 nm sphere on water is $\tilde{\tau}_T \simeq 25$ ns, as calculated using equation 1.21 for water with $\rho = 10^3\ \frac{\mathrm{kg}}{\mathrm{m}^3}$, $c = 4.18\ 10^3 \frac{\mathrm{J}}{\mathrm{kg°K}}$ and $\kappa = 0.58\ \frac{\mathrm{W}}{\mathrm{m°K}}$. This time interval is much shorter than the characteristic time scales of the optical printing process (as discussed in section5.5.1). Therefore, the temperature field is set almost instantaneously after the laser beam is turned on to print a second NP.

At a first sight, calculations shown in figure 6.9 may seem unphysical, given that they estimate temperatures well above the boiling point of water. However, it must be noted than temperature fields decay rapidly with increasing distance to the particle, typically in one to two hundreds of nanometers. It has been ob-

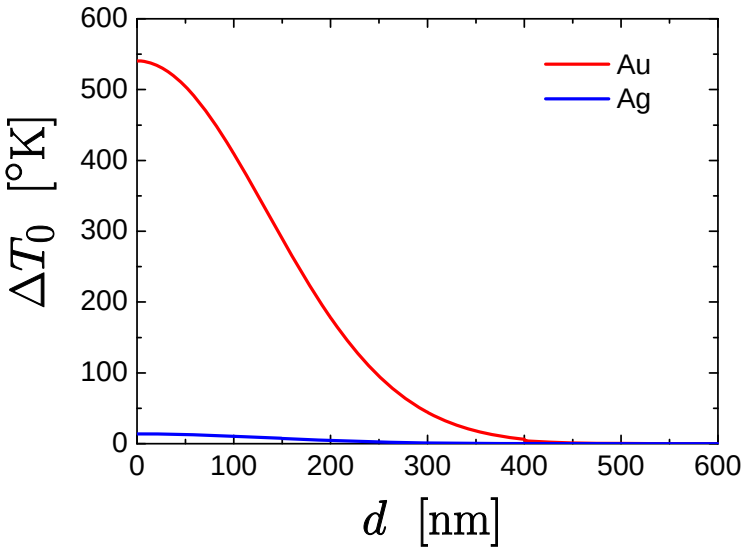

Figure 6.9: Surface temperature increase of a 60 nm (Au or Ag) in water as function of the distance d to centre of a Gaussian beam of wavelength $\lambda = 532$ nm, with a waist of $w_0 = 265$ nm and power of $P = 1,2$ mW, calculated using equation 6.5 with a thermal conductivity of $\kappa_w = 0.58\ \frac{\mathrm{W}}{\mathrm{mK}}$

served that water can be superheated beyond the boiling point up to the spinodal decomposition temperature 594 °K in such small volumes[78, 79, 80]. Another possibility is that a small bubbles form around the NP[81]. In any case, calculations show that considerably high temperatures and temperature gradients arise around the fixed NP when the printing laser is placed at separation distances below 200 nm. Therefore, thermally driven repulsive effects are plausible to occur. In section 6.6, a discussion about the possible nature of such photo-thermal effects are given.

6.5.2 Study of heat dissipation

The work presented in this section is part of a collaboration with the Experimental Solid State Group of the Imperial College London (United Kingdom), directed by Prof. Stefan Maier. In order to study if the light-induced repulsions are caused by the locally increased temperature around the NPs , different heat dissipation schemes were tested. In a first experiment, a heat conductive substrate as sapphire was employed. Thermal conductivity of sapphire is $\kappa_{sapphire} \simeq 24\ \frac{W}{mK}$, which is around 20 times larger than the conductivity of glass $\kappa_{glass} \simeq 1.3\ \frac{W}{mK}$. Apart from the thermal properties, sapphire substrates are transparent and allow dark field imaging equivalently to glass.

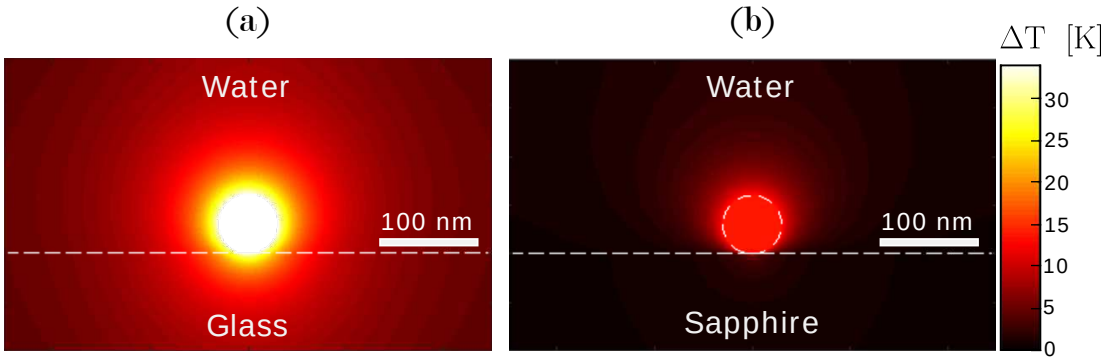

Figure 6.10: Temperature increase map of a single Au 60nm sphere in the centre of a Gaussian beam on (a) glass and (b) sapphire substrates, considering $\kappa_{glass} = 1.3\ \frac{W}{mK}$ for the thermal conductivity of glass and a $\kappa_{sapphire} = 24\ \frac{W}{mK}$ for sapphire, and an irradiance of $I = 1\frac{\mathrm{mW}}{\mu\mathrm{m}^2}$ at $\lambda = 532$ nm. Calculations were made by Thomas Brick and Pablo Albella from the Experimental Solid State Group, using COMSOL software to solve numerically equation 1.17

For a NP on top of a substrate with high thermal conductivity, the approximation of an homogeneous medium (equation 6.5) is no longer valid. Therefore temperature maps were calculated solving numerically the full heat diffusion equation 1.17 using COMSOL software. Figure 6.10 show the temperature increase maps produced by a single Au 60 nm sphere in water, fixed on top of a glass and a sapphire substrates, illuminated with an irradiance of $I = 1\frac{\mathrm{mW}}{\mu\mathrm{m}^2}$ in a resonant Gaussian beam ($\lambda = 532$ nm).

The temperature increase of a NP on top of sapphire is around 3 times smaller than on glass. Also, temperature increase on sapphire is more confined close to the particle with respect to glass. And is below one third of its maximumm for distances larger than one diameter.

Optical printing of Au NPs on sapphire was experimentally tested. For that, sapphire substrates were functionalized with polyelectrolytes following the same protocol employed for glass (see section5.1). The first noticeable fact was that $\simeq 2.4$ times less power was required for printing. The threshold power for Au NPs at $\lambda = 532$ nm was found to be $P_{th} = (0.45 \pm 0.06)$ mW. The reason for this can be two-fold: i) The assembly process of polyelectrolytes can be different on sapphire, resulting in a lower superficial charge. ii) A short-ranged attraction between the heat-releasing particles and the heat-conductive surface is taken place, as described in reference [82]. This last possibility is further discussed in section 6.6.2.

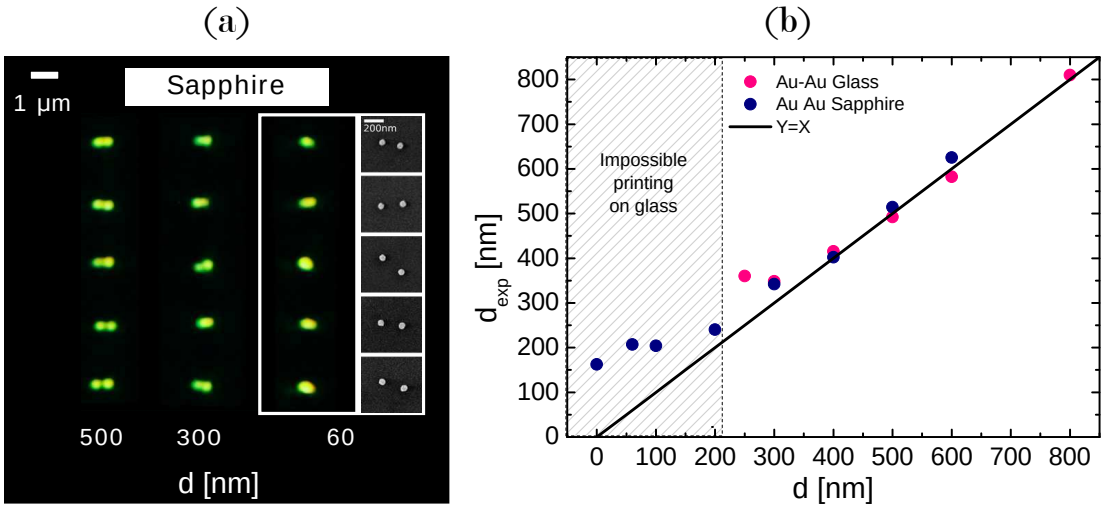

Figure 6.11: (a) Dark field images of Au-Au dimers fabricated on sapphire substrates at different interparticle distances d, with a beam of $\lambda = 532$ nm and $P = 0.5$ mW. In the white inset, SEM images of the fabricated dimers are shown. (b) Measured interparticle distances d_{exp} vs set point d for Au-Au dimers on sapphire (blue). For comparison, the results on glass are included (pink). The ideal behavior is shown as a line with slope = 1 and the grey zone correspond to distances for which printing on glass is impossible.

Dimers of Au NPs were fabricated by optical printing at set points d ranging from 60 nm to 600 nm and $P = 0.5$ mW, to keep the temperature as low as possible. Example dark field images of the dimers are shown in figure 6.11a, and figure 6.11b shows the average achieved interparticle distance d_{exp} versus the set-point d. Remarkably, optical printing of a second particle is possible at any interparticle distance. However, for distances d below 250 nm, the achieved distance d_{exp} is larger than the set point. The inset of figure 6.11a shows SEM images of the fabricated dimers at a set point of $d = 60$ nm, i.e. aiming to connect the particles. Even though a second particle was printed with a fairly well controlled orientation, the average achieved distance was $d_{exp} = (211 \pm 12)$ nm.

These results show that reducing the temperature of the already printed particle by simply changing the substrate has measurable consequences in the achieved inter-particle distance for the optical printing of Au NPs dimers. An additional reason for the temperature reduction is that less power is required for printing. Although it is still not possible to fully connect the particles when using a sapphire substrate, the 300 nm inter-particle threshold was overcome.

Optical Printing next to Au nanodisks In order to gain a better understanding on the origin and magnitude of the thermal effects, alternative NPs were studied. Increasing the contact area between the NPs and the substrate is an effective way of achieving a better heat dissipation. In order to test this approach, Au nanodisks (NDs) were fabricated by top-down methods onto sapphire substrates. The NDs have a considerably larger contact area with the substrate than the nearly spherical colloidal NPs.

Au NDs were fabricated using electron beam lithography, with the help of Toshihiko Shibanuma in the clean room facilities of Imperial College, in United Kingdom. Positive tone resist PMMA (poly(methyl methacrylate)) was coated on a sapphire substrate and baked at 180 °C for 5 minutes. The substrate was exposed with an electron beam followed by a development procedure with MIBK (methyl isobutyl ketone): IPA (isopropanol) = 1:3 solvent. The nanostructured substrate was covered with 2 nm chromium adhesion layer and 50 nm gold film deposited by thermal evaporation. Subsequent PMMA removal by lift-off process with acetone provided the gold nanodisks.

Employing the above described method, Au NDs of 70 nm, 100 nm and 150 nm diameter and 50 nm height were fabricated on sapphire substrates. Figure 6.12a and 6.12b show dark-field and SEM images for the 70 nm and 150 nm Au NDs fabricated arrays. Figure 6.12d shows the absorption cross sections and temperature increase spectra for the fabricated structures upon illumination, calculated solving numerically the full heat diffusion equation 1.17 with COMSOL software. The irradiance was $I = 4.6\frac{\mathrm{mW}}{\mu\mathrm{m}^2}$ which correspond to the particle set in the centre of the printing laser at $\lambda = 532$ nm with a power of $P = 0.5\mathrm{mW}$. The calculations show that although the disks have greater volume and equal or higher absorption cross sections than the spheres, (as shown in figure 6.12c), their temperature increase is expected to be around 5 times smaller (figure 6.12d).

Following the same procedure of section 6.1, 60 nm Au NPs were printed close to Au NDs in order to fabricate ND-NP dimers with different separation distances. The results are analysed in terms of the gap between particles, instead of the centre to centre distances as done until now. Figure 6.13a shows a schematic of the AuNP-AuND dimers printing experiment. The set gap is the distance between the centre of the beam and the border of the disk. The experimental gap Gap_{exp} is the measured surface to surface distance between the printed NP and the disk.

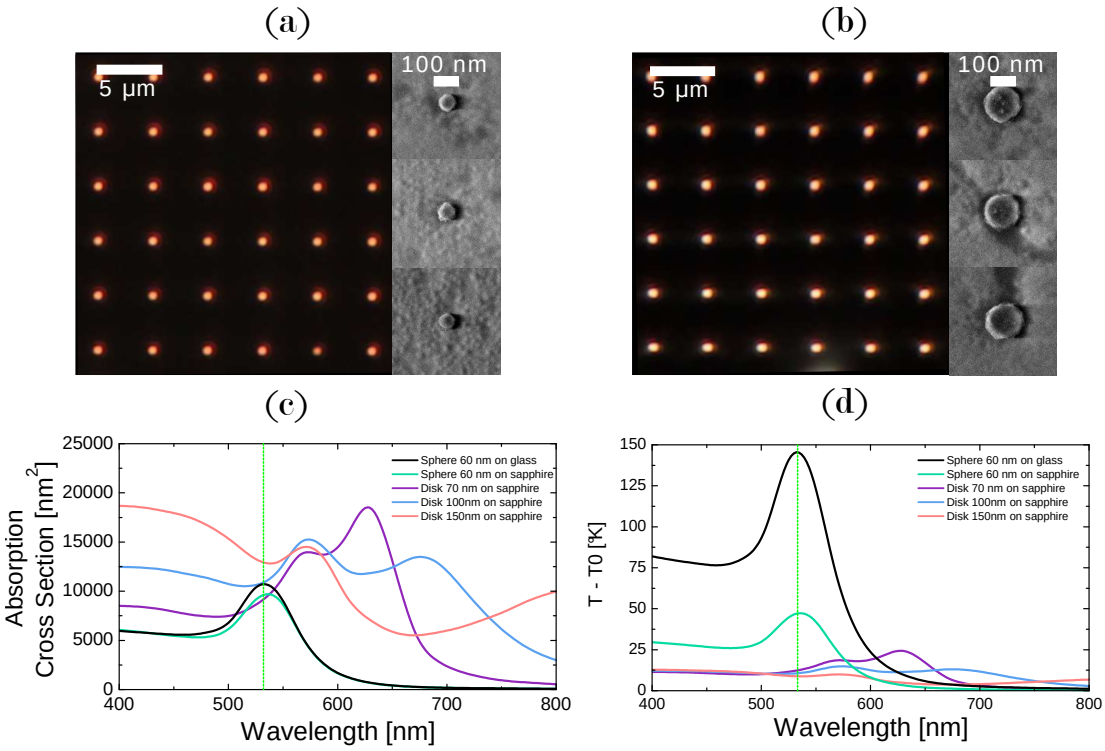

Figure 6.12: (a) Dark field image of 70 nm NDs (left) and representative FE-SEM images of the structures (right) (b) Dark field image of 150 nm NDs (left) and representative FE-SEM images of the structures (right) (c) Calculated Absorption Cross Section σ_{abs} versus wavelength for Au NPs and NDs (d) Calculated temperature increase of a Au NPs and NDs versus wavelength under an irradiance of $I = 4.6\frac{\text{mW}}{\mu\text{m}^2}$, typical value for printing on sapphire at $\lambda = 532$ nm. Calculations were made by Pablo Albella solving the full heat diffusion equation 1.17 with COMSOL software.

Representative dark field images are shown in figure 6.13b for 70 nm ND-NP. The inset (up) shows a FE-SEM image of a particle printed with a set gap of 0 nm and an experimental $\text{Gap}_{exp} = (35 \pm 5)nm$. Both particles look similar on FE-SEM images, but through the scattering spectra the presence of a disk and a spherical NP can be corroborated, as shown in the inset (down). Figure 6.13c shows the measured gap versus the set gap for all disk sizes. Optical printing of NPs particle was possible for all gaps and NDs sizes. The negative set gaps of Figure 6.13c correspond to optical printing attempts with the beam centred on the ND. In those cases, NPs were printed, but on the substrate, not on top of the ND. The smaller average G_{exp} achieved were below 100 nm for all disk sizes, which correspond to values impossible to obtain with dimers of spherical Au NPs on glass or sapphire. This demonstrates that engineering the dissipation of heat

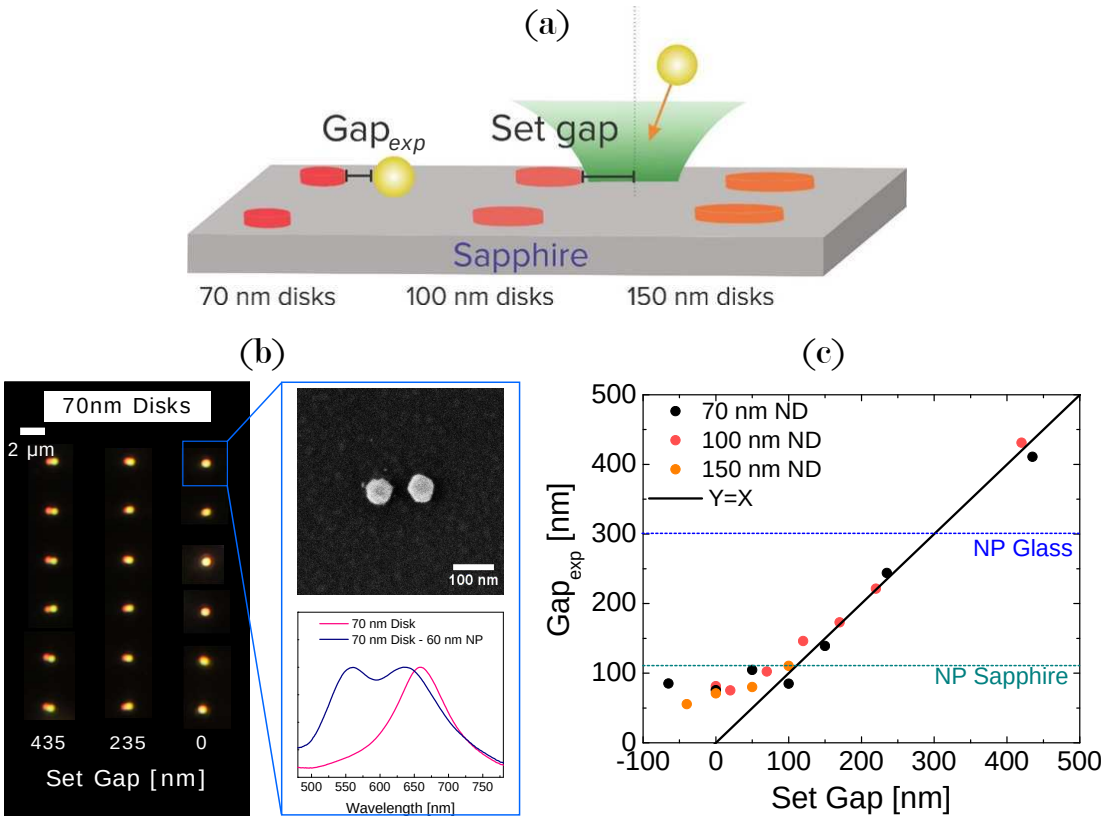

Figure 6.13: (a) Schematic of the AuNP-AuND dimers printing experiment. The set gap is the distance between the centre of the beam and the border of the disk. The Gap$_{exp}$ is the surface to surface distance. (b) Dark field images of optically printed AuNPs next to 70 nm AuNDs, for different set-gap (435 nm, 235 nm and 0 nm). The inset shows a FE-SEM image of one obtained AuNP-AuND dimer for a set distance of 0 nm and its scattering spectra before printing (pink line) and after printing (blue line). (c) Measured experimental gap of AuNP-AuND dimers for different printing set gaps between the structures. Three different AuNDs diameters were employed: 70 nm (black dots), 100 nm (pink dots) and 150 nm (orange dots). Black line represents unperturbed printing. For comparison, the minimum achievable gaps for Au NPs on glass and sapphire are indicated with horizontal lines.

through the NP geometry is a viable avenue to control the optical printing of nearby NPs . However, is was still not possible to connect the particles.

These results provide additional evidence against the repulsion mechanisms via scattered light discussed in section 6.4. The scattering cross sections at 532 nm of a 60 nm spherical NP and the 70 nm NP have similar magnitudes. Furthermore, the 150 nm ND has a scattering cross section 7-fold larger than a 60 nm Au NP, but presents the smallest repulsion.

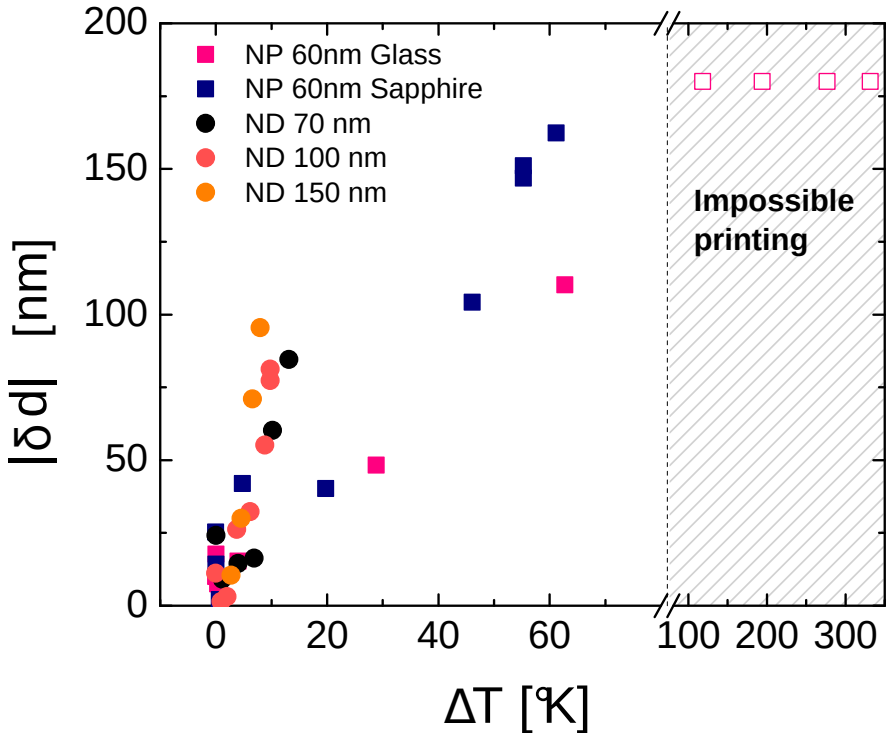

Figure 6.14: Absolute value of the dfference between set gap and measured gap $|\delta d|$ versus ΔT temperature increase of the fixed NP. Empty pink squares in the grey zone correspond to impossible printing and therefore their value of δd is arbitrary.

It is interesting to quantitatively compare the influence of temperature increase in the printing performance of all the experiments presented so far. To this end the variable δd was calculated, defined as the difference between the set gap and the measured gap According to this definition, δd may be interpreted as the deviation from the unperturbed behaviour. The temperature increase ΔT of the fixed particle on the substrate was also computed in each case, considering its distance to the printing beam; for example, larger set gaps will have smaller temperature increases because the particle is illuminated with the edge of the Gaussian beam. Fig 6.14 shows the value of absolute value of $|\delta d|$ versus ΔT. Even though they correspond to diverse systems, including spheres and disks in glass and sapphire for many set gaps, they remarkably group into the same tendency. This proves that temperature is indeed a key parameter to predict the performance of optical printing to place NPs together. The threshold between possible and impossible printing is consistent with the boiling temperature of water. It is a noticeable fact that a relatively slow surface temperature increase

of ten degrees can cause a repulsive force as strong as the optical counterpart. In the following section, discussion about the physical nature of the repulsion is provided.

6.6 Plausible photo thermal effects during optical printing

In the previous sections, evidence has been given to support the idea that the resolution of otical printing is limited by photo-thermal effects arising from the plasmonic heating of NPs on the substrate. In this section, convection, thermophoresis and thermo-osmosis are discussed as possible physical mechanisms.

6.6.1 Convection

Fluid around the printed NPs is hotter than the bulk solution, establishing a temperature gradient and producing buoyancy-driven natural convection[83]. The magnitude of convective flows during the optical printing process can be estimated using the formalism presented by Quidant et. al.[17]. In particular, the order of magnitude of the velocity $\tilde{V}$ of the fluid induced by a structure of typical size $\tilde{L}$ and a temperature increase ΔT can be estimated as

$$\tilde{V} = \frac{\tilde{L}^2 \beta g \rho \Delta T}{\mu} \tag{6.6}$$

with β the dilatation coefficient of water, μ the dynamic viscosity, ρ the density and g the gravitational acceleration. For $\tilde{L} = 60$ nm (diameter of the NP), $\Delta T = 100$ °K, $\rho = 10^3 \ \frac{kg}{m^3}$, $\beta = 10^{-4}$ °K^{-1}, $\mu = 10^{-3} \ Pa \ s$ and $g = 9.8 \ \frac{m}{s^2}$, the obtained characteristic fluid velocity is $\tilde{V} \simeq 0.3 \ \frac{\text{nm}}{s}$. Such flows translate into drag forces of $F_{drag} \simeq 2 \ 10^{-7}$pN using equation 5.3, which are six order of magnitude weaker than the optical forces. This means that the existent convective flows do not play any relevant role in the optical printing process.

6.6.2 Thermophoresis and Thermo-osmosis

Thermophoretic forces arise as a result of the inhomogeneous liquid-solid interfacial tension when a temperature gradient is present at the interface between a

fluid and a surface. Temperature gradients induce a slip flow velocity V_s on a liquid-solid boundary, which can be calculated from the excess enthalpy $h(z)$ in the boundary layer[84]

$$V_s \cdot \hat{t} = -\frac{1}{\mu}\int_0^\infty z h(z)\frac{\nabla T}{T}\mathrm{d}z \equiv \chi\frac{\nabla T}{T}\cdot\hat{t} \tag{6.7}$$

where $\hat{t}$ is the unit vector tangential to the surface, μ is the dinamic viscocity of the fluid, T the temperature, χ the mechanocaloric cross-coefficient, and z the perpendicular distance to the surface. Depending on the nature of the interaction, i.e. the sign of χ, the fluid can be pushed towards the hotter or the colder region. If the surface corresponds to a suspended particle in a non-isothermal solvent, this force induces the migration of the particle, known as *thermophoresis*[85, 86, 87], as depicted on figure 6.15a. On the other hand, if the surface is a fixed boundary, a long ranged movement of the fluid is established known as *thermo-osmosis*.[88, 89], as depicted on figure 6.15b.

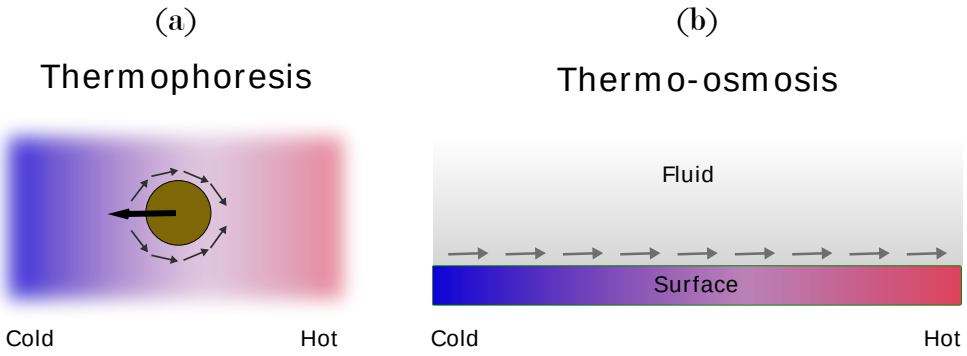

Figure 6.15: Schematic of (a) thermophoresis and (b) thermo-osmosis. A temperature gradient induces the motion of the liquid towards the hot region. Close to a suspended particle, this flow pushes the particle towards the cold region.

Temperature fields around a hot nanostructure typically decay in about 100 nm (see, per example, figure 1.4 or 6.10). Therefore, extreme temperature gradients as high as $10^9 - 10^{10}\ \frac{\mathrm{K}}{\mathrm{m}}$ are produced, potentially leading to strong thermophoretic interactions. Since optical printing involves suspended NPs and substrates, both thermophoresis and thermo-osmosis may take place. For simplicity, both phenomena are addressed separately .

Thermophoresis. Thermophoresis is the movement of suspended particles in non-isothermal solvents. In this context, Equation 6.7 can be employed to derive

a more convenient description, where the macroscopic thermophoretic velocity V_{tph} of the particle is proportional to the external temperature gradient ∇T and can be calculated using the thermodiffusion coefficient D_T

$$V_{tph} = -D_T \nabla T \tag{6.8}$$

For large particles the thermodiffusion coefficient is related to χ through[90] $D_T = \frac{2\chi}{3T}$. Since this D_T is typically positive, particles move from hot to cold regions.

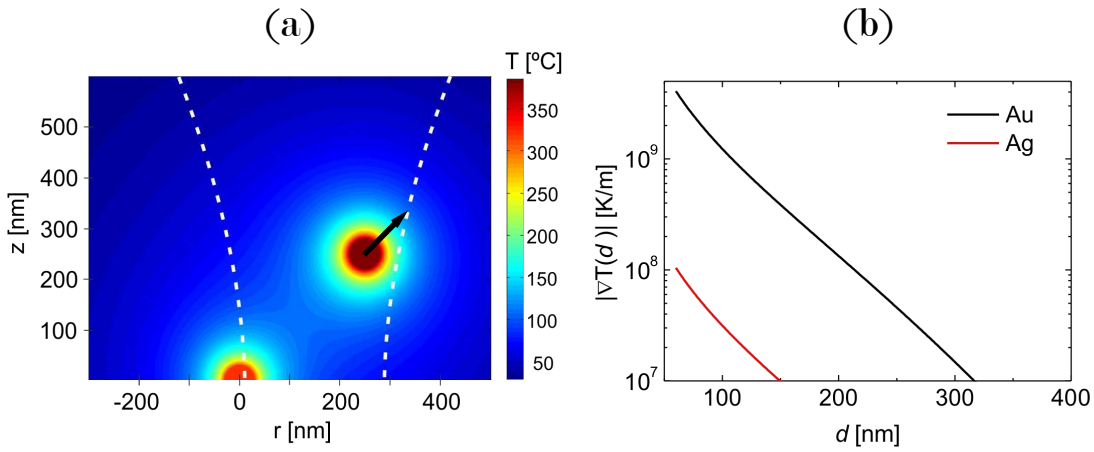

Figure 6.16: (a) Snapshot of the temperature field produced when a Au NP at (0,0) is approached by another Au NP at (250 , 250) nm, that is being printed with the laser focus centred at $d = 150$ nm. The region between the two particles is hotter than the bulk solution, and therefore a thermophoretic force appears (black arrow). (b) Temperature gradients evaluated at $r = d$ for a Au or a Ag NP at (0,0) as a function of the distance to the printing beam d. Calculus made for a focused Gaussian laser beam of $\lambda = 532$nm, with a waist of $w_0 = 265$nm and power of $P = 1,2$ mW, as in the experiments of sections 6.2 and 6.3

Next, thermophoresis is evaluated as a plausible cause for the light-induced repulsion during the optical printing, considering the cases of Au-Au homodimers on glass (section 6.2) and Ag-Au heterodimers on glass (section 6.3).

During the printing process, both the fixed and the approaching NP absorb light and contribute to the temperature field. Figure 6.16a shows the calculated temperature increase induced by light absorption of a fixed and an approaching NP, when the printing beam is set at a distance $d = 150$ nm from the fixed particle. For simplicity and since thermal conductivity of glass is comparable to water, temperature maps were calculated analytically using equations 6.5 and 1.20 considering an homogeneous medium. The region between the two particles is hotter

than the bulk solution, and therefore a thermophoretic force appears that pushes the approaching NP away (indicated with a black arrow). Inserting equation 1.20 into expression 6.5, it is possible to calculate the temperature gradient generated around a NP when it is illuminated by a Gaussian beam centred at a distance d from the NP

$$\nabla T_0(r=d) = -\frac{\sigma_{abs} P}{2\pi^2 \kappa w_0^2 d^2} e^{-\frac{2d^2}{w_0^2}} \tag{6.9}$$

The solutions of equation 6.9 for the cases of a 60 nm Au NP and a 60 nm Ag NP, and a focused Gaussian beam of 532 nm as the one used in the experiments, are shown in figure 6.16b. The strong dependency of the generated temperature gradients with d, explains qualitatively the sharp transition from interacting without printing to correct printing behaviors for Au-Au homodimers (section 6.2). The much smaller magnitude of the gradients produced by the Ag NP are consistent with the feasibility to fabricate Ag-Au heterodimers at arbitrarily close separations. Following this argument, thermophoresis can qualitatively explain the experimental observations.

However, it is not straightforward to compute quantitatively the magnitude of thermophoretic forces because experimental values of D_T are scarce in general, particularly scant for metallic particles and inexistent for temperature gradients as high as the ones present during optical printing. Nevertheless, it is interesting to perform some calculations using a range of reported vlues of D_T. As reviewed by Piazza and Parola[86], most of the measured coefficients range in the order of $10^{-12} - 10^{-11} \frac{\mathrm{m}^2}{\mathrm{sK}}$. The three experiments with the most similar conditions to those presented here are (i) the one performed by Bucholtz[91] et. al. with laser-induced thermophoresis of silica microspheres in viscous liquids, where $D_T = 2.2\ 10^{-11} \frac{\mathrm{m}^2}{\mathrm{sK}}$ (ii) the one with fullerenes in toluene performed by Bou-Ali et. al.[92], which is the only report involving heat conducting nanoparticles, where $D_T = 4.5\ 10^{-11} \frac{\mathrm{m}^2}{\mathrm{sK}}$ (iii) the one with Au nano triangles by Zheng et. al.[93], which is the only work involving Au nanoparticles but the value of D_T is not reported but estimated to be consistent with an order of magnitude of $10^{-12} \frac{\mathrm{m}^2}{\mathrm{sK}}$. As example, Figure 1.17 shows calculations made with $D_T = 4.5\ 10^{-11} \frac{\mathrm{m}^2}{\mathrm{sK}}$.

Thermophoretic velocities were calculated at numerous positions around an already printed Ag or Au NP on glass, for various positions d of the printing laser. They were calculated using equation 1.20 for the temperature fields, therefore considering the heat dissipation of the glass substrate to be the same as water. Thermophoretic velocities can be translated into thermophoretic forces using the

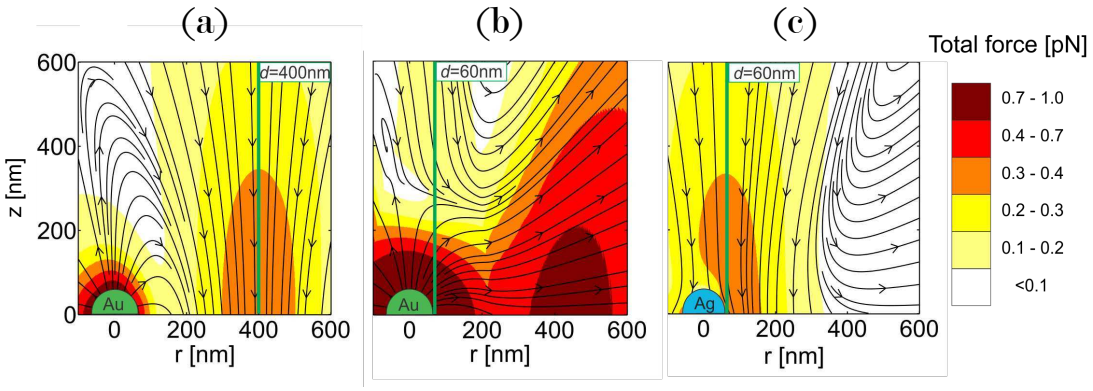

Figure 6.17: Maps of total force (optical plus thermophoretic) acting on a 60 nm Au NP for positions around a Au or Ag NP printed at (0,0), for different set points d of the laser focus. The arrows denote the direction of the resultant force and its magnitude is colour coded. (a) printed NP of Au, $d = 400$ nm; (b) printed NP of Au, $d = 60$ nm; (c) printed NP of Ag, $d = 60$ nm. A thermodiffusion coefficient $D_T = 4.5\ 10^{-11} \frac{\mathrm{m}^2}{\mathrm{sK}}$. The immobilized NPs at (0,0) are drawn schematically with a diameter of 120 nm (i.e., two times their diameter) because calculations with interpenetrating NPs have no physical meaning

Stokes equation (5.3), including the temperature dependence of the viscosity of water. The optical force produced by the laser beam on the Au NP that is being printed was added to the thermophoretic force in order to obtain total force maps. In figure 6.17, three total force maps are shown. The force lines can be interpreted as trajectories in the absence of Brownian motion. If the laser is relatively far from the printed NP, e.g., at 400 nm (figure 6.17a), thermophoretic forces are negligible in comparison to the optical forces, and the printing path of the Au NP is practically undisturbed. As the laser gets closer to the printed Au NP and light absorption increases, the thermophoretic repulsive force becomes more important. For example for d = 60 nm (figure6.17b), thermophoretic repulsion dominates and no trajectory reaches the substrate; i.e. printing is not possible at all. In contrast, if the printed NP is made of Ag (figure6.17c), the thermophoretic forces are significantly weaker, and optical printing is possible at any interparticle separation.

Calculations of figure 6.17 have no free parameter except the rather arbitrary chosen value of $D_T = 4.5\ 10^{-11} \frac{\mathrm{m}^2}{\mathrm{sK}}$. It was found that values of D_T ranging from 2 to 20 $10^{-11} \frac{\mathrm{m}^2}{\mathrm{sK}}$ lead to calculated force fields compatible with the experimental observations. The best fit to the onset of repulsion observed on the fabrication of Au-Au dimers on glass is obtained with a value of 8 $10^{-11} \frac{\mathrm{m}^2}{\mathrm{s°K}}$.

Thermophoretic attraction to the substrate. As described in section 6.5, the observed threshold of laser power for optical printing a NP on sapphire is 2.4 times lower than on glass. The minimum power required for printing on glass was $P_{th} = (1 \pm 0.05)$ mW, while on sapphire it was $P_{th} = (0.45 \pm 0.06)$ mW. This fact can be explained in terms of an interaction between the heat realeasing NP and the surface caused by thermophoresis. This force was theoretically introduced in a paper from Elperin et.al. in 2003.[82] When a particle of radius a releases heat at a rate Q in a host medium of thermal conductivity κ_1 and is separated a distance z from a planar interface with another medium of thermal conductivity κ_2, a the thermophoretic force arises between the NP and the substrate given by

$$F = \frac{\pi a \eta \chi}{\kappa_1 z^2} \frac{\kappa_1 - \kappa_2}{\kappa_1 + \kappa_2} Q \ \hat{z} \tag{6.10}$$

Where $\hat{z}$ is the unit vector normal to the interface. If the thermal conductivity of the host medium is smaller than the one of the substrate, the force is attractive for heat releasing particles.

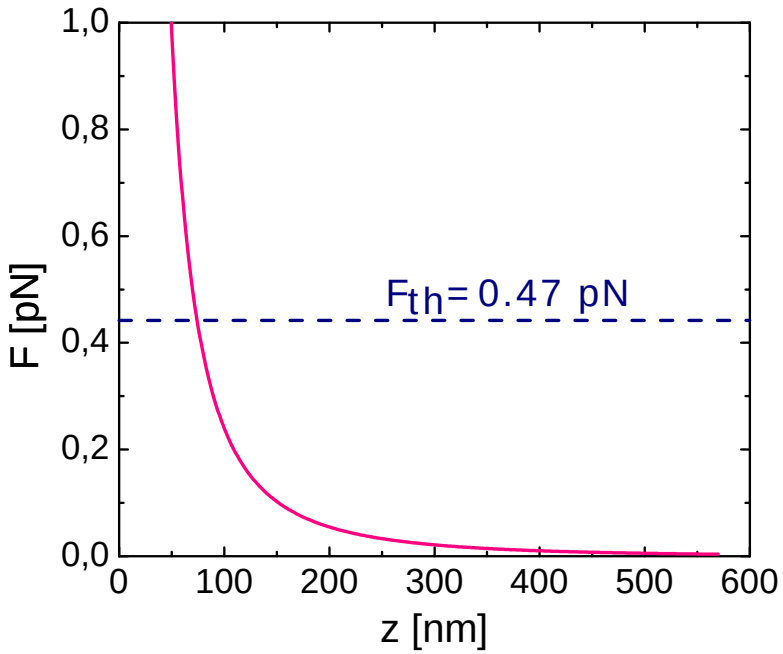

Figure 6.18: Thermophoretic force acting on a 60 nm Au NP in water as a function of the distance to a sapphire substrate, according to equation 6.10, when the NP is in the centre of a Gaussian beam of $\lambda = 532$ nm with a waist $w_0 = 265$ nm and $P = 0.5$ mW. Blue horizontal line denotes the electrostatic repulsion, as estimated in section 5.5.2.

Figure 6.18 shows the thermophoretic force as a function of the distance z, for Au 60 nm NPs in water ($\kappa_1 = 0.58\ \frac{\mathrm{W}}{\mathrm{mK}}$), close to a sapphire substrate of $\kappa_{sapphire} = 24\frac{W}{mK}$. The particle was considered to be in the centre of a Gaussian beam of $\lambda = 532$ nm with a waist $w_0 = 265$ nm and $P = 0.5$ mW. The value of $Q = \sigma_{abs} I$ can be estimated using expression 1.29. The value of χ was $10^{-10}\frac{\mathrm{m}}{\mathrm{s}^2}$ (see subsection **Thermo-osmosis**). The repulsive electrostatic threshold is also shown, with the value of $F_{th} = 0.47$ pN, as estimated in section 5.5.2. For distances below the hundred nanometers, the thermophoretic attractive force is stronger than the electrostatic threshold, contributing to the printing process, and probably explaining the lower laser power needed for printing on sapphire.

Thermo-osmosis. This phenomenon consist of the generation of a liquid flow close to a solid boundary with inhomogeneous temperature. The first microscale observation of thermo-osmotic flows was reported very recently by Bregulla et. al.[88] in 2016.

Upon illumination with the printing beam, the temperature gradient around the fixed NP would induce the flow of water close to the substrate towards the NP. Then, to preserve mass continuity, the streamlines must be closed, and vertical flows perpendicular to the substrate must appear at the position of the printed NP. The stationary state is reached almost immediately, in tens or hundreds of nanoseconds.[17]. This flow can exert drag forces on the particle being printed, disrupting its movement.

In order to fully characterize the thermo-osmotic flow field, numerical simulations using COMSOL were performed by Thomas Brick in the Experimental Solid State Group of the Imperial College London (United Kingdom). First, the temperature maps were calculated by solving the heat diffusion equation (1.17), which in the stationary state and low Rayleigh number is (see section 1.3)

$$-\kappa(r)\nabla^2 T(r) = q(r) \tag{6.11}$$

Once the temperature map was calculated, the slip velocity $V_s = \chi\frac{\nabla T}{T}$ on the substrate-water interface was obtained according to equation 6.7. This velocity was imposed as a boundary condition when solving the Navier-Stokes equations for stationary flows of low Reynolds[17]

$$-\nu\nabla^2 V(r) = f_e(T(r)) \tag{6.12}$$

where ν is the kinematic viscosity. $f_e\left(T\left(r\right)\right)$ is the force per unit mass due to temperature non-uniformity and, according to Boussinesq approximation[17] is

$$f_e\left(T\right) = \beta(T) g \delta T \ \hat{z} \tag{6.13}$$

where $\beta(T)$ is the coefficient of thermal expansion of water, g is the gravitational acceleration, δT is the local temperature increase and $\hat{z}$ the vertical unit vector. Equations 6.12 and 6.13 accounts for both natural convection and thermo-osmosis.

The only unknown parameter in the calculations is χ, which is not straightforward to predict. In the present case, both glass and sapphire substrates are equivalently coated with polyelectrolytes. χ is related to the excess enthalpy h, which for an assembly of polyelectrolytes is, in principle, a complicated quantity with several contributions. A reasonable speculation is to consider that the main contributions to the enthalpy are due to surface charges in the electric double-layer. The electric double-layer enthalpy is negative, leading to positive χ and a surface flow towards the hotter region[88]. It can be estimated using the Debye-Hükel approximation[93]

$$h(z) = -\frac{1}{2}\epsilon\frac{\zeta^2}{\Lambda^2}e^{-\frac{2z}{\Lambda}} \tag{6.14}$$

where ζ is the surface z-potential, ϵ the permittivity and Λ the Debye length. Inserting 6.14 into 6.7 leads to

$$\chi = \frac{\epsilon\zeta^2}{8\mu} \tag{6.15}$$

Using $\zeta = -37$ mV for the zeta-potential of the PDDA-PSS layer[94], leads to $\chi = 1.2\ 10^{-10}\frac{\mathrm{m}}{\mathrm{s}^2}$, which is the value employed in the calculations. Thermo-osmotic flows were calculated, considering an Au 60 nm NP on glass (shown in figure 6.19a), an Au 60 nm NP on sapphire (shown in figure 6.19b) and a 150 ND on sapphire (shown in figure 6.19c). In all cases an irradiance corresponding to a Gaussian beam of $\lambda = 532$ nm and waist of $w_0 = 265$ nm centered to the NP or ND was considered, at the respective power employed in each experiment ($P = 1.2$ mW and $P = 0.5$ mW for printing on glass and sapphire, respectively).

The vector lines on figure 6.19 show the direction of the calculated flows. For Au NPs on glass, the magnitude of the flow remains high for a significant distance away from the NP. On sapphire substrates, the region of the space with appreciable velocities is reduced. For the NDs, it is confined to small volumes

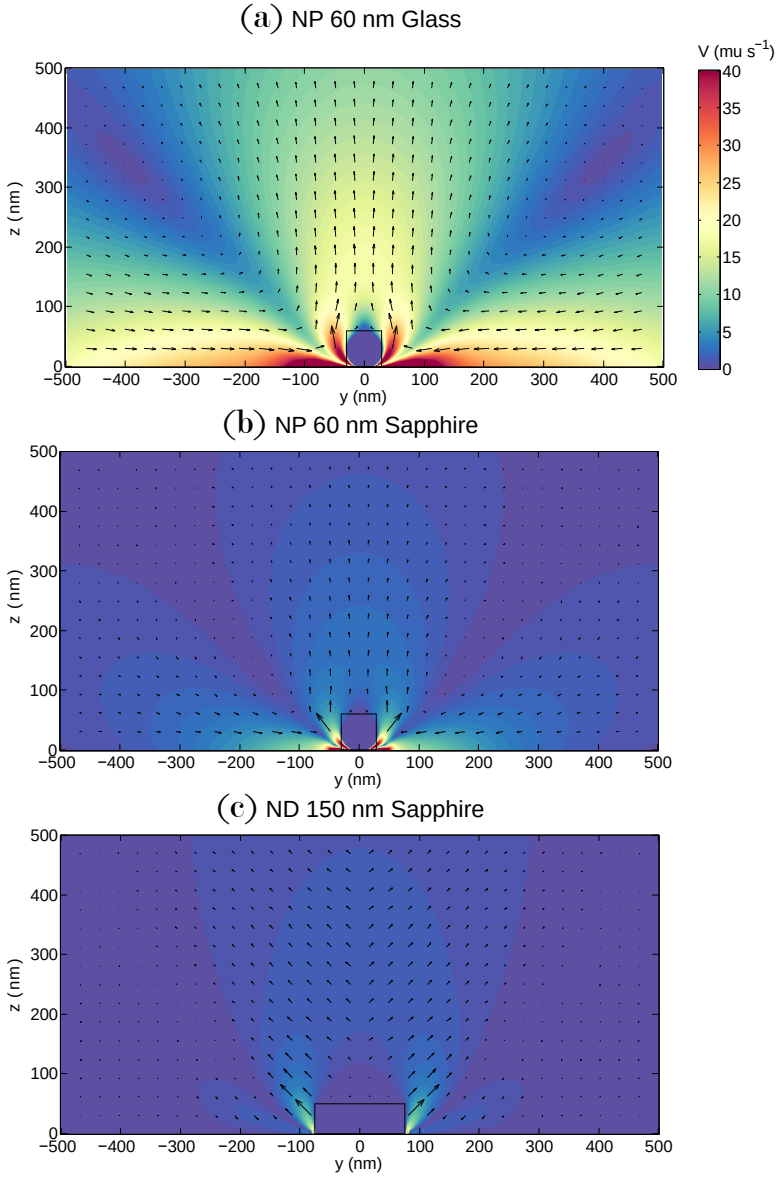

Figure 6.19: Thermo-osmotic flows induced by heating of several Au nanostructures during optical printing process. Arrows denote direction of the velocities and its magnitude is color coded. Nanostructures are in water and in the centre of a Gaussian beam at $\lambda = 532$ nm . The laser powers correspond to the ones employed on each experiment ($P = 1.2$ mW for glass and $P = 0.5$ mW for sapphire). Flows were numerically calculated by COMSOL software by Thomas Brick.

comparable to the size of the NDs. These results are qualitatively consistent with the experimental observations shown in section 6.5.2. For, example, at a point 200 nm in the y direction and 100 nm above the nanostructure, the absolute value of the induced velocity is $11\frac{\mu m}{s}$ for NPs on glass, $0.3\frac{\mu m}{s}$ for NPs on sapphire and

$0.03\frac{\mu m}{s}$ for 150 nm NDs. These velocities can be translated into drag forces using the Stokes equation (5.3). A velocity of $v_{max} \sim \frac{10\,\mu m}{s}$ correspond to a drag force of $F_{drag} \sim 10^{-3}$pN. This value is a hundred times smaller than the maximum optical force and therefore negligible. Given the linearity of the temperature and flow equations, it must be concluded that the parameter χ on equation 6.7 should be in the order of magnitude of $\chi \approx 10^{-8}\frac{m}{s^2}$ to produce drag forces comparable to their optical counterparts. With a value of χ in that order of magnitude, the drag forces would be similar to optical forces for AU NP on glass, one order weaker for AU NP on sapphire and negligible for ND on sapphire.

6.6.3 Discussion and alternative phenomena

Plasmonic heating had been identified as an important effect altering the movement of NPs in several experiments of optical manipulation [95, 96, 97, 98, 99, 100]. Discussions usually point towards convective currents induced by the hot NPs . However, efforts to quantitatively explain the observed effects in terms of natural convection have systematically failed, given their negligible magnitude.

Evidently, there is a limited current understanding of photo-thermal phenomena in the nanoscale. On the other hand, this lack of understanding did not prevent its exploitation. There have been examples where this thermal forces helped or enabled the manipulation of single[101, 102, 103] or assemblies[93] of NPs , and were identified as the driving force for the motion of self-propelled Janus particles[104, 105, 106].

Estimating theoretically the value of the thermodiffusion coefficient D_T of metallic NPs is not trivial and remains a challenging problem.[107, 108, 85]. Because of its high thermal conductivity, it has been argued that metallic NPs should not experience thermophoretic forces becausethe fluid in close vicinity of the NP is expected to have uniform temperature.[88]. However, this simplified picture could be wrong. It has been shown theoretically that thermophoretic interaction is influenced by the properties of a finite layer of fluid from the NPs surface, and actually heat conductive NPs may present higher thermophoretic coefficients than dielectric NPs. [109]. In addition, the (scarse) experimental measurements of D_T involve temperature gradients 2-3 orders of magnitude weaker than the ones present during optical printing, and temperatures near room temperature.[110, 111].

Experiments involving two mettalic NPs confined in an optical Gaussian trap

have shown that is possible to force both particles into distances as short as ten nanometers[112, 113, 114]. Those experiments could be considered as evidence against the thermophoretic repulsion. However, other reports on similar experiments, state that the trapped NPs never aggregate[65]. In addition, in a work by Feldman et. al.[115], aggregation was observed in 20% of the cases and they also report an *optothermal escape* of particles when heated inside the optical traps. The results presented in this chapter indicate that interactions due to thermophoresis could have significant magnitudes, and could be an (often forgotten) additional explanation of repulsive forces inside optical traps. In addition, in two recent papers[111, 116], thermophoresis was found to be enhanced close to surfaces due to hydrodynamic boundary effects. This means that even if the thermodiffusion coefficient D_T for metallic NPs in suspension were not as large as speculated in section 6.6.2, thermophoretic forces could still be appreciable close to surfaces.

Thermo-osmosis is an alternative or additional possible mechanism for the photo-thermal repulsion. Quantitative calculations rely on the value of the parameter χ. This parameter is related to the excess enthalpy on the boundary layer close to the surface (equation 6.7), which is not trivial to estimate theoretically. Using an electrostatic model for the enthalpy, a value of $\chi = 1.2\ 10^{-10}\frac{\mathrm{m}}{\mathrm{s}^2}$ was obtained. However, calculations of thermo-osmotic flows shown in section 6.6.2 indicate that the value of χ must be at least $\chi = 100\ 10^{-10}\frac{\mathrm{m}}{\mathrm{s}^2}$ to induce drag forces comparable to optical forces. Measured values of χ are scarse in the literature. In the work by Bregulla et.al[88], a value of $\chi = 1.8\ 10^{-10}\frac{\mathrm{m}}{\mathrm{s}^2}$ is reported for a bare glass surface in water, and $\chi = 13\ 10^{-10}\frac{\mathrm{m}}{\mathrm{s}^2}$ for a glass surface coated with Pluronic F-127 (a nonionic triblock copolymer).

An additional photo-thermal effect was recently observed by Ito et.al.[117]. Continuous wave illumination of Au NPs can lead to the formation of a stationary bubble around the NP. A Marangoni convection is induced, originating from the surface tension of stationary bubbles. Marangoni convection induces much higher convective velocities than natural convection. In their work, velocities as high as $1000\frac{\mu\mathrm{m}}{\mathrm{s}}$ were observed upon illumination of a Au 150 nm NP. However, the threshold NP temperature for bubble formation was 686 K. This value is consistent with other works, where temperature increases as high as 600 K were observed without bubble formation[78, 79, 80]. In all the experiments of this chapter, the temperature increase of the fixed particle is expected to be well

below that threshold. However, the formation of a bubble could explain the transition between the "interaction with printing" regime and the "impossible printing" regime, shown in figure 6.14.

To summarize, the results presented here contribute to the general understanding of thermophoresis and thermo-osmosis. These thermal phenomena are not well understood in the nanoscale, specially in systems under such high temperatures and large temperature gradients as the ones presented in this chapter. Reciprocally, optical printing can strongly benefit from a deeper comprehension of thermophoretic and thermo-osmosis phenomena of colloidal systems.

6.7 Connecting Au NPs on graphene substrates

In previous sections it has been proposed that the repulsion restricting the optical printing of close by NPs is caused by themophoretic forces. This forces were reduced dissipating the heat generated upon light absorption by the printed NPs employing a sapphire substrate. A route to further reduce thermophoretic forces is to employ a higher thermally conductive substrate. Absorption of such substrate must be kept as low as possible because it would lead to heating, and therefore metals are not appropriate choices. A suitable candidate is graphene. Its thermal conductivity has been claimed to be as has high as $\kappa_{graphene} = 5000\ \frac{\mathrm{W}}{\mathrm{mK}}$[118] and the absorption of a single layer is only 2.3% at $\lambda = 532$ nm[119]. In this section, optical printing on graphene substrates is described. The results are part of a collaboration with Facundo Herrera and Félix Requejo from the Instituto de Investigaciones Fisicoquímicas Teóricas y Aplicadas (INIFTA), in La Plata.

A Langmuir-Blodgett trough was used for the deposition of a graphene oxide (GO) film on a sapphire substrate. The films were formed at the air-water interface by spreading 3 ml of GO solution in methanol ($1.0\frac{\mathrm{mg}}{\mathrm{ml}}$). The temperature was kept constant at $(24 \pm 1)°C$, using a circulating water bath. Langmuir films were transferred onto silicon wafers treated with $NH_4OH : H_2O_2 : H_2O$ (1 : 1 : 5), keeping the surface pressure constant by compression. The films were then reduced in Ultra High Vacuum (UHV) at 600 °C to obtain a negativaly charged reduced graphene oxide (rGO). In this way, a surface of rGO between one and two atomic layers of thickness, homogeneously dispersed and chemically composed, was obtained with low a density of defects. An electronic conductivity as larger as

$10^5 \frac{S}{m}$ was obtained on the same rGO thin film when on silicon. The homogeneity was tested by Raman and XPS spectroscopies at different regions of the sample.

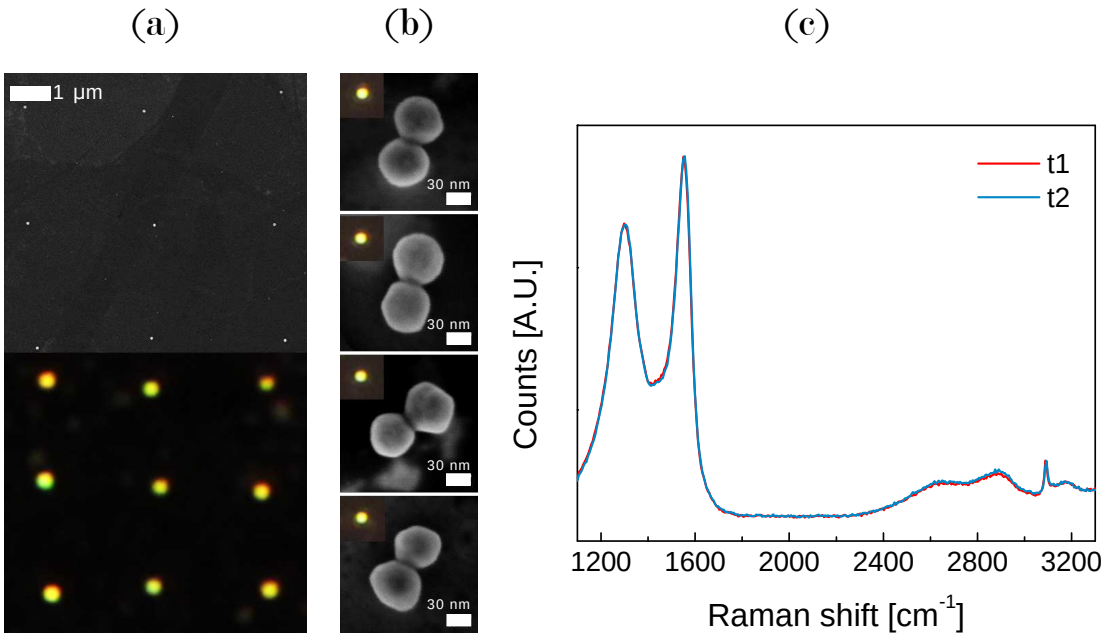

Figure 6.20: (a) Top: FE-SEM; bottom: Dark field images of a 60 nm Au NP grid optically printed on rGO; B) Dark-field and Fe-SEM images of connected Au-Au dimers printed on rGO; C) rGO Raman spectra acquired using a 532 nm laser before(red line) and after (blue line) irradiation with twice the laser power during printing. Both spectra are similar indicating that the rGO is not damaged.

Before optical printing, the rGO presence on sapphire substrates was confirmed by Raman spectroscopy, using excitation light of $\lambda = 532$ nm. Figure 6.20c shows an example spectrum. The two main peaks observed at 1600cm^{-1} and 1330cm^{-1} correspond to the G and D bands, respectively. They are the typycal peaks observed on graphene oxides. G-band is due to first-order scattering for the E2g phonon of sp2-hybridized carbon and D-band corresponds to the first-order zone boundary phonons (sp3-hybridized carbon).[120, 121]

After the acquisition of a Raman spectrum, the sample was irradiated for 2 minutes at $P = 1$ mW with a focused Gaussian beam of $\lambda = 532$ nm. Then, a second Raman spectrum was acquired. Both spectra are similar, as shown in figure 6.20c. This demonstrate that the rGO layer remains unaltered after irradiation.

A colloidal drop of Au NPs was set on top of the rGO substrate, where no

spontaneous attachment of NPs on the substrate was observed for at least 2 hours. An array of 60 nm Au NPs were printed, using resonant light of $\lambda = 532$ nm and a power of $P = 0.5$ mW. At this power, the sample is not damaged. Dark field and FE-SEM images of the printed grid shown in 6.20a proves that it is possible to print arbitrary arrays of Au particles on a rGO substrate.

Then, the possibility of printing two connected particles was studied. Several dimers with a set gap of 0 nm were printed. Even though some variations were found depending on the region of the substrate used, in many cases connected dimers could be fabricated, as shown in figure 6.20b.

It is important to note that a comparison of these results is not as straightforward. Not only was the thermal conductivity altered, but also the interfacial forces, and therefore the value of χ, could in principle be very different.

7

Light-Induced growth of optically printed Nanoparticles

In this chapter, combination of optical printing with plasmon assisted chemistry (PAC) is presented. PAC is a field of research that exploits the photophysical processes related to the excitation of localized surface plasmon resonances (LSPRs) of metallic nanoparticles (NPs) to drive chemical reactions on the nanoscale. [122, 123, 124, 125] These processes can be categorized as: i) local heating (see section1.3); ii) near-field enhancement (see section1.2); iii) plasmon-decay generated hotelectrons and hot-holes that can react with nearby molecular species. The combination of optical printing and plasmon assisted chemistry is appealing because of two main reasons. First, it makes feasible the systematic investigations of chemical reactions on immobilized single NPs, where the effect of a controlled dosage of light, including its polarization, can be studied. Second, it serves as a platform for the fabrication of devices based on NPs , where the properties of each component could be fine-tuned by plasmon assisted growth. The aim of this work is to present a novel approach to the study of the plasmon assisted synthesis of NPs at a single particle level, based on optical printing. In this chapter, plasmon-assisted growth of optically printed Au NPs is shown. Each experiment of light-induced NP growth involved essentially three steps, as depicted in figure 7.1. In the first step, a regular grid of Au NPs of 60 nm in diameter was fabricated on a glass substrate by optical printing on-resonance at $\lambda = 532$ nm and $P = 1.2$ mW, following the methods described in section 5.2. The second step was the exchange of the Au NP colloid by an aqueous solution of $HAuCl_4$, including a thorough rinsing with ultrapure water in between. Finally, each NP

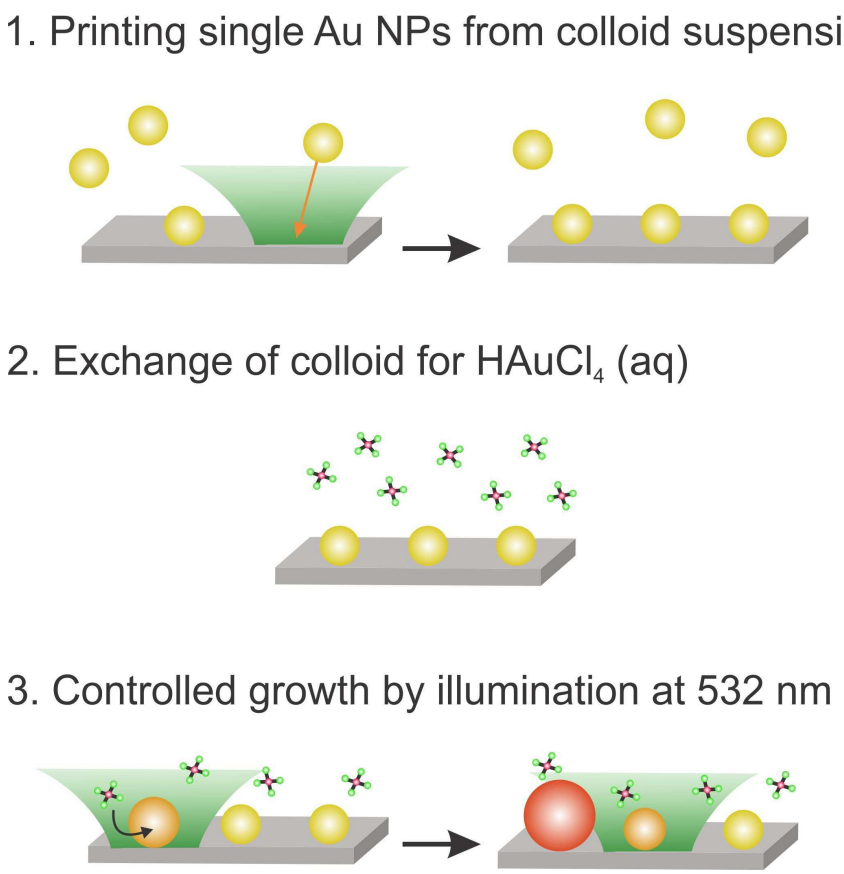

Figure 7.1: Essential steps of the light-induced growth experiment: (1) Au 60 nm NPs are optically printed from colloidal suspension; (2) the Au NPs suspension is removed and the sample chamber is rinsed thoroughly with ultrapure water and filled with an aqueous solution of $HAuCl_4$; (3) each Au NP is irradiated individually with light of 532 nm for a given time interval.

of the grid was localized by a confocal scan, moved to the center of the laser focus, and irradiated with linearly polarized light of 532 nm during a given time period.

Dark-field images of a typical grid of Au NPs are shown before (figure 7.2a) and after (figure 7.2b) a light-induced growth experiment using an irradiance of $I = 4.6 \frac{\mathrm{mW}}{\mu\mathrm{m}^2}$ of $\lambda = 532$ nm laser light and 1.5 μM $HAuCl_4$. The Au NPs on each column were irradiated for a different time interval. The controlled light-induced growth is evident already from a visual inspection of the dark-field images. As the irradiation time increases, the scattering by the NPs becomes more intense and turns from green to orange. Further insight is obtained by analysing the scattering spectra of the individual NPs . This was performed using a polarizer filter in order to separate the contributions polarized parallel (PX) and perpendicular

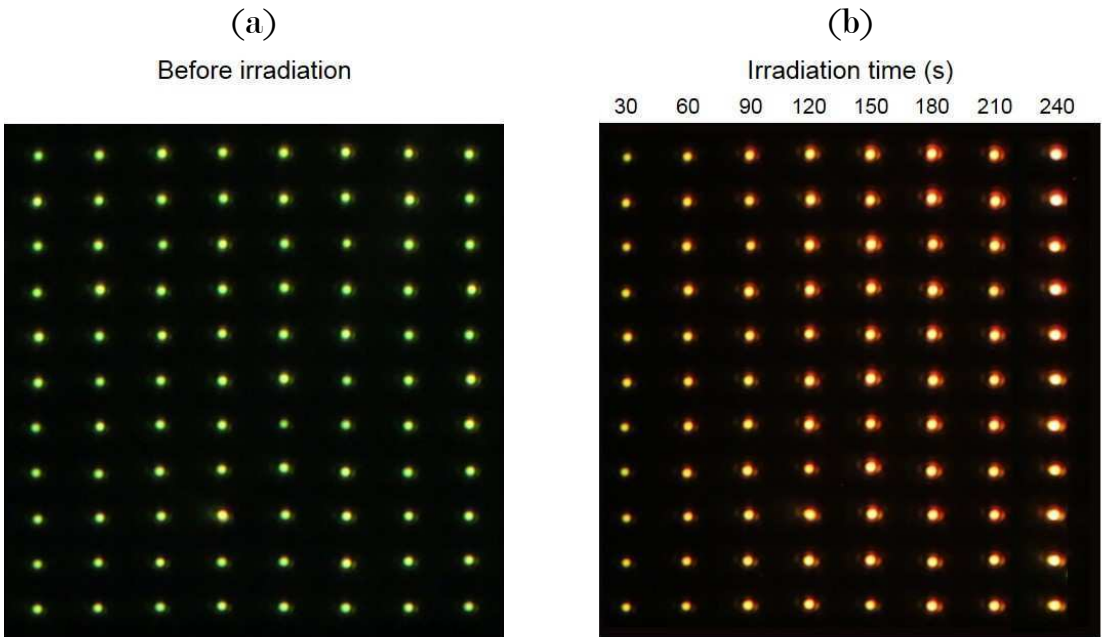

Figure 7.2: (a) Dark-field image of the optically printed Au NPs grid. (b) Dark-field image of the same grid of Au NPs after each column was irradiated with 532 nm light for different times in the presence of 1.5 μM $HAuCl_4$ (aq).

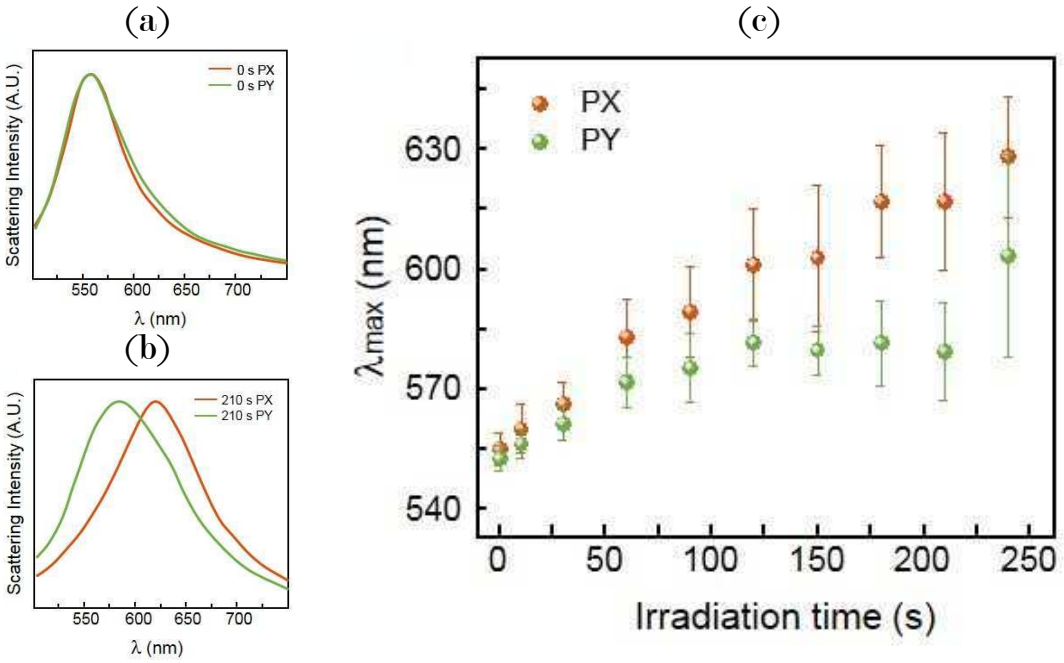

Figure 7.3: (a) Dark-field image of the optically printed Au NPs grid. (b) Dark-field image of the same grid of Au NPs after each column was irradiated with 532 nm light for different times in the presence of 1.5 μM $HAuCl_4$ (aq).

(PY) to the electric field vector used for the growth reaction. Example spectra of a NP before irradiation is shown in figure 7.3a. They correspond to the typical spectra of near spherical Au NPs , presenting a single peak at around 555 nm, independent of the polarization. Spectra of a light-grown NP after 210 s of irradiation is shown in 7.3b. Remarkably, they present different contributions depending on polarization. The scattering maximum of the PX contribution is considerably red-shifted, peaking at 620 nm. The PY spectrum with its maximum at 570 nm remains closer to the original scattering peak. Both PX and PY scattering spectra of the grown Au NPs are broader in comparison to the spectra of Au NPs before irradiation. This spectra constitute a strong indication that the light-induced growth occurred preferentially in the direction determined by the electric field of the light used for the growth reaction. In figure 7.3b, the average evolution of the PX and PY scattering peak wavelengths as a function of the irradiation time is shown. Each data point corresponds to the average obtained from 11 Au NPs. At first and up to approximately 30 s, the scattering peak wavelengths of both polarizations increase together, indicating that the growth is rather isotropic during the first stages of the reaction. Then, at around 60 s the PY peak wavelength reaches a plateau and does not increase with further irradiation, whereas the PX peak continuously shifts to longer wavelengths.

The morphology of the Au NPs was then characterized individually by field emission scanning electron microscopy (FESEM). Representative images of the Au NPs grown for different irradiation times are presented in Figure 7.4. The FE-SEM observations confirm the predictions based on the scattering spectra. Upon irradiation, the Au NPs change from nearly spherical to spheroidal with their major diameter parallel to the polarization of the light used for the growth reaction.

Control experiments were performed. The printed Au NPs were left in contact with 1.5 μM $HAuCl_4$for several days with no irradiation. Then, they were visualized using a field-emission scanning electron microscopy (FE-SEM). No changes were observed, as shown in figure 7.4b. On a complementary experiment, the NPs were illuminated with twice the irradiance used for the growth reaction ($I = 9.2\frac{\mathrm{mW}}{\mu\mathrm{m}^2}$), with no observed changes either, as shown in figure 7.4c.

In order to further quantify the evolution of the reshaping, the FE-SEM images of all single Au NPs were analysed, identifying their minor and major diameters, and determining the angle φ between them, acording to the definition given on

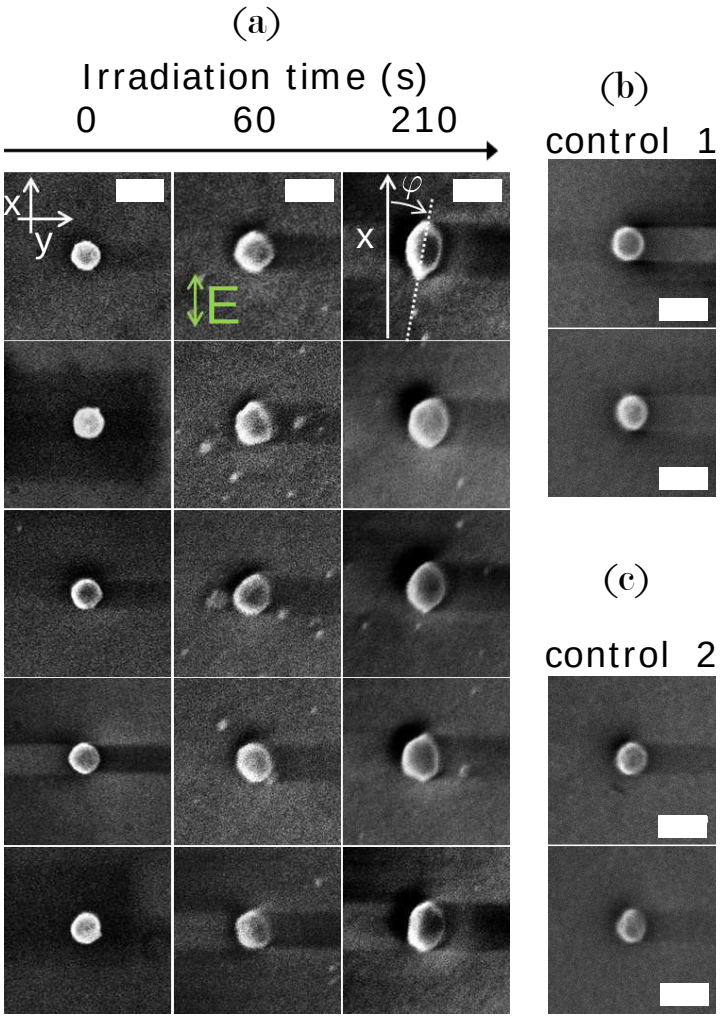

Figure 7.4: FE-SEM images of five representative Au NPs in the presence of $HAuCl_4$without irradiation (0 s) and irradiated for 60 and 210 s using a $\lambda = 532$ nm laser beam with an irradiance of $I = 4.6\frac{\text{mW}}{\mu\text{m}^2}$. The electric field polarization vector E, angle description φ, and axis references are also indicated. (b) Control experiment. Au NPs in contact with 1.5 μM $HAuCl_4$for several days but without irradiation. (c) Control experiment. Au NPs irradiated with $\lambda = 532$ nm laser light for 60 s in the absence of $HAuCl_4$, at twice the irradiance used for the growth reaction ($I = 9.2\frac{\text{mW}}{\mu\text{m}^2}$)

figure 7.4a). Figure 7.5a shows the average minor and major diameters of the Au NPs as a function of the irradiation time, and 7.5b shows the average angle φ. The Au NPs increase their size, first in a rather isotropic way and then faster in the direction imposed by the electric field. The directionality imposed by the polarization of light is evident as well in the reduced dispersion of φ as the light-induced growth reaction progresses. At short irradiation times, values of φ

spanning a range of almost 90° are observed, reflecting the fact that the Au NPs are nearly spherical without any preferential orientation. As the growth reaction advances, φ takes values over a much narrower range of less than $\pm 10°$, indicating the Au NPs have grown preferentially in the direction imposed by polarization.

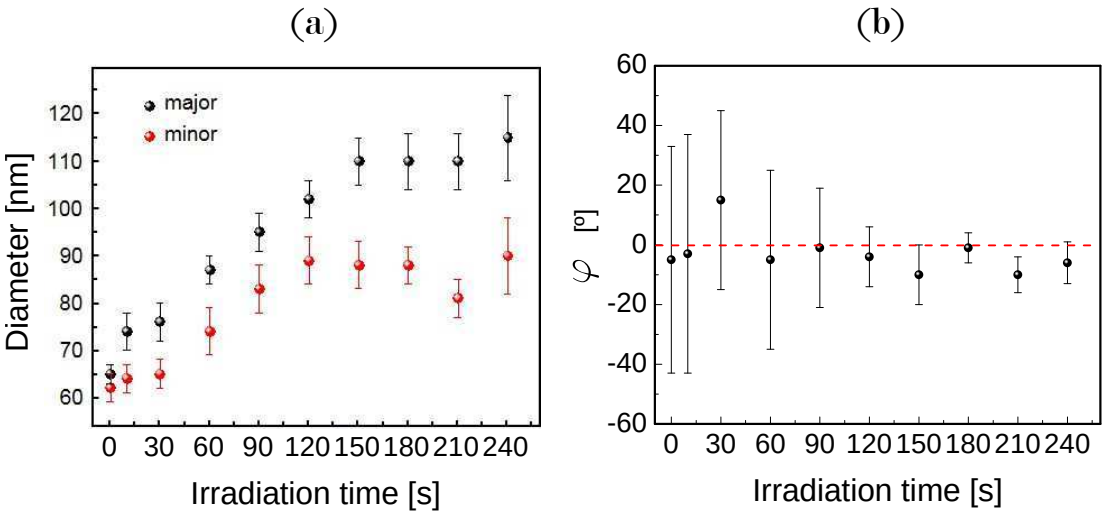

Figure 7.5: (a) Major and minor diameter dependence on the irradiation time using linearly polarized light along X. (b) Angle obtained between X and the major axis of the NPs φ versus irradiation time.

The mechanistic details of light-induced growth of metallic NPs are not trivial and are still a matter of investigation and debate, even after more than a decade since its discovery with silver NPs[123, 126]. Light-induced growth of gold NPs has only recently been reported in a detailed study, using various reducing agents and polyvinylpyrrolidone (PVP) as surface capping[127]. Currently, the proposed mechanism[128] involves the following steps. Upon illumination, hot electron-hole pairs are generated in the metallic NP, preferentially in regions of enhanced electric field (hot-spots) determined by the particular plasmon mode excited. Such hot electron-hole pairs have a lifetime of the order of femtoseconds[129] and therefore are too short-lived to directly drive the reduction reaction of metal ions in solution. Instead, it is proposed that molecules at the NP surface can act as electron donors to fill the photogenerated holes, rendering the NPs with a net negative charge, which has been measured consistently.[130, 126] Then, metallic ions from the solution that get in contact with the NPs are reduced and incorporated one by one to the glsNP, leading to growth with crystalline order. A reductive agent present in the solution, usually citrate, closes the redox cycle. The final NP shape is independent of the positions of the plasmonic hotspots

obtained by varying the incident-light polarization[126] or wavelength,[127] which is in contrast the findings presented here.

The results of this chapter, however, are conducted under different conditions from most previous reports. Although the Au NPs had a surface layer of citrate anions, no extra citrate or any other reducing agent was present in the solution; that is, the redox cycle is probably closed by water oxidation.[131, 132] In addition, the employed irradiances that are 10^9 times higher than what has been typically used. These conditions in turn modify several critical experimental parameters: (i) much more intense near fields are generated, (ii) the Au NP surface and the solution around are at temperatures considerably higher than room temperature during the growth reaction. The estimated surface temperature increase of the NP is 265°K, according to equation 6.5, (iii) reaction rates are higher in comparison to previous reports (4 min versus hours), even when the reducing agent is weaker. There are few examples of experiments conducted in comparable conditions.[133, 134]Also, Kim et al.[132] recently described the reduction of aqueous platinum ions onto Au NPs observing a preferential deposition in the NPs hot spots, in agreement with the findings presented here.

From the FE-SEM images, it is evident that the Au NPs do not grow following any crystallographic order, which is consistent with the fast growing rates[135] and the absence of surface molecules with preferential selectivity to crystallographic planes (such as PVP). The anisotropic growth must have a different origin. Other interesting fact observed on the Fe-SEM images, was that in some

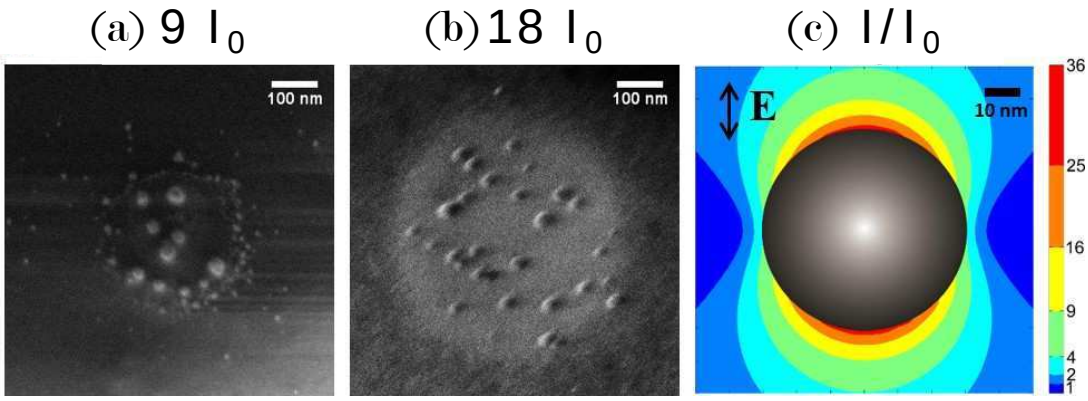

Figure 7.6: FE-SEM images of Au NPs formed directly on the substrate, irradiating in the presence of $HAuCl_4$at: (a) 9 I_0, (a) 18 I_0 (c) Map of the near field intensity. $I_0 = 4.6\frac{\text{mW}}{\mu\text{m}^2}$ is the irradiance used in the growth experiments.

cases, smaller Au NPs (5-15 nm) appeared on the irradiated area near the printed

Au NPs (e.g., figure 7.4a at 60 and 210 s). For the longest exposure time, the amount of these satellite NPs was considerable. Scattering by these NPs is most probably the reason why the points at 240 s in Figure 2E deviate from the trend. On the basis of these observations, an additional experiment was performed. Regions of the substrate that were far from any Au NP were irradiated. Using the same irradiance as for the NP growth produced no effect whatsoever. However, by using irradiances 9-to 18-fold higher ($I = 41 - 80 \frac{\mathrm{mW}}{\mu \mathrm{m}^2}$), smaller Au NPs deposited and grew on any region of the substrate, as shown on figures 7.6a and 7.6b. Noting that both the substrate and the HAuCl4 solution are practically transparent at 532 nm, it is reasonable to speculate that small Au clusters form and disassemble in a dynamic equilibrium. Au clusters of a few tens of atoms present broad visible absorption.[136] NPs as small as 2.9 nm in diameter ($\approx$ 700 atoms) already sustain a surface plasmon resonance and absorb resonant light of 532 nm. Such spontaneously formed clusters are the ones interacting with light and driving the reaction. The high levels of irradiance needed for these clusters to drive the reduction of $HAuCl_4$ are comparable to what is expected near the poles of the immobilized 60 nm (and larger) Au NPs when they are plasmonically excited with polarized light, as shown in figure 7.6c. Therefore, a reasonable interpretation of the observed results is that the anisotropic NP growth induced by the polarization of light occurs via small Au clusters present in the solution, which grow preferentially in the regions of highly intensified plasmon fields at the Au NP poles determined by the direction of polarization.

In addition to the photoinduced reduction, other physical phenomena are plausible to play a role. As soon as a small but polarizable Au NP forms near the pole of the immobilized AuNP, it would be attracted to the larger NP due to optically induced dipole-dipole interaction. The high temperature due to light absorption would then stimulate coalescence.[134] This temperature increase does not play a dominant role in the reaction growth. Because the temperature of the Au NPs is homogeneous over its surface, a thermally induced reaction would lead to isotropic and polarization independent growth, which is in contrast to the observations. Moreover, melting or reshaping of the NPs due to the light-induced heating can be ruled out considering the temperatures reached. This is further proved by the control experiment shown in figure 7.4c where printed Au NPs are irradiated in water but in the absence of gold precursor, and no changes in shape or size are observed.

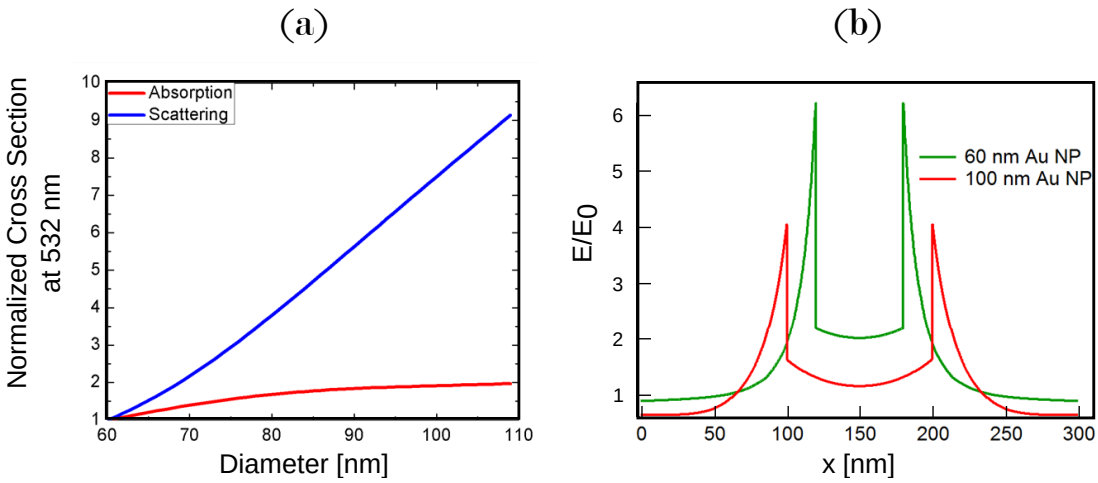

Figure 7.7: (a) Absorption and scattering cross sections at 532 nm for Au NPs with diameters from 60 to 110 nm, calculated with Mie theory (1.12 and 1.11), normalized to their value for 60 nm NPs . (b) Electric field profiles, normalized to the incident field (E_0) as a function of position along the direction of polarization, for Au NPs of 60 and 100 nm in diameter, when they are illuminated at 532 nm.

As the Au NPs grow, their surface plasmon resonance shifts away from the 532 nm laser. This is a plausible reason for the growth reaction to slow down and eventually stop at a given final size. Figure 7.7a shows the evolution of the absorption and scattering cross sections at 532 nm as a function of the Au NP diameter. The scattering cross section increases almost linearly, and the absorption cross section remains fairly constant, as the NP diameter increases from 60 to 110 nm. This shows that the plasmon shift is not sufficient to leave the 532 nm laser completely out of resonance. However, the maximum near field as a function of the NP diameter does decrease as the Au NPs grow. The scattering cross section increases linearly with the diameter but the NP surface increases quadratically. The total field enhancement distributes over a larger area and the maximum field achieved is lower. Figure 7.7b shows field profiles along the direction of polarization for 60 and 100 nm Au NPs. Therefore, it is plausible that the grow reaction stops due to the surface plasmon shifts away from the laser, if the maximum near field intensity becomes insufficient to drive the plasmon induced reaction with the small Au clusters.

8

Conclusions

Optical printing is a recently introduced technique that allows the direct assembly of colloidal nanoparticles (NPs) , one by one, onto solid surfaces with great flexibility of pattern design and no need of any previous surface patterning.

In this thesis, an experimental set-up for optical printing at different wavelengths was built, including a software set for its full control. The set-up made possible the automated optical printing of Au and Ag NPs on arbitrary arrays, the on-live monitoring of the printing process and the optical characterization of the fabricated arrays. The full automation and high mechanical stability of the set-up enabled systematic investigations of fundamental open questions of optical printing.

Achieving high accuracy in the positioning of NPs onto surfaces is one of the open challenges of current nanotechnology and of optical printing in particular. Here, the precision of optical printing to immobilize a single NP in a target position was studied, as a function of various experimental parameters, such as the power and wavelength of the printing beam and for Au and Ag NPs . These two materials are of particular interest because of their extended use in research and technology. For both materials, two different regimes were identified depending on whether the laser used is tuned to the LSPR (on-resonance) or not. For light on-resonance, optical printing provides higher precision at lower powers, up to a limit where printing is not possible because the optical forces are not strong enough to surpass the electrostatic repulsion by the substrate. On the other hand, if light off-resonance is used, the precision is worse than the best precision attained on-resonance, but is practically independent of the laser power. A detailed physical description of the process of optical printing of NPs was pro-

vided, including the analytical calculation of optical forces, Brownian motion and surface repulsion. The developed model was able to quantitatively explain the main aspects of the experimental observations. These investigations expand the understanding of the processes behind optical printing and constitute a useful guideline for future applications.
In spite of its practicality and high potential, optical printing had been limited to the fabrication of patterns of well separated NPs. For unknown reasons, it was not possible to print NPs closer than 300 nm in a controlled manner. The nature of the repulsion causing this limitation was unclear. In this thesis, the optical printing of two NPs at controlled separation distances was studied. First, it was shown that interaction of the printing beam with the already fixed NPs disrupts the printing process of a second NP. Selecting a wavelength for which the printed NPs were practically transparent, it was possible to fabricate Ag-Au NP heterodimers at any inter-particle separation, as well as connected dimers with controlled orientation. This important achievement constitutes the first step towards the fabrication of circuits of connected colloidal NPs by optical printing. Based on the experimental observations, many plausible mechanisms for the light induced repulsion were evaluated by means of physical arguments and calculations. It was concluded that the repulsion restricting the optical printing of close by NPs is due to absorbed light and consequent heating of the printed NPs . Other mechanisms based on light scattering were firmly ruled out. As a first solution to print identical NPs closer to each other, heat dissipation was enhanced by using substrates with higher thermal conductivity. Enlarging the contact area between the fixed particles and the substrate was shown to be a viable possibility as well. Optical printing of Au-Au homodimers with gaps below the 100 nm could be fabricated by optical printing. Then, as a proof of concept, optical printing of Au connected NPs was demonstrated on highly thermal conductive graphene substrates.

Photo-thermal effects, in spite of being identified as important phenomena hindering the performance of several experiments of optical manipulation of nano components, are not well understood at the nanoscale. In the context of optical printing, thermophoresis and thermo-osmosis were discussed. The results presented here contribute to the general understanding of these intriguing phenomena, at sub-micrometer length scales and high temperature gradients, and therefore their impact exceeds the field of optical printing. Reciprocally, it is

envisioned that the technique can strongly benefit from a deeper comprehension of thermophoretic and thermo-osmosis phenomena of colloidal systems.

Finally, spherical Au NPs immobilized by optical printing were grown to definite sizes, one by one, by driving photochemical reactions locally with the enhanced near-field around the printed NPs. Conditions were found for which the photo-induced growth is faster in the direction imposed by the polarization of light, leading to spheroidal NPs of predetermined orientation. Apart from the interest in the particular studied reaction, the general use of optical printing as a general platform for systematic investigations of plasmon-assisted chemical reactions performed on supported metallic NPs was introduced. It facilitates the systematic investigations of chemical reactions on immobilized single NPs, where the effect of a controlled dosage of light, including the elusive role of light polarization, can be studied.

The results presented on this thesis expand the field of application of optical printing as a template-free and versatile nanofabrication strategy for positioning colloidal NPs on a solid surface. They constitute the fundamental step for the fabrication of complex functional nanostructures and circuits based on connected NPs. The new insight into the physical mechanism of optical printing provides clear guidelines for devising new, optimized optical printing strategies fulfilling the key condition of avoiding temperature increases of the printed NPs, either by avoiding absorption or by efficiently dissipating the generating heat. In addition, controlled and in-situ anisotropic shaping of printed NPs in particular directions is possible, further expanding the versatility of nanostructures that can be built.

Agradecimientos

Fernando es un excelente director al que le estoy agradecido por muchos motivos. Me dio la oportunidad de trabajar en un tema interesante. Se ocupó de que no falten los equipos y condiciones necesarios para hacer los experimentos. Fue un director presente, que respondió siempre que lo necesité y me dedicó mucho tiempo, sin importar si era fin de semana o vacaciones. Aprendí desde el primer día hasta la última corrección de esta tesis. Hizo posible que pueda discutir mi trabajo con referentes mundiales en el tema. Le agradezco mucho.

Le agradezco a Andrea, que además de ser mi consejera de estudios fue con quien comencé este camino en la nanoescala.

Me tocó hacer el doctorado en un momento en que el sistema científico argentino se estaba construyendo, simbólica y literalmente. Fui un privilegiado en poder colaborar con el armado del Polo Científico y Tecnológico. Le agradezco al estado argentino por la oportunidad. Hoy que el gobierno de Cambiemos desprestigia, recorta y destruye al sistema científico, agradezco a todos los que luchan para defender lo contruido.

Fue un orgullo haber sido parte del grupo fundacional del CIBION. Le agradezco a Pedro por realizar la díficil y admirable tarea de dirigirlo. También por los consejos y las recomendaciones.

La ciencia es evaluada en términos individuales pero se hace colectivamente. Tuve tres equipos de trabajo intenso. Esta tesis tiene mi nombre pero la hicimos entre los cuatro. Primero con Emiliano, un año con Santiago y al final con Ianina. Fueron mis maestros, porque se aprende haciendo e hicimos ciencia juntos.

Durante tres días intensos en Brno y muchos skypes, Luke también fue un compañero de ciencia. Gracias Luke por sacar a pasear al extranjero. Gracias a Pavel por la hospitalidad.

A Tom, Toshi y Pablo. Por hacer el esfuerzo de entenderme. Porque disfruté de trabajar juntos. A Stefan por darme la posibilidad de que suceda. Gracias.

Emi me ayudó muchisimo, Estando acá me dio confianza en momentos difíciles y me contagió su pasión por la ciencia (de la que Santi dice haberse contagiado después). Discutimos durante madrugadas o andando en bici. Después me bancó tres semanas en la casa para que podamos laburar juntos. Gracias a Eva por eso también.

Iani me enseñó a poner la vara alta en la calidad de los datos mientras me ayudaba con minusciosidad y detalle a alcanzar esa vara. También me escuchó, ordenó y enfoncó. Y hasta me prestó su computadora un fin de semana para que avance con la escritura de la tesis cuando la mía se rompió. Gracias Iani

El mejor compañero de laboratorio posible es Fede. El mundo sería un lugar mejor si todos fueramos como él. Le agradezco por todas las veces en que su prioridad fueron los intereses del grupo y no los suyos. Su trabajo (a veces invisible) me ayudó muchisimo. Lo quiero, lo admiro y le agradezco.

En los primeros años me hubiera vuelto loco si no fuera por Jesica, que me enseñó a no tomar las cosas tan en serio. Fue para mí una referente y le agradezco infinito.

A Francisco por ayudarme en mis primeros pasos, cuando andaba muy perdido. Por dedicarme tiempo que no tenía. Fue decisivo para el desarollo del programa del microscopio.

Caldarola también fue clave para ayudarme a arrancar. Siempre apasionado. Gracias.

A Maxi, porque gracias a su pericia el microscopio funcionó.

A Freitas, Marian, PP y Mundel por convivir con esta locura. A Gabi por cada vez que golpeó la puerta de Giribone.

A Fede, Ari, Mario y Sabri por compartir la vorágine de la escritura y por contenerme.

A todo es-importante por el aguante.

A la gente del CIBION que compartió conmigo estos años. Andy, Leo, Cata, Pablo, Lucho, Anto, Chechu, Nati, Luciana, Santi, Walter, Sabri, Bruno, Helen, Migue, Ale, Emi, Borde, Nico y Ana.

Gracias Alan por compartir el caos.

A Lucho por el buen humor y las charlas de ciencia.

A Mark por los consejos y recomendaciones.

Le agradezco a todo el que alguna vez no le acepté alguna invitación porque tenía que trabajar en esta tesis. Al entenderme me apoyaron.

A mis amigos y amigas. Gabi, Marian, PP, Freitas, Fede, Mario, Monti, Ari, Sabri. Con todos tuve al menos una mañana, tarde, noche o madrugada crucial.

A Dalia, Ricardo, Laura y Freya. Para dejar por escrito que los quiero y les agradezco por ser parte de mi vida.

A mi mamá y mi papá, de quienes surgió el placer de razonar el mundo, la filosofía y la ciencia. Por el infinito apoyo.

Los cinco años incluyeron fuertes miedos, angustias, incertidumbres, euforias, festejos, llantos, alegrías. Con ella los compartí. Fui alentado, consolado, aconsejado y soportado. Mientras repaso esos recuerdos me emociono, y desbordo de agradecimiento y amor por Alina.

Glossary

CDF	cumulative distribution function 66, 67, 69
GO	graphene oxide 114
LSPR	localized surface plasmon resonance 12, 14–16, 18, 19, 21, 25, 37, 42, 68, 117
MNP	metallic nanoparticle 41, 42, 50, 52, 57, 62, 64
ND	nanodisk 99–101, 110, 111
NP	nanoparticle 11–15, 18, 20–22, 27, 35–37, 39–41, 44, 46, 47, 51, 58–84, 86–89, 91, 92, 95–101, 103, 109, 110, 112–120, 122, 124–127
PAC	plasmon assisted chemistry 117
PDDA	Polydiallyldimethylammonium chloride 62
PSS	sodium polystyrene sulfonate 62
rGO	reduced graphene oxide 114–116
RMSE	Root mean square error 66
UHV	Ultra High Vacuum 114

Bibliography

[1] M.-C. Daniel and D. Astruc, "Gold nanoparticles:assembly, supramolecular chemistry, quantum-size-related properties, and applications toward biology, catalysis, and nanotechnology," *Chemical Reviews*, vol. 104, 01 2004.

[2] T. Hyeon, "Chemical synthesis of magnetic nanoparticles," *Chemical Communications*, 4 2003.

[3] O. Masala and R. Seshadri, "Synthesis routes for large volumes of nanoparticles," *Annual Review of Materials Research*, vol. 34, 2004.

[4] C. J. Murphy, T. K. Sau, A. M. Gole, C. J. Orendorff, J. Gao, L. Gou, S. E. Hunyadi, and T. Li, "Anisotropic metal nanoparticles: Synthesis, assembly, and optical applications," *ChemInform*, vol. 36, 2005.

[5] T. K. Sau, A. L. Rogach, F. Jäckel, T. A. Klar, and J. Feldmann, "Properties and applications of colloidal nonspherical noble metal nanoparticles," *Advanced Materials*, vol. 22, 2010.

[6] A. R. Tao, S. Habas, and P. Yang, "Shape control of colloidal metal nanocrystals," *Small*, vol. 4, 2008.

[7] R. Ghosh Chaudhuri and S. Paria, "Core/shell nanoparticles: Classes, properties, synthesis mechanisms, characterization, and applications," *Chemical Reviews*, vol. 112, 2012.

[8] Xia, Xiong, Lim, and Skrabalak, "Shape controlled synthesis of metal nanocrystals: Simple chemistry meets complex physics?," *Angewandte Chemie International Edition*, vol. 48, 2009.

[9] R. A. Sperling and W. J. Parak, "Surface modification, functionalization and bioconjugation of colloidal inorganic nanoparticles," *Philosophical Transactions Mathematical Physical & Engineering Sciences*, vol. 368, 2010.

[10] P. Paufler, "M. n. rudden, j. wilson. elements of solid state physics. john wiley and sons, chichester, 2nd edition 1993. isbn 0-471-92973-5. 264 seiten. preis £ 15.95 (paperback)," *Crystal Research and Technology*, vol. 28, 1993.

[11] S. Maier, *Plasmonics: Fundamentals and Applications*. Springer US, 2010.

[12] J. D. Jackson, *Classical electrodynamics*. New York, NY: Wiley, 3rd ed. ed., 1999.

[13] G. C. Coronado, Eduardo A.; Schatz, "Surface plasmon broadening for arbitrary shape nanoparticles: A geometrical probability approach," *The Journal of Chemical Physics*, vol. 119, 2003.

[14] C. F. Bohren and D. R. Huffman, *Absorption and Scattering of Light by Small Particles*. 1998.

[15] H. Kuwata, H. Tamaru, K. Esumi, and K. Miyano, "Resonant light scattering from metal nanoparticles: Practical analysis beyond rayleigh approximation," *Applied Physics Letters*, vol. 83, 2003.

[16] G. Baffou and R. Quidant, "Thermo-plasmonics: using metallic nanostructures as nano-sources of heat," *Laser & Photonics Reviews*, vol. aop, 2012.

[17] J. S. Donner, G. Baffou, D. McCloskey, and R. Quidant, "Plasmon-assisted optofluidics," *ACS Nano*, vol. 5, 07 2011.

[18] M. Dienerowitz, "Optical manipulation of nanoparticles: a review," *Journal of Nanophotonics*, vol. 2, 09 2008.

[19] O. M. Maragò, P. H. Jones, P. G. Gucciardi, G. Volpe, and A. C. Ferrari, "Optical trapping and manipulation of nanostructures," *Nature Nanotechnology*, vol. 8, no. 11, pp. 807–819, 2013.

[20] S. Albaladejo, M. I. Marqués, M. Laroche, and J. J. Sáenz, "Scattering forces from the curl of the spin angular momentum of a light field," *Phys. Rev. Lett.*, vol. 102, p. 113602, Mar 2009.

[21] R. R. Agayan, F. Gittes, R. Kopelman, and C. F. Schmidt, "Optical trapping near resonance absorption.," *Applied optics*, vol. 41, no. 12, pp. 2318–2327, 2002.

[22] N. Vogel, M. Retsch, C.-A. Fustin, A. del Campo, and U. Jonas, "Advances in colloidal assembly: The design of structure and hierarchy in two and three dimensions," *Chemical Reviews*, vol. 115, 07 2015.

[23] N. Vogel, C. K. Weiss, and K. Landfester, "From soft to hard: the generation of functional and complex colloidal monolayers for nanolithography," *Soft Matter*, vol. 8, pp. 4044–4061, 2012.

[24] O. D. Velev and S. Gupta, "Materials fabricated by micro- and nanoparticle assembly – the challenging path from science to engineering," *Advanced Materials*, vol. 21, no. 19, pp. 1897–1905, 2009.

[25] Q. Li, U. Jonas, X. S. Zhao, and M. Kappl, "The forces at work in colloidal self-assembly: a review on fundamental interactions between colloidal particles," *Asia-Pacific Journal of Chemical Engineering*, vol. 3, no. 3, pp. 255–268, 2008.

[26] N. A. Fleck, R. M. McMeeking, and T. Kraus, "Convective assembly of a particle monolayer," *Langmuir*, vol. 31, 12 2015.

[27] L. Malaquin, T. Kraus, H. Schmid, E. Delamarche, and H. Wolf, "Controlled particle placement through convective and capillary assembly," *Langmuir*, vol. 23, no. 23, pp. 11513–11521, 2007. PMID: 17910483.

[28] N. Vogel, S. Goerres, K. Landfester, and C. K. Weiss, "A convenient method to produce close- and non-close-packed monolayers using direct assembly at the air–water interface and subsequent plasma-induced size reduction," *Macromolecular Chemistry and Physics*, vol. 212, 2011.

[29] M. Retsch, M. Tamm, N. Bocchio, N. Horn, R. Förch, U. Jonas, and M. Kreiter, "Parallel preparation of densely packed arrays of 150-nm gold-nanocrescent resonators in three dimensions," *Small*, vol. 5, 2009.

[30] A. Plettl, F. Enderle, M. Saitner, A. Manzke, C. Pfahler, S. Wiedemann, and P. Ziemann, "Non-close-packed crystals from self-assembled polystyrene spheres by isotropic plasma etching: Adding flexibility to colloid lithography," *Advanced Functional Materials*, vol. 19, 2009.

[31] A. Manzke, N. Vogel, C. K. Weiss, U. Ziener, A. Plettl, K. Landfester, and P. Ziemann, "Arrays of size and distance controlled platinum nanoparticles fabricated by a colloidal method," *Nanoscale*, vol. 3, 2011.

[32] K. Nakahama and K. Fujimoto, "Thermosensitive two-dimensional arrays of hydrogel particles," *Langmuir*, vol. 18, 12 2002.

[33] Y. Lu and M. Drechsler, "Charge-induced self-assembly of 2-dimensional thermosensitive microgel particle patterns," *Langmuir*, vol. 25, 11 2009.

[34] N. Vogel, C. Fernández-López, J. Pérez-Juste, L. M. Liz-Marzán, K. Landfester, and C. K. Weiss, "Ordered arrays of gold nanostructures from interfacially assembled au@pnipam hybrid nanoparticles," *Langmuir*, vol. 28, 06 2012.

[35] S. Jaber, M. Karg, A. Morfa, and P. Mulvaney, "2d assembly of gold–pnipam core–shell nanocrystals," *Physical Chemistry Chemical Physics*, vol. 13, 2011.

[36] X. Li, T. Wang, J. Zhang, X. Yan, X. Zhang, D. Zhu, W. Li, X. Zhang, and B. Yang, "Modulating two-dimensional non-close-packed colloidal crystal arrays by deformable soft lithography," *Langmuir*, vol. 26, 02 2010.

[37] X. Yan, J. Yao, G. Lu, X. Li, J. Zhang, K. Han, and B. Yang, "Fabrication of non-close-packed arrays of colloidal spheres by soft lithography," *Journal of the American Chemical Society*, vol. 127, no. 21, pp. 7688–7689, 2005. PMID: 15913353.

[38] Y. Yin, Y. Lu, B. Gates, and Y. Xia, "Template assisted self-assembly: A practical route to complex aggregates of monodispersed colloids with well-defined sizes, shapes, and structures," *Journal of the American Chemical Society*, vol. 123, no. 36, pp. 8718–8729, 2001. PMID: 11535076.

[39] V. Flauraud, M. Mastrangeli, G. D. Bernasconi, J. Butet, D. T. L. Alexander, E. Shahrabi, O. J. F. Martin, and J. Brugger, "Nanoscale topographical control of capillary assembly of nanoparticles," *Nature Nanotechnology*, 10 2016.

[40] I. Lee, H. Zheng, M. Rubner, and P. Hammond, "Controlled cluster size in patterned particle arrays via directed adsorption on confined surfaces," *Advanced Materials*, vol. 14, 2002.

[41] K. M. Chen, X. Jiang, L. C. Kimerling, and P. T. Hammond, "Selective self-organization of colloids on patterned polyelectrolyte templates," *Langmuir*, vol. 16, 10 2000.

[42] F. Fan and K. J. Stebe, "Assembly of colloidal particles by evaporation on surfaces with patterned hydrophobicity," *Langmuir*, vol. 20, 04 2004.

[43] H. Wang, Y.-l. Zhang, H. Xia, q. chen, K.-S. Lee, and H. Sun, "Photodynamic assembly of nanoparticles towards designable patterning," *Nanoscale Horizons*, 2016.

[44] J. P. Hoogenboom, D. L. J. Vossen, C. Faivre-Moskalenko, M. Dogterom, and A. van Blaaderen, "Patterning surfaces with colloidal particles using optical tweezers," *Applied Physics Letters*, vol. 80, 2002.

[45] S. Ito, H. Yoshikawa, and H. Masuhara, "Laser manipulation and fixation of single gold nanoparticles in solution at room temperature," *Applied Physics Letters*, vol. 80, 2002.

[46] S.-W. Lee, G. Jo, T. Lee, and Y.-G. Lee, "Controlled assembly of in2o3 nanowires on electronic circuits using scanning optical tweezers," *Optics Express*, vol. 17, 2009.

[47] M. J. Guffey and N. F. Scherer, "All-optical patterning of au nanoparticles on surfaces using optical traps," *Nano Letters*, vol. 10, 11 2010.

[48] A. S. Urban, A. a. Lutich, F. D. Stefani, and J. Feldmann, "Laser Printing Single Gold Nanoparticles," *Nano Letters*, vol. 10, no. 12, pp. 4794–4798, 2010.

[49] L. Lin, X. Peng, Z. Mao, W. Li, M. N. Yogeesh, B. B. Rajeeva, E. P. Perillo, A. K. Dunn, D. Akinwande, and Y. Zheng, "Bubble-pen lithography," *Nano Letters*, 12 2015.

[50] P. Y. Chiou, A. T. Ohta, and M. C. Wu, "Massively parallel manipulation of single cells and microparticles using optical images," *Nature*, vol. 436, 2005.

[51] G. Decher, "Fuzzy nanoassemblies: Toward layered polymeric multicomposites," *Science*, vol. 277, 1997.

[52] J. N. Israelachvili, *Intermolecular and surface forces*. Colloid Science, Academic Press, 2 ed., 1992.

[53] R. Bos, H. C. van der Mei, and H. J. Busscher, "Physico-chemistry of initial microbial adhesive interactions – its mechanisms and methods for study," *FEMS Microbiology Reviews*, vol. 23, 1999.

[54] M. J. Guffey, R. L. Miller, S. K. Gray, and N. F. Scherer, "Plasmon-driven selective deposition of au bipyramidal nanoparticles," *Nano Letters*, vol. 11, no. 10, pp. 4058–4066, 2011.

[55] M. A. Huergo, C. M. Maier, M. F. Castez, C. Vericat, R. C. Salvarezza, A. S. Urban, and J. Feldmann, "Optical nanoparticle sorting elucidates synthesis of plasmonic nanotriangles," *ACS Nano*, 02 2016.

[56] S. Nedev, A. S. Urban, A. a. Lutich, and J. Feldmann, "Optical force stamping lithography," *Nano Letters*, vol. 11, no. 11, pp. 5066–5070, 2011.

[57] Y. Bao, Z. Yan, and N. F. Scherer, "Optical Printing of Electrodynamically Coupled Metallic Nanoparticle Arrays," *The Journal of Physical Chemistry C*, p. 140728101029000, 2014.

[58] L. Ling, H.-L. Guo, X.-L. Zhong, L. Huang, J.-F. Li, L. Gan, and Z.-Y. Li, "Manipulation of gold nanorods with dual-optical tweezers for surface plasmon resonance control," *Nanotechnology*, vol. 23, 2012.

[59] J. Do, M. Fedoruk, F. Jäckel, and J. Feldmann, "Two-color laser printing of individual gold nanorods," *Nano Letters*, vol. 13, 09 2013.

[60] J. Do, K. N. Sediq, K. Deasy, D. M. Coles, J. Rodríguez-Fernández, J. Feldmann, and D. G. Lidzey, "Photonic crystal nanocavities containing plasmonic nanoparticles assembled using a laser-printing technique," *Advanced Optical Materials*, vol. 1, 12 2013.

[61] M. Li, T. Lohmüller, and J. Feldmann, "Optical injection of gold nanoparticles into living cells," *Nano Letters*, vol. 15, 01 2015.

[62] A. S. Urban, S. Carretero-Palacios, A. A. Lutich, T. Lohmüller, J. Feldmann, and F. Jäckel, "Optical trapping and manipulation of plasmonic nanoparticles: fundamentals, applications, and perspectives," *Nanoscale*, vol. 6, 2014.

[63] a. S. Urban, M. Fedoruk, S. Nedev, a. Lutich, T. Lohmueller, and J. Feldmann, "Shrink-to-fit Plasmonic Nanostructures," *Advanced Optical Materials*, vol. 1, no. 2, pp. 123–127, 2013.

[64] Y. Bao, Z. Yan, and N. F. Scherer, "Optical printing of electrodynamically coupled metallic nanoparticle arrays," *The Journal of Physical Chemistry C*, vol. 118, 08 2014.

[65] Z. Yan, R. A. Shah, G. Chado, S. K. Gray, M. Pelton, and N. F. Scherer, "Guiding spatial arrangements of silver nanoparticles by optical binding interactions in shaped light fields," *ACS Nano*, vol. 7, 02 2013.

[66] K. Dholakia and P. Zemánek, "Colloquium:gripped by light: Optical binding," *Review of Modern Physics*, vol. 82, 6 2010.

[67] V. Jacobsen, P. Stoller, C. Brunner, V. Vogel, and V. Sandoghdar, "Interferometric optical detection and tracking of very small gold nanoparticles at a water-glass interface," *Optics Express*, vol. 14, 2006.

[68] J. J. Richardson, M. Bjornmalm, and F. Caruso, "Technology-driven layer-by-layer assembly of nanofilms," *Science*, vol. 348, 04 2015.

[69] G. Decher and J. B. Schlenoff, *Multilayer Thin Films: Sequential Assembly of Nanocomposite Materials*. 2012.

[70] K. Setoura, Y. Okada, and S. Hashimoto, "Cw-laser-induced morphological changes of a single gold nanoparticle on glass: observation of surface evaporation," *Physical Chemistry Chemical Physics*, vol. 16, 10 2014.

[71] J. Happel and H. Rrenneh, "An introduction to fluid dynamics, g. k.batchelor, cambridge, university press, massachusetts (1967). 615 pages," *AIChE Journal*, vol. 14, 1968.

[72] T. Hida, *Brownian Motion*, pp. 44–113. New York, NY: Springer US, 1980.

[73] M. M. Burns, J.-M. Fournier, and J. A. Golovchenko, "Optical binding," *Phys. Rev. Lett.*, vol. 63, pp. 1233–1236, Sep 1989.

[74] K. Dholakia and P. Zemánek, "Colloquium: Gripped by light: Optical binding," *Reviews of Modern Physics*, vol. 82, no. 2, pp. 1767–1791, 2010.

[75] Z. Yan, S. K. Gray, and N. F. Scherer, "Potential energy surfaces and reaction pathways for light-mediated self-organization of metal nanoparticle clusters," *Nature Communications*, vol. 5, 5 2014.

[76] L. Chvátal, O. Brzobohatý, and P. Zemánek, "Binding of a pair of au nanoparticles in a wide gaussian standing wave," *Optical Review*, vol. 22, no. 1, pp. 157–161, 2015.

[77] G. Baffou, P. Berto, E. Bermúdez Ureña, R. Quidant, S. Monneret, J. Polleux, and H. Rigneault, "Photoinduced heating of nanoparticle arrays," *ACS Nano*, vol. 7, 08 2013.

[78] S. Baral, A. J. Green, M. Y. Livshits, A. O. Govorov, and H. H. Richardson, "Comparison of vapor formation of water at the solid/water interface to colloidal solutions using optically excited gold nanostructures," *ACS Nano*, vol. 8, 02 2014.

[79] M. T. Carlson, A. J. Green, and H. H. Richardson, "Superheating water by cw excitation of gold nanodots," *Nano Letters*, vol. 12, 2012.

[80] P. M. Bendix, S. N. S. Reihani, and L. B. Oddershede, "Direct measurements of heating by electromagnetically trapped gold nanoparticles on supported lipid bilayers," *ACS Nano*, vol. 4, 04 2010.

[81] Z. Fang, Y.-R. Zhen, O. Neumann, A. Polman, F. J. García de Abajo, P. Nordlander, and N. J. Halas, "Evolution of light-induced vapor generation at a liquid-immersed metallic nanoparticle," *Nano Letters*, 03 2013.

[82] Y. Dolinsky and T. Elperin, "Thermophoretic interaction of heat releasing particles," *Journal of Applied Physics*, vol. 93, 2003.

[83] B. J. Roxworthy, A. M. Bhuiya, S. P. Vanka, and K. C. Toussaint, "Understanding and controlling plasmon-induced convection," *Nature Communications*, vol. 5, pp. 1–8, 2014.

[84] B. V. Derjaguin, N. V. Churaev, and V. M. Muller, *Surface Forces*, vol. 10.1007/978-1-4757-6639-4. 1987.

[85] A. Würger, "Thermal non-equilibrium transport in colloids," *Reports on Progress in Physics*, vol. 73, 2010.

[86] R. Piazza and A. Parola, "Thermophoresis in colloidal suspensions," *Journal of Physics: Condensed Matter*, vol. 20, no. 15, p. 153102, 2008.

[87] V. P. S. Epstein, "Zur theorie des radiometeres," *Z. Physik*, vol. 54, pp. 537–563, 1929.

[88] A. P. Bregulla, A. Würger, K. Günther, M. Mertig, and F. Cichos, "Thermo-Osmotic Flow in Thin Films," *Physical Review Letters*, vol. 116, no. 18, 2016.

[89] M. Yang and M. Ripoll, "Thermoosmotic microfluidics," *Soft Matter*, 2016.

[90] J. L. Anderson, "Colloid transport by interfacial forces," *Annual Review of Fluid Mechanics*, vol. 21, 01 1989.

[91] R. T. Schermer, C. C. Olson, J. P. Coleman, and F. Bucholtz, "Laser-induced thermophoresis of individual particles in a viscous liquid.," *Optics express*, vol. 19, no. 11, pp. 10571–10586, 2011.

[92] A. Martin and M. M. Bou-Ali, "Determination of thermal diffusion coefficient of nanofluid: Fullerene–toluene," *Comptes Rendus Mécanique*, vol. 339, 2011.

[93] L. Lin, X. Peng, M. Wang, L. Scarabelli, Z. Mao, L. M. Liz-Marzán, M. F. Becker, and Y. Zheng, "Light-directed reversible assembly of plasmonic nanoparticles using plasmon-enhanced thermophoresis," *ACS Nano*, 09 2016.

[94] J. Irigoyen, S. E. Moya, J. J. Iturri, I. Llarena, O. Azzaroni, and E. Donath, "Specific ζ-potential response of layer-by-layer coated colloidal particles triggered by polyelectrolyte ion interactions," *Langmuir*, vol. 25, 03 2009.

[95] K. Wang, E. Schonbrun, P. Steinvurzel, and K. B. Crozier, "Trapping and rotating nanoparticles using a plasmonic nano-tweezer with an integrated heat sink," *Nature Communications*, vol. 2, 9 2011.

[96] Y.-J. Yang and Y.-G. Lee, "Comparison of plasmonic structures in terms of temperature increase under equivalent maximal trapping forces," *Journal of Applied Physics*, vol. 119, no. 8, p. 083108, 2016.

[97] B. J. Roxworthy, K. D. Ko, A. Kumar, K. H. Fung, E. K. C. Chow, G. L. Liu, N. X. Fang, and K. C. Toussaint, "Application of plasmonic bowtie nanoantenna arrays for optical trapping, stacking, and sorting," *Nano Letters*, vol. 12, 02 2012.

[98] B. J. Roxworthy, K. D. Ko, A. Kumar, K. H. Fung, E. K. C. Chow, G. L. Liu, N. X. Fang, and K. C. Toussaint, "Application of plasmonic bowtie nanoantenna arrays for optical trapping, stacking, and sorting," *Nano Letters*, vol. 12, no. 2, pp. 796–801, 2012.

[99] J. Kim, "Joining plasmonics with microfluidics: from convenience to inevitability," *Lab on a Chip*, vol. 12, 2012.

[100] M. Ploschner, "Optical forces near a nanoantenna," *Journal of Nanophotonics*, vol. 4, 02 2010.

[101] M. Braun and F. Cichos, "Optically controlled thermophoretic trapping of single nano-objects," *ACS Nano*, vol. 7, 12 2013.

[102] M. Braun, A. P. Bregulla, K. Gunther, M. Mertig, and F. Cichos, "Single molecules trapped by dynamic inhomogeneous temperature fields," *Nano letters*, vol. 15, no. 8, pp. 5499–5505, 2015.

[103] M. Braun, A. Würger, and F. Cichos, "Trapping of single nano-objects in dynamic temperature fields," *Physical Chemistry Chemical Physics*, vol. 16, no. 29, pp. 15207–15213, 2014.

[104] H.-R. Jiang, N. Yoshinaga, and M. Sano, "Active Motion of a Janus Particle by Self-Thermophoresis in a Defocused Laser Beam," *Physical Review Letters*, vol. 105, no. 26, p. 268302, 2010.

[105] S. Nedev, S. Carretero-Palacios, P. Kühler, T. Lohmüller, A. S. Urban, L. J. E. Anderson, and J. Feldmann, "An Optically Controlled Microscale Elevator Using Plasmonic Janus Particles.," *ACS photonics*, vol. 2, no. 4, pp. 491–496, 2015.

[106] S. Simoncelli, J. Summer, S. Nedev, P. Kühler, and J. Feldmann, "Combined Optical and Chemical Control of a Microsized Photofueled Janus Particle," *Small*, vol. 12, no. 21, pp. 2854–2858, 2016.

[107] E. E. Michaelides, "Brownian movement and thermophoresis of nanoparticles in liquids," *International Journal of Heat and Mass Transfer*, vol. 81, pp. 179–187, 2015.

[108] J. C. Giddings, P. M. Shinudu, and S. N. Semenov, "Thermophoresis of metal particles in a liquid," *Journal of Colloid and Interface Science*, vol. 176, no. 2, pp. 454–458, 1995.

[109] J. Giddings, P. M. Shinudu, and S. N. Semenov, "Thermophoresis of Metal Particles in a Liquid," *Journal of Colloid and Interface Science*, vol. 176, no. 2, pp. 454–458, 1995.

[110] S. Putnam, D. Cahill, and G. Wong, "Temperature dependence of thermodiffusion in aqueous suspensions of charged nanoparticles," *Langmuir*, vol. 23, pp. 9221–9228, 8 2007.

[111] L. Helden, R. Eichhorn, and C. Bechinger, "Direct measurement of thermophoretic forces," *Soft Matter*, vol. 11, 2015.

[112] J. Enger, K. Ramser, M. Goksör, D. Hanstorp, J. Prikulis, F. Svedberg, and M. Käll, "Optical spectroscopy of single trapped metal nanoparticles in solution," *Nano Letters*, vol. 4, 2004.

[113] F. Svedberg, Z. Li, H. Xu, and M. Käll, "Creating hot nanoparticle pairs for surface-enhanced raman spectroscopy through optical manipulation," *Nano Letters*, vol. 6, 2006.

[114] L. Tong, V. D. Miljković, P. Johansson, and M. Käll, "Plasmon hybridization reveals the interaction between individual colloidal gold nanoparticles confined in an optical potential well," *Nano Letters*, vol. 11, no. 11, pp. 4505–4508, 2011.

[115] A. Ohlinger, S. Nedev, A. A. Lutich, and J. Feldmann, "Optothermal escape of plasmonically coupled silver nanoparticles from a three-dimensional optical trap," *Nano Letters*, vol. 11, 04 2011.

[116] A. Würger, "Hydrodynamic boundary effects on thermophoresis of confined colloids," *Physical Review Letters*, vol. 116, 3 2016.

[117] K. Setoura, S. Ito, and H. Miyasaka, "Stationary bubble formation and marangoni convection induced by cw laser heating of a single gold nanoparticle," *Nanoscale*, 2016.

[118] A. A. Balandin, S. Ghosh, W. Bao, I. Calizo, D. Teweldebrhan, F. Miao, and C. N. Lau, "Superior thermal conductivity of single-layer graphene," *Nano Letters*, vol. 8, no. 3, pp. 902–907, 2008.

[119] R. R. Nair, P. Blake, a. N. Grigorenko, K. S. Novoselov, T. J. Booth, T. Stauber, N. M. R. Peres, and a. K. Geim, "Fine Structure Constant Defines Visual Transperency of Graphene," *Science*, vol. 320, 2008.

[120] S. Eigler, C. Dotzer, and A. Hirsch, "Visualization of defect densities in reduced graphene oxide," *Carbon*, vol. 50, no. 10, pp. 3666–3673, 2012.

[121] Y. Zhu, S. Murali, W. Cai, X. Li, J. W. Suk, J. R. Potts, and R. S. Ruoff, "Graphene and graphene oxide: synthesis, properties, and applications," *Advanced materials*, vol. 22, no. 35, pp. 3906–3924, 2010.

[122] G. Baffou and R. Quidant, "Nanoplasmonics for chemistry," *Chemical Society Reviews*, vol. 43, no. 11, pp. 3898–3907, 2014.

[123] M. R. Langille, M. L. Personick, and C. A. Mirkin, "Plasmon-mediated syntheses of metallic nanostructures," *Angewandte Chemie International Edition*, vol. 52, no. 52, pp. 13910–13940, 2013.

[124] S. Linic, U. Aslam, C. Boerigter, and M. Morabito, "Photochemical transformations on plasmonic metal nanoparticles," *Nature materials*, vol. 14, no. 6, pp. 567–576, 2015.

[125] S. Linic, P. Christopher, H. Xin, and A. Marimuthu, "Catalytic and photocatalytic transformations on metal nanoparticles with targeted geometric and plasmonic properties," *Accounts of chemical research*, vol. 46, no. 8, pp. 1890–1899, 2013.

[126] L. Brus, "Noble metal nanocrystals: plasmon electron transfer photochemistry and single-molecule raman spectroscopy," *Accounts of chemical research*, vol. 41, no. 12, pp. 1742–1749, 2008.

[127] Y. Zhai, J. S. DuChene, Y.-C. Wang, J. Qiu, A. C. Johnston-Peck, B. You, W. Guo, B. DiCiaccio, K. Qian, E. W. Zhao, *et al.*, "Polyvinylpyrrolidone-induced anisotropic growth of gold nanoprisms in plasmon-driven synthesis," *Nature Materials*, vol. 15, no. 8, pp. 889–895, 2016.

[128] L. Brus, "Plasmon-driven chemical synthesis: Growing gold nanoprisms with light," *Nature Materials*, vol. 15, no. 8, pp. 824–825, 2016.

[129] T. Klar, M. Perner, S. Grosse, G. Von Plessen, W. Spirkl, and J. Feldmann, "Surface-plasmon resonances in single metallic nanoparticles," *Physical Review Letters*, vol. 80, no. 19, p. 4249, 1998.

[130] P. L. Redmond, X. Wu, and L. Brus, "Photovoltage and photocatalyzed growth in citrate-stabilized colloidal silver nanocrystals," *The Journal of Physical Chemistry C*, vol. 111, no. 25, pp. 8942–8947, 2007.

[131] Y. Nishijima, K. Ueno, Y. Kotake, K. Murakoshi, H. Inoue, and H. Misawa, "Near-infrared plasmon-assisted water oxidation," *The journal of physical chemistry letters*, vol. 3, no. 10, pp. 1248–1252, 2012.

[132] N. H. Kim, C. D. Meinhart, and M. Moskovits, "Plasmon-mediated reduction of aqueous platinum ions: The competing roles of field enhancement and hot charge carriers," *The Journal of Physical Chemistry C*, vol. 120, no. 12, pp. 6750–6755, 2016.

[133] E. J. Bjerneld, K. Murty, J. Prikulis, and M. Käll, "Laser-induced growth of ag nanoparticles from aqueous solutions," *ChemPhysChem*, vol. 3, no. 1, pp. 116–119, 2002.

[134] E. J. Bjerneld, F. Svedberg, and M. Käll, "Laser-induced growth and deposition of noble-metal nanoparticles for surface-enhanced raman scattering," *Nano Letters*, vol. 3, no. 5, pp. 593–596, 2003.

[135] D. Alloyeau, W. Dachraoui, Y. Javed, H. Belkahla, G. Wang, H. Lecoq, S. Ammar, O. Ersen, A. Wisnet, F. Gazeau, *et al.*, "Unravelling kinetic and thermodynamic effects on the growth of gold nanoplates by liquid transmission electron microscopy," *Nano letters*, vol. 15, no. 4, pp. 2574–2581, 2015.

[136] U. Kreibig and M. Vollmer, *Optical properties of metal clusters*, vol. 25. Springer Science & Business Media, 2013.